Quantification of the Blood-Brain Barrier Permeability to Neutral and Charged Solutes

by

Wei Yuan

A dissertation submitted to the Graduate Faculty in Biomedical Engineering in partial fulfillment of the requirements for the degree of Doctor of Philosophy, The City University of New York

2009

This manuscript has been read and accepted for the Graduate Faculty in Biomedical Engineering in satisfaction of the dissertation requirement for the degree of Doctor of Philosophy.

Professor Bingmei M. Fu

Date

Chair of Examining Committee

Professor Mumtaz Kassir

Date

Executive Officer

Professor John M. Tarbell

Professor David S. Rumschitzki

Professor Marom Bikson

Professor Barclay Morrison

Supervision Committee

THE CITY UNIVERSITY OF NEW YORK

ABSTRACT

QUANTIFICATION OF THE BLOOD-BRAIN BARRIER PERMEABILITY TO NEUTRAL AND CHARGED SOLUTES

by

Wei Yuan

Advisor: Dr. Bingmei M. Fu

The blood-brain barrier (BBB) is a dynamic barrier essential for maintaining the micro-environment of the brain. Its special anatomical features determine its protective role for the central nervous system (CNS) as well as a barrier to drug delivery to the brain. The BBB is such a complicated barrier that even after numerous attempts have been made to decode its complexity, very little has been determined conclusively. One difficulty is a lack of quantitative and well-defined model system. In the first part of this study, a non-invasive method was developed to measure the rat cerebral microvessel permeability to solutes. This new *in vivo* quantitative method overcame disadvantages of previous open-skull methods that would cause increased BBB permeability in a very short time.

Although the existence of charge in the BBB has been found a long time ago, there are no detailed quantitative data and models that investigate the contribution of the charge carried by the endothelial surface glycocalyx and basement membrane to the permeability of the BBB. The second part of the study applied the newly developed non-invasive method to measure the permeability of the BBB to charged

molecules, and then to predict the charge density of the surface glycocalyx layer of the endothelium and that of the basement membrane in the BBB through mathematical modeling. Previous studies have shown that plasma glycoprotein orosomucoid modulates permeability of peripheral microvessels to charged molecules by contributing to the net charge on the microvessel wall. We also found that orosomucoid modulates the permeability of the BBB by altering its charge.

The cultured monolayer of b.End3, an immortalized mouse cerebral endothelial cell line, is becoming a more and more popular *in vitro* model of the BBB because of its advantages over the primary cultures in several aspects, e.g., easy growth and the ability to maintain the same characteristics over many passages. In the third part of this study, we examined whether or not b.End3 monolayer is a good *in vitro* model in studying transport across the BBB. We found that the b.End3 monolayer carries many characteristics of the BBB in terms of low solute permeability, comparable surface charge to that of the intact BBB endothelium, as well as similar transcellular transport of large nanoparticles as observed in the intact BBB.

ACKNOWLEDGEMENTS

I owe my deepest gratitude to my supervisor, Professor Bingmei M. Fu, for her endless support, encouragement and advice, for providing me with an environment which allowed me to do research independently, for her leading me into the challenging field of research, and for always stimulating my confidence and guiding me with patience and helping to build the foundation of my future career. Her positive attitude with which she approaches any challenge has always been inspirational. It has not always been an easy road, but she has been an anchor of support throughout my research.

I would also like to give my thanks to the members of my thesis committee: Professor John Tarbell (CCNY), Professor David Rumschitzki (CCNY), Professor Marom Bikson (CCNY), and Professor Barclay Morrison (Columbia University). They have been a source of encouragement and advice that have contributed a great deal in the course of my Ph.D. work.

I would like to give my special thanks to my colleagues, Dr. Min Zeng, Dr. Yonggang Lv, Qin Liu, Guanglei Li, Jie Fan, and Bin Cai. They gave me tremendous help and support, and this project could not exist without any of them. I would also like to thank Dr. Yuzhuo Su, Xiang Zhou, and Zhongdong Shi of the Department of Biomedical Engineering of the CCNY. Thanks for them being a great source of support and friendship.

Lastly, I would like to thank my family for their unconditional love and support throughout the years.

LIST OF FIGURES

LIST OF TABLES

CONTENTS

CHAPTER 1 INTRODUCTION

The Blood-Brain Barrier

The blood-brain barrier (BBB) is a unique dynamic regulatory interface between the cerebral circulation and the brain tissue, and it is essential for maintaining the micro-environment within brain. No other body organ so absolutely depends on a constant internal micro-environment as does the brain. In brain, the extracellular concentrations of amino acids and ions such as Na^+, K^+, and Ca^{2+} must be retained in very narrow ranges (Pardridge, 1998). If the brain is exposed to big chemical variations for these molecules, neurons would not function properly because some amino acids serve as neurotransmitters and certain ions modify the threshold for neuronal firing. The BBB also protects the central nervous system (CNS) from blood-borne neuroactive solutes, such as glutamate, glycine, norepinephrine, epinephrine, and peptide hormones (Smith, 2000), which can increase with physiological changes (such as diet and stress) and pathological changes (such as injury and diseases). In addition, the BBB plays a key role in facilitating the brain uptake of essential nutrients like glucose, hormones and vitamins, and larger molecules like insulin, leptin and iron transferring to sustain brain growth and metabolism (Zhang and Pardridge, 2001).

The term “blood-brain barrier” was coined by Lewandowsky in 1900 while he demonstrated that neurotoxic agents affected brain function only when directly injected into the brain but not when injected into the systemic circulation

(Lewandowsky, 1900). Nevertheless, the first experimental observation of this vascular barrier between the cerebral circulation and the CNS dates back to the 1880s, when Paul Ehrlich discovered that certain water-soluble dyes after injected into the systemic circulation were rapidly taken by all organs except the brain and spinal cord (Ehrlich, 1885), although Ehrlich himself interpreted these observations as a lack of the affinity of the nervous system for the dyes. Subsequent experiments performed by Edwin Goldmann, an associate of Ehrlich, demonstrated that the same dyes, when injected directly into the CNS, stained all types of cells in the brain tissue but not any other tissues in the rest of the body (Goldmann, 1913). It took additional 70 years until this barrier was firstly localized to cerebral microvascular endothelial cells by electron-microscopic studies done by Reese and Karnovsky (1967) and Brightman and Reese (1969). Although the concept of the BBB has continued to be refined over the past few decades, the recent understanding of the basic structure of the BBB is built on the general framework established by their studies in the late 1960s; more specifically, the BBB exists primarily as a selective diffusion barrier at the level of cerebral capillary endothelium.

The anatomical structure of the blood-brain barrier is shown in **Figure 1.1**. The circumference of the capillary lumen is completely surrounded by a single endothelial cell (E), the opposing membranes of which are connected by tight junctions (TJs). At the luminal surface of the endothelial cell, there is a fluffy glycocalyx layer (G) (Ueno *et al.*, 2004b), which is mainly composed of heparan sulfate proteoglycan, chondroitin sulfate proteoglycan, and hyaluronic (Henry and

Duling, 1999). This mucopolysaccharide structure is highly hydrated in electrolytic solution and contains large numbers of solid-bound fixed negative charges due to the polyanionic nature of its constituents with abundance in glycoproteins, acidic oligosaccharides, terminal sialic acids, proteoglycan, and glycosaminoglycans aggregates (Tarbell and Pahakis, 2006). Pericytes (Ps) attach to the abluminal membrane of the endothelium at irregular intervals. Pericytes and endothelial cells are ensheathed by the basal lamina (B), a membrane 30 to 40-nm thick composed of collagen type IV, heparin sulfate proteoglycans, laminin, fibronectin, and other extracellular matrix proteins (Farkas and Luiten, 2001). The basal lamina is contiguous with the plasma membranes of astrocyte (A) end-feet that ensheathe almost the entire abluminal surface of the endothelium (Pardridge, 1998).

Cerebral endothelial layer is different from that in the rest of body in several aspects. First, anatomically, cerebral endothelial layer is ensheathed by pericytes and astrocyte foot processes that cover almost the entire abluminal area of the capillary endothelium (Pardridge, 1998). Second, the mitochondrial content of the BBB capillary endothelial cells is greater than that of such cells in all non-neural tissues; it is suggested that this larger metabolic work capacity may be used to maintain the unique structural characteristics of BBB endothelial layer, or/and by metabolic pumps that may require energy to maintain the differences in composition of the cerebral circulation and the brain tissue (Oldendorf *et al.*, 1977). Third, BBB endothelial layer is characterized with high electrical resistance, much less fenestration, and more intensive tight junctions, which are responsible for restricting paracellular passage of

water and polar solutes from the peripheral circulation entering into the CNS (Butt *et al.*, 1990; Hawkins and Davis, 2005).

A number of grafting and cell culture studies have suggested that the ability of cerebral endothelial cells to form the BBB is not intrinsic to these cells, but the cellular milieu of brain somehow induces the barrier property into the blood vessels. It is believed that all components of the BBB are essential for maintaining functionality and stability of the BBB. Pericytes seem to play a key role in angiogenesis, structural integrity, and maturation of cerebral microvessels (Ballabh *et al.*, 2004). The extracellular matrix of the basal lamina appear to serve as an anchor for the endothelial layer via interaction of laminin and other matrix proteins with endothelial integrin receptors (Hynes, 1992). It was suggested that astrocytes are critical in the development and/or maintenance of unique features of the BBB. Additionally, astrocytes may act as messengers to or in conjunction with neurons in the moment-to-moment regulation of cerebral microvascular permeability (Ballabh *et al.*, 2004).

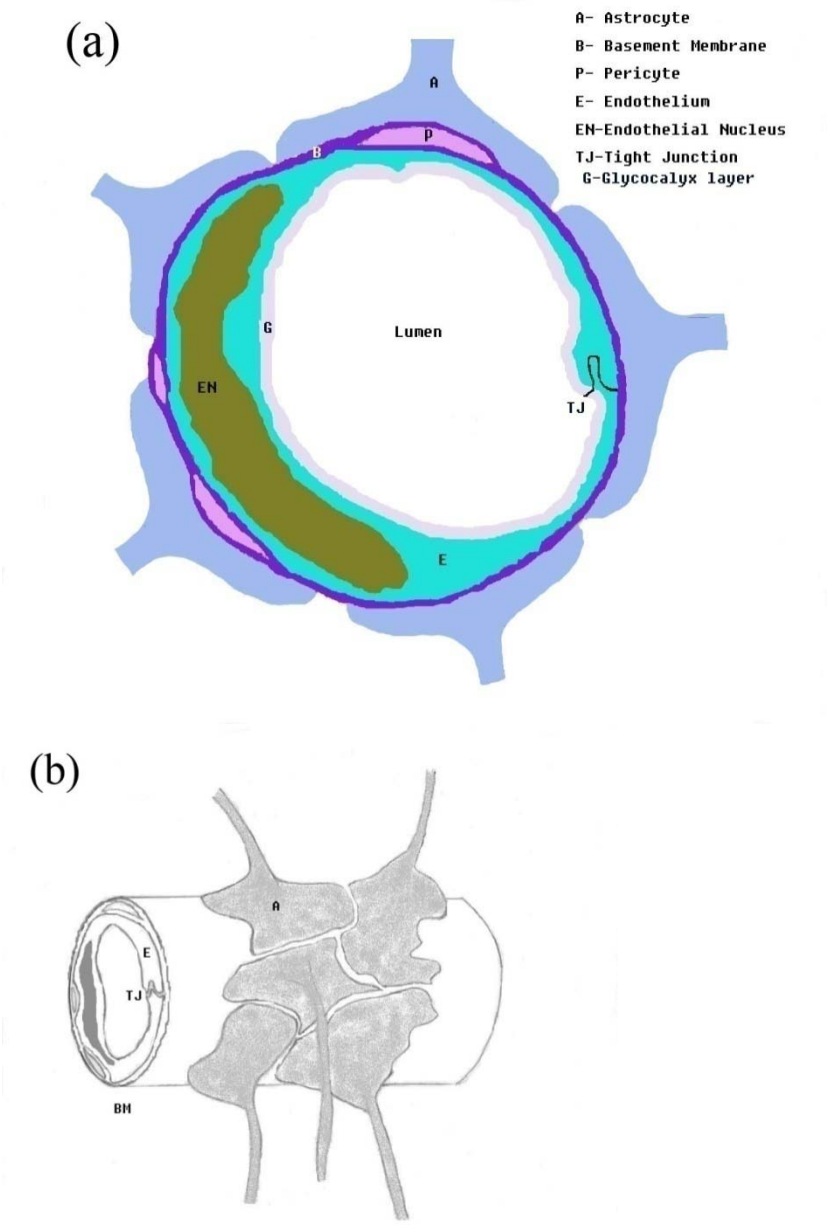

Figure 1.1 Schematic representation of the anatomical structure of the BBB. (a) Cross- sectional view. (b) 3-D view (Li *et al.*, 2007).

Transport across the BBB

The BBB endothelial cells differ from that in the rest of body by more intensive tight junctions, sparse pinocytic vesicular transport, and much less fenestrations. Endothelial cell tight junctions restrict hydrophilic molecules diffusion through the gaps between the cells (i.e., the paracellular pathway). In contrast, small hydrophobic molecules such as O_2 and CO_2 diffuse freely across plasma membranes following their concentration gradients (i.e., the transcellular pathway). The BBB permeability of most molecules can be estimated on the basis of their octanol/water partition coefficients (Sawchuk and Elmquist, 2000). For example, diphenhydramine (Benadryl), which has a high coefficient, can easily cross the BBB, whereas water-soluble loratadine (Claritin) is not able to penetrate the BBB and has little effect on the CNS (Kay, 2000).

However, the octanol/water partition coefficients do not completely reflect BBB permeability to solutes. Some solutes with low partition coefficients that easily enter into the CNS generally cross the BBB by active or facilitated transport mechanisms (**Figure 1.2**), which rely on ion channels, specific transporters, energy-dependent pumps, and a limited amount of receptor-mediated endocytosis. Glucose, amino acids, and small intermediate metabolites, for example, are ushered into brain tissue via facilitated transport mediated by specific proteins, whereas larger molecules, such as insulin, transferrin, and other plasma proteins, are carried across the BBB via receptor-mediated or adsorptive endocytosis (Pardridge, 1998).

Some small molecules with high octanol/water partition coefficients are observed to poorly penetrate the BBB. Recent studies suggested that these molecules

are actively pumped back into blood by efflux systems (Pardridge, 1998). These efflux systems greatly limit drug delivery across the BBB. For instance, P-glycoprotein (P-gp), which is a member of the adenosine triphosphate-binding cassette family of exporters, has been demonstrated to be a potent energy-dependent transporter. P-gp contributes greatly to the efflux of xenobiotics from brain to blood and has increasingly been recognized as having a protective role and being responsible for impeding the delivery of therapeutic agents (Schuetz *et al.*, 1996). The organic anion transporters and glutathione-dependent multidrug resistance-associated proteins (MRP) also contribute to the efflux of organic anions from the CNS, and many drugs with the BBB permeabilities that are lower than predicted are the substrates for these efflux proteins (Pardridge, 1998).

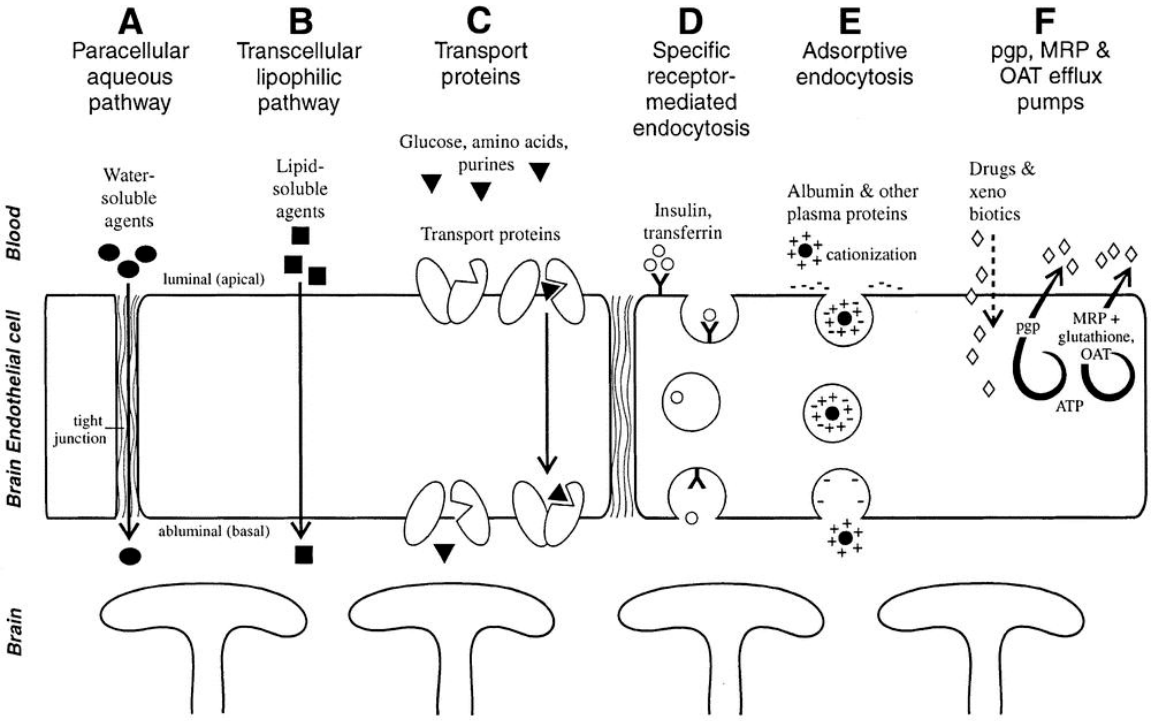

Figure 1.2 Transport pathways across the BBB. For normal homeostasis, carrier-mediated transport systems exist for hexoses (glucose, mannose, and galactose), monocarboxylic acids (acetic, lactic, and pyruvic acids), large neutral amino acids (tyrosine, phenylalanine, and isoleucine), acidic amino acids (glutamate and aspartate), basic amino acids (arginine and lysine), nucleic acid precursors (adenine, adenosine, and guanine), choline, and thyroid hormones (via transthyretin). The large neutral amino acid transporters, like the glucose transporter, are present on both the luminal and abluminal membranes of endothelial cells and are bidirectional, although they are most important for influx to the brain, whereas other transporters are unidirectional efflux systems. The carrier for small neutral amino acids is primarily located on the abluminal membrane and allows only efflux. Potassium efflux is archieved with an energy-dependent process that exchanges sodium for potassium at

the abluminal membrane, with adenosine triphosphate (ATP) as the energy source (Na+/K+-adenosine triphosphatase). P-gp, which is localized to the luminal membrane of endothelial, pumps amphipathic organic cations or neutral compounds out of the CNS into the blood, while multidrug resistance-associated protein (MRP) and organic anion transporter (OAT) pump anions out of the CNS as efflux proteins. (Neuwelt, 2004).

Significance of the Study

Breakdown of the BBB in Disease and Injury

CNS disorders, such as multiple sclerosis, HIV infection, and brain tumors, are often associated with the breakdown of the BBB. In some diseases, such as ischemic stroke, increased BBB permeability resulting from the disrupted BBB is a consequence of pathological conditions, whereas in other diseases, such as multiple sclerosis, BBB opening may be a precipitating event. Additionally, after traumatic brain injury, the BBB is disrupted acutely and transiently, which is always accompanied with vasogenic edema and ischemia. Vasogenic edema leads to brain swelling and highly increased intracranial pressure, and ischemia robs the brain of blood flow resulting from a lack of perfusion pressure. Vasogenic edema due to the breakdown of the BBB is a life threatening complication of stroke (Rosenberg, 1999) and often accompanies the progression of multiple sclerosis (Floris *et al.*, 2004) and encephalitis (Dallasta *et al.*, 1999), and it could also be involved in the autoimmune destruction of myelin and neurons (Petty and Lo, 2002). Furthermore, as a

consequence of certain CNS diseases, such as Alzheimer's disease progression and chronic inflammatory pain, the BBB becomes compromised, allowing influx of the molecules and cells that are normally excluded under homeostatic conditions (Calabria and Shusta, 2006). In addition, the infiltration of circulating immune cells can lead to brain inflammation and the subsequent destruction of neural cells.

Due to the unique features of the BBB structure, for better understanding the breakdown of the BBB, it is necessary to take into account not only the endothelial junction dysfunction but also damages to the basement membrane, pericytes, astrocytes, vascular innervation, and components of the immune system. In addition to the endothelial surface glycocalyx, the basement membrane behaves as another molecular sieve of the BBB. It was reported to retain a fraction of a variety of solutes such as HRP and sucrose (Brightman and Kaya, 2000). Both the endothelial surface glycocalyx and the basement membrane were found to be markedly damaged in rat brain in pathological states (Ueno *et al.*, 2004b). Although many biochemical factors induced by brain diseases have been found to affect the endothelial tight junction proteins, modulate the neurovascular matrix, interfere with cell-matrix signaling and homeostasis, how they ultimately disrupt the structural components of the BBB to increase the BBB permeability and how to restore the BBB structures by therapeutic agents are not well understood. Therefore, understanding these molecular and structural mechanisms by which the BBB permeability is modulated is crucial in combating CNS diseases.

Drug Delivery across the BBB

Designed for protecting brain from blood-born neurotoxins, the BBB extremely limits the therapeutic efficacy of drugs into the CNS. It blocks almost 100% large-molecule neurotherapeutics and more than 98% of all small-molecule drugs (Pardridge, 2006). This greatly hinders the treatment of major brain diseases, such as Alzheimer disease, Parkinson disease, and brain tumor. Although the molecular Trojan horses for the BBB drug delivery are very promising in delivering large peptides and recombinant proteins such as neurotrophins, enzymes, and monoclonal antibodies (Pardridge, 2006), the traffic is limited by the number and carrying capacity of the transporters, as well as by the number of drug molecules that can attach to each antibody. Therefore, development of delivery strategies through other pathways of the BBB is necessary. The assessment for the permeability of cerebral microvessels to various drugs across the BBB is very important for the drug development for CNS disorders, especially at the early stage for searching new drug candidates with the ability to penetrate the BBB. It is also an essential tool to search the methods to modulate the paracellular pathway of the BBB to improve the delivery efficacy, and to evaluate the therapy changing the permeability property of microvessels at the pathological region to enhance drug delivery.

Previous Studies

Several *in vivo* rat models have been used for the study of the solute transport across the BBB, including pharmacokinetic methods (Cornford *et al.*, 1992; van

Uitert *et al.*, 1981; Zlokovic *et al.*, 1986), intracerebral microdialysis (de Lange *et al.*, 1999), positron emission tomography (PET) (Elsinga *et al.*, 2004), magnetic resonance imaging (MRI) (Wang *et al.*, 2007), the intravital microscopy study (Gaber *et al.*, 2004), and occluding single microvessel measurement (Easton and Fraser, 1994).

Pharmacokinetic methods are used to evaluate the delivery of a molecule from the systemic circulation into the brain, in which the amount of solute delivered to the brain can be expressed by percentage of injected dose delivered per gram of the brain. Generally, a small volume of buffered Ringer's solution containing the compound of interest and a radio-labeled diffusible reference compound as an internal standard (such as 3H-water) is injected into the common carotid artery or the internal carotid artery or the venule depending on different techniques. Then, the animal is sacrificed 5–15s after injection, and the brain tissue and the injection solution are analyzed to calculate the brain uptake index (BUI) (Pardridge, 1998). The assumptions of these models are that the reference compound is freely diffusible across the BBB, that the drug does not back-diffuse from the brain to blood, and that no metabolism of the compounds occurs before decapitation. The advantage of these pharmacokinetic methods is fast and many compounds can be assessed in a short time, which is ideal in the high-throughput setting. The major disadvantages are: 1) brain extraction only occur over a limited time, making it difficult to measure the brain uptake index (Pardridge, 1998); 2) the driving force for the transport is unknown.

Intracerebral microdialysis involves direct sampling of brain interstitial fluid by a dialysis fiber directly implanted into the brain. The concentration of compound that has permeated into the brain following oral, intravenous or subcutaneous administration can be monitored over time within the same animal. Any drug that enters the brain interstitial fluid will permeate into the physiological solution within the probe, and the solution may be subsequently assayed by an appropriate technique. The major advantage of this technique is that it provides pharmacokinetic profiles of drugs in the brain without killing animals at different time points. One limitation of this technique is that it greatly relies on and limited by the sensitivity of the assay technique (de Lange *et al* 1999), since the solute concentrations may be extremely low in the dialysate. Another major disadvantage is that insertion of the probe can result in chronic BBB disruption.

More recently, various imaging techniques, including positron emission tomography (PET) and magnetic resonance imaging (MRI) have been used to determine BBB permeability in humans. PET is a non-invasive tracer technique used to quantify the BBB extravasation. Magnetic resonance imaging (MRI) is also non-invasive techniques, but it is more qualitative than quantitative. The major disadvantages for these techniques include their inherent costs, labor intensity, relatively low resolution (100μm to 1mm) and inability to differentiate between parent compound and metabolites (Nicolazzo *et al.*, 2006).

All of above-mentioned methods, except occluding single microvessel measurement, only determine certain indexes of relative permeability for the drug

uptake to brain since they cannot determine the driving force for the leakage flux. Gaber *et al*., 2004 suggested a method to measure clearance or leakage of drug out of the pial microvessels rather than 'true' permeability of the microvessels to hydrophilic solutes, since it did not consider that the change of the concentration of dye in the vessel, i.e. the driving force, also contributes to the amount of dye extravasation to the tissue. Because it is hard to measure the BBB permeability in brain parenchyma, the microvessels in pia dura at the surface of brain are often used in *in vivo* BBB permeability study. Although pial microvessels do not have the entire ensheathment of astrocytes as those cerebral microvessels in the parenchyma, the pial and cerebral microvessels appear to have many morphophysiolgical properties in common. These include ultrastructural characteristics, permeability of cell junctions to electron dense tracers, trans-endothelium electrical resistance, and molecular properties of endothelium. For these reasons, pial microvessels are often used in the BBB permeability studies (Allt and Lawrenson, 1997a).

The occluding single microvessel measurement is done directly on one single exposed pial microvessel after the frontal craniotomy removing a small section of skull and the dura mater (Easton *et al.*, 1997). This method has well-controlled conditions including known concentration difference across the microvessel wall. However, recent study suggests that the exposed rat pial microvessels become leaky to both small and large molecules within 20-60 minutes following the craniotomy and the permeability of the exposed microvessels rises sharply after 160 minutes (Easton *et al.*, 1997).

In addition, *in vitro* model holds several advantages over *in vivo* model, including high-throughput screening at low cost, the ability to easily assess compound and to investigate the transport mechanism at molecular level, besides its comparatively high permeability and the loss of expression of some of BBB efflux protein systems (Nicolazzo *et al.*, 2006). Recently, the *in vitro* model deriving from immortalized brain endothelial cell line, b.End3, become more and more popular as BBB transport study because of its ability to maintain characteristics over many passages and easy growth and low cost.

Objectives of This Study

To quantify the permeability of intact rat BBB and overcome the above-mentioned disadvantages, the first objective of the current study is to develop a non-invasive method to measure the solute permeability of the rat pial microvessels *in vivo*.

Although the existence of charge in the BBB has been found a long time ago, there are no detailed quantitative data and models that investigate the contribution of the charge carried by the endothelial surface glycocalyx and basement membrane to the permeability of the BBB. The second objective is to apply the newly developed non-invasive method to measure the solute permeability of the BBB to charged molecules and particles, and then to quantify the charge density of the surface glycocalyx layer of the endothelium as well as that in the basement membrane of the BBB.

Previous studies have shown that plasma glycoprotein orosomucoid modulates permeability of peripheral microvessels to charged molecules by contributing to the net charge on the microvessel wall. We also test the hypothesis that orosomucoid modulates the permeability of the blood-brain barrier (BBB) by altering the charge of the BBB.

The cultured monolayer of b.End3, an immortalized mouse cerebral endothelial cell line, is becoming a more and more popular *in vitro* model of the BBB because of its advantages over the primary cultures in several aspects, e.g., easy growth and the ability to maintain the characteristics of the BBB over many passages. Therefore, the third objective of this study is to examine whether or not b.End3 monolayer is a good *in vitro* model in studying transport across the BBB, especially the transport of the charged molecules.

CHAPTER 2 NON-INVASIVE MEASUREMENT OF SOLUTE PERMEABILITY IN CEREBRAL MICROVESSELS OF THE RAT

Introduction

The blood-brain barrier (BBB) is a dynamic interface between the cerebral circulation and brain tissue and is essential for maintaining the micro-environment within the brain. The BBB endothelial layer is different from that in the rest of body in several aspects. First, anatomically, BBB endothelial layer is ensheathed by pericytes and astrocyte foot processes which cover almost the entire abluminal area of the capillary endothelium (Nicolazzo *et al.*, 2006). Second, BBB endothelial layer is characterized with high electrical resistance and much less fenestration and more intensive tight junctions, which are responsible for restricting paracellular passage of water and polar solutes from the peripheral circulation entering into the central nervous system (CNS) (Butt *et al.*, 1990; Hawkins and Davis, 2005).

Along with its importance for protecting brain from blood-born neurotoxins, however, the BBB extremely limits the therapeutic efficacy of drugs into the CNS. It blocks almost 100% large-molecule neurotherapeutics and more than 98% of all small-molecule drugs (Pardridge, 2006). This greatly hinders the treatment of major brain diseases, such as Alzheimer disease, Parkinson disease and brain tumor. Thus, the assessment for the permeability of cerebral microvessels for various drugs across

the BBB is very important for the drug development for CNS disorders, especially at the early stage for searching new drug candidates with the ability to penetrate the BBB. It is also an essential tool to evaluate the therapy changing the permeability property of microvessels at pathological region to enhance drug delivery. In addition, the CNS disorders, such as multiple sclerosis, HIV infection and brain tumors, are always associated with microvessel hyperpermeability, which is the critical step for the abnormal transport of molecules and cells across the blood vessel wall; therefore, understanding the mechanisms of microvessel hyperpermeability from various approaches is important in combating these malignant diseases.

Several *in vivo* rat models have been used for transport across the BBB study, including brain efflux index (BEI) using vital injections (the single carotid injection, *in situ* perfusion injection and intravenous injection), intracerebral microdialysis (Nicolazzo *et al.*, 2006), positron emission tomography (PET), magnetic resonance imaging (MRI), the intravital microscopy study (Gaber *et al.*, 2004), and occluding single microvessel measurement (Easton and Fraser, 1994). However, all of these models, except occluding single microvessel measurement, only reflect certain indices of relative permeability for the drug uptake to brain. Gaber *et al*., 2004 suggested a method to measure clearance or leakage of drug out of the pial microvessels rather than 'true' permeability of the microvessels to hydrophilic solutes, since it did not consider that the change of the concentration of dye in the vessel, i.e. the driving force, also contribute the change of the amount of dye extravasation to the tissue. The occluding single microvessel measurement is done

directly on one single exposed pial microvessel after the frontal craniotomy removing a small section of skull and dura mater. Since it is hard to measure BBB permeability in brain parenchyma, the microvessels in pia mater at the surface of brain are often used in *in vivo* BBB permeability study, and pial microvessel has been proved as a valid BBB study model (Lawrenson *et al.*, 1997).

Recent study suggests that the exposed rat pial microvessels become leaky to both small and large molecules within 20-60 minutes following the craniotomy and the permeability of the exposed microvessels rises sharply after 160 minutes (Easton *et al.*, 1997). To quantify the permeability of intact rat pial microvessels, we developed a non-invasive method, without exposing the vessels, to measure the apparent permeability (P) of post-capillary venules on rat pia mater (20-40 μm in diameter) to various sized fluorescence tracers: sodium fluorescein (NaF, MW 376, Stokes' radius 0.45nm), fluorescein isothiocyanate – dextran 4000- conjugate (FITC-dextran-4k, MW 4,000, Stokes' radius 1.4nm), FITC-dextran-10k (MW 10k, Stokes' radius 1.9nm), FITC-dextran-20k (MW 20k, Stokes' radius 2.4nm), FITC-dextran-40k (MW 40k, Stokes' radius 3.0nm) and FITC-dextran-70k (MW 70k, Stokes' radius 3.6nm). The pial microvessels were observed by a high numerical aperture objective lens (Nikon, 20×, 0.75 N.A.) through a section of frontoparietal bones (~ 6mm × 6mm) thinned with a high-speed micro-grinder (revised surgery method from Easton *et al.*, 1997). P was measured on individual pial venular microvessel with the perfused fluorescence tracer solution by using quantitative fluorescence microscope

imaging method adapted from the fluorescence microscope photometry (Fu *et al.*, 1998).

Materials and methods

General preparation

All *in vivo* experiments were performed on adult female Sprague–Dawley rats (250–300 g) supplied by Hilltop Laboratory Animals (Scottdale, PA). All procedures and the animal use have been approved by the Institutional Animal Care and Use Committee at the City College of New York. The rat (age 3–4 months) was anesthetized with pentobarbital sodium given subcutaneously. The initial dosage was 65 mg/kg, and additional 3 mg/dose was given as needed. The rat was then kept warm on a heating pad. The skull in the region of interest was exposed by shaving off the hair and cutting away the skin and connective tissue. A section of left or right frontoparietal bone, approximately ~ 5 mm × ~ 5 mm, was carefully ground with a high-speed micro-grinder (0–50,000 rpm, DLT 50KBU; Brasseler USA, GA) until a part of it (~ 2 mm × ~ 2 mm) became soft and translucent. The blood vessels could be seen under a 16× dissection microscope (**Figure 2.1**). During the process, artificial cerebrospinal fluid (ACSF) with the room temperature was applied to the surface of the skull to remove the heat due to grinding. After grinding, the rat was laid face-up on a tray with its thinned section of the head placed in a shallow chamber formed by a glass cover slip. The thinned section was observed under the microscope and the pial microvessels were focused by carefully adjusting the focusing knob. The fluorescent

solution was introduced into the cerebral circulation via the left or right carotid artery by a syringe pump at a constant rate of 3 ml/min while the images of the pial microvessels and nearby brain tissue were simultaneously collected (**Figure 2.2**). To repeat the measurement, the perfusate was switched to a washout solution containing no fluorescently labeled solutes to wash away the fluorescence in the microvessel.

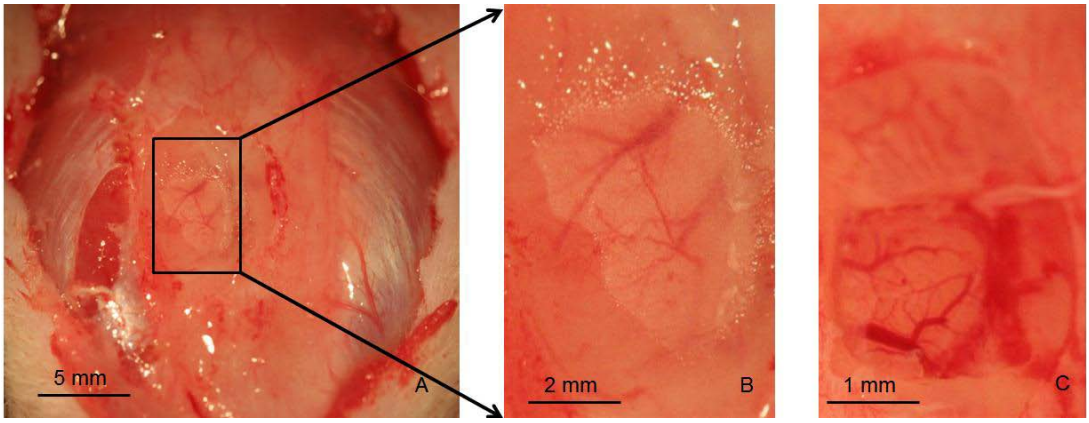

Figure 2.1 (A) The thinned frontoparietal bone on the rat skull; (B) Enlarged thinned section; (C) Exposed pial vessels by removing the thinned frontoparietal bone and the meninges (the method used Easton *et al.*, 1997).

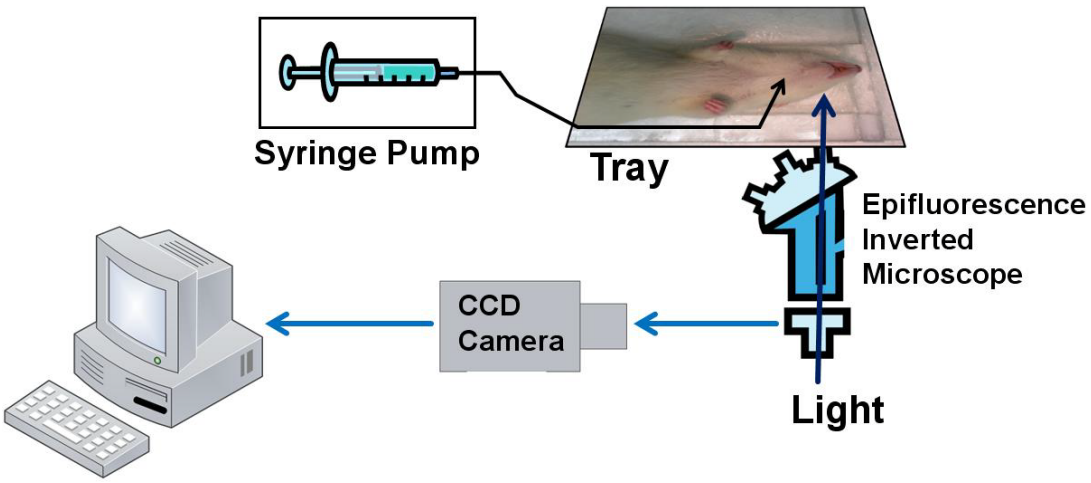

Figure 2.2 The experimental setup. The fluorescence solution was injected into the brain via a carotid artery with a syringe pump. The fluorescence images were captured by a CCD camera, which was connected to a Nikon inverted microscope. The image analysis software was then used to measure the fluorescence intensity for the region of interest in each image.

Microscope preparation

A detailed description of a photometry method used to measure permeability (*P*) of fluorescently labeled solutes has been published elsewhere (Adamson *et al.*, 1988; Fu *et al.*, 1998; Huxley *et al.*, 1987). In the current experiment, we used an imaging method instead of photometry. A Nikon TE2000-E inverted fluorescence microscope was used to observe pial microvessels. The rat was laid on a customized tray with the thinned section of the rat skull placed on a glass cover slip (view area ~ 20 mm diameter) which was embedded in the tray. The surface of the skull was constantly superfused with 37 °C ACSF at the rate of ~ 1 ml/min through a dripping

tube attached to the side of the head. The vessels were observed with a 20× lens (NA = 0.75, Nikon) and an illumination system (the monochromator with a xenon lamp, FSM150Xe; Bentham, U.K.), which was computer-controlled to change the excitation/emission wavelengths for various fluorescent probes. The intensity of the xenon light source was controlled by an attenuator knob on the front panel of the lamp house. The intensity of the light output can be adjusted from 0% to 100%. To reduce the tissue damage due to the exposure to fluorescence light, the light intensity was kept as low as possible. Further protection was provided by using an experimental protocol in which the time of tissue exposure to the excitation light was kept as short as possible for the permeability measurement. The excitation/emission wavelengths were set to 475 nm/520 nm and 490 nm/520 nm for sodium fluorescein and FITC-dextrans, respectively. The images were captured using a highly sensitive 12-bit CCD camera (Sensicam QE; Cooke, MI) and then transferred to an imaging acquisition and analysis workstation. The spatial resolution of our system with 20× lens (NA = 0.75) is 0.5 μm/pixel. The acquisition speed is 3 frames/s for image size of 1024 × 1376 pixels or 8 frames/s for image size 512 × 672 pixels.

Solutions and fluorescent test solute preparation

Mammalian Ringer solution

Rat Ringer solution was used for all perfusates. The solution composition was (in mM) NaCl 132, KCl 4.6, $MgSO_4$ 1.2, $CaCl_2$ 2.0, $NaHCO_3$ 5.0, glucose 5.5 and HEPES 20. All these chemicals were from Sigma. The pH was buffered to 7.4–7.45

by adjusting the ratio of HEPES acid to base. In addition, both the washout solution and the fluorescent dye solution contained bovine serum albumin (BSA, A4378, Sigma) at 10 mg/ml (Fu and Shen, 2004) The solutions were made fresh on the day of use to avoid binding to the serum albumin (Adamson *et al*., 1994 and Fu *et al*., 1998).

Sodium fluorescein

Sodium fluorescein (F6377, Sigma; mol. wt. 376, Stokes–Einstein radius ~ 0.45 nm) was dissolved at 0.1 mg/ml in the Ringer solution containing 10 mg/ml BSA.

FITC-dextrans

All FITC-dextrans, FITC-dextran-4k (FD4, Sigma; mol. wt. 4000, Stokes radius ~ 1.4 nm), FITC-dextran-10k (FD10 s, Sigma; mol. wt. 10,000, Stokes radius ~ 1.9 nm), FITC-dextran-20k (FD20 s, Sigma; mol. wt. 20,000, Stokes radius ~ 2.4 nm), FITC-dextran-40k (FD40 s, Sigma; mol. wt. 40,000, Stokes radius ~ 3.0 nm), and FITC-dextran-70k (FD70 s, Sigma; mol. wt. 70,000, Stokes radius ~ 3.6 nm), were used in experiments at the concentration of 1 mg/ml in Ringer solution containing 10 mg/ml BSA.

Artificial Cerebrospinal Fluid (ACSF)

The ACSF solution composition was (in mM) NaCl 110.5, KCl 4.7, $CaCl_2$ 2.5, KH_2PO_4 1.1, $MgSO_47H_2O$ 1.25, $NaHCO_3$ 25 and HEPE 15 (Easton *et al.*, 1997),

and the solution was buffered to pH 7.4 ± 0.5. All chemicals were obtained from Sigma.

Permeability measurement

The left or right carotid artery was cannulated with a PE50 tubing with I.D. 0.58 mm and O.D. 0.965 mm from Becton Dickinson, and the fluorescent solution was introduced into the cerebral circulation by a syringe pump at a constant rate of 3 ml/min. It took ~ 15 s for the dye from the cannulation site to the microvessel. Measurement of solute permeability *P* was made on individual post-capillary venule (20–40 μm in diameter). We followed the method described in Easton *et al*. (1997) for identifying post-capillary venules. When the dye was perfused into the pial microvessels, the images were recorded simultaneously. The *P* was determined off-line from the prerecorded images. Briefly, in recorded images, the total fluorescence intensity (*I*) in a rectangular window including the vessel lumen and surrounding tissue (**Figure 2.3**) was measured by using the imaging analysis software (Intracellular Imaging Inc., Cincinnati, OH). The measuring window was at least 100–200 μm long and 40–100 μm wide and was set at least 100 μm from the base of the bifurcation to avoid solute contamination from the side arms. The size and placement of the measuring window were chosen to satisfy that 1) the vessel segment is straight; 2) the dye does not spread out of the window during the time for *P* measurement (5–30 s for the size of dyes used in our experiment); and 3) no contamination of dye from the neighboring vessels. When these conditions were satisfied, *P* that is defined as the solute outflow rate per unit vessel surface area

divided by the concentration difference across the vessel wall, could be calculated from the relationship $P = (1/\Delta I_0)\,(dI/dt)_0(r/2)$, where ΔI_0 is the step increase in fluorescence intensity in the measuring window as the test solute fills the microvessel lumen, $(dI/dt)_0$ is the initial rate of increase in fluorescence intensity after the solute fills the lumen and begins to accumulate in the tissue, and r is the vessel radius (**Figure 2.4**) (Adamson *et al.*, 1988; Adamson *et al.*, 2004b; Fu *et al.*, 1998; Huxley *et al.*, 1987). We measured the diameter of the vessel and the total intensity of fluorescence in the lumen of the vessel segment from the recorded images and found no changes during the period in our experiments (up to 1 min). This indicates that there was no vasoreactivity, which may induce the change in the vessel radius.

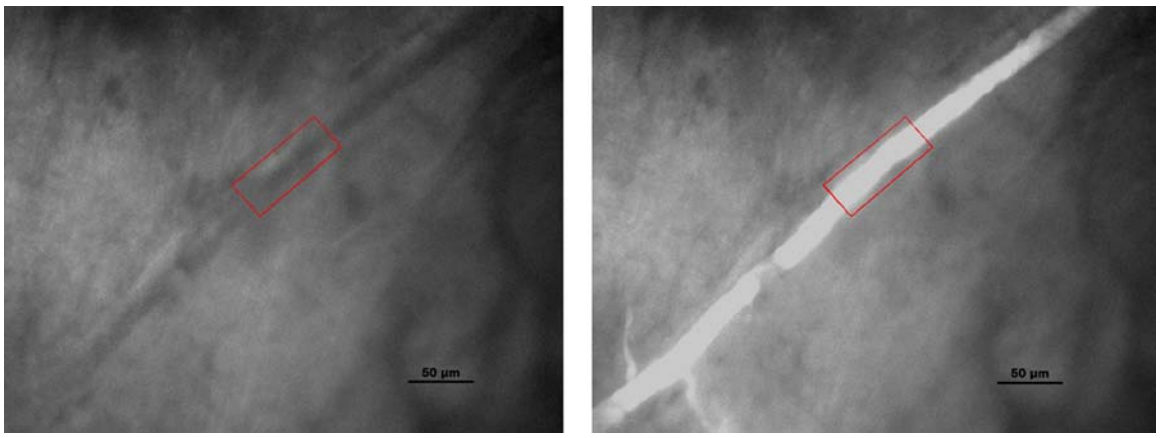

(A) **(B)**

Figure 2.3 A pial microvessel before (A) and after (B) filled with the fluorescent solution. The fluorescence intensity in the rectangular window (in red) was measured to determine the solute permeability P.

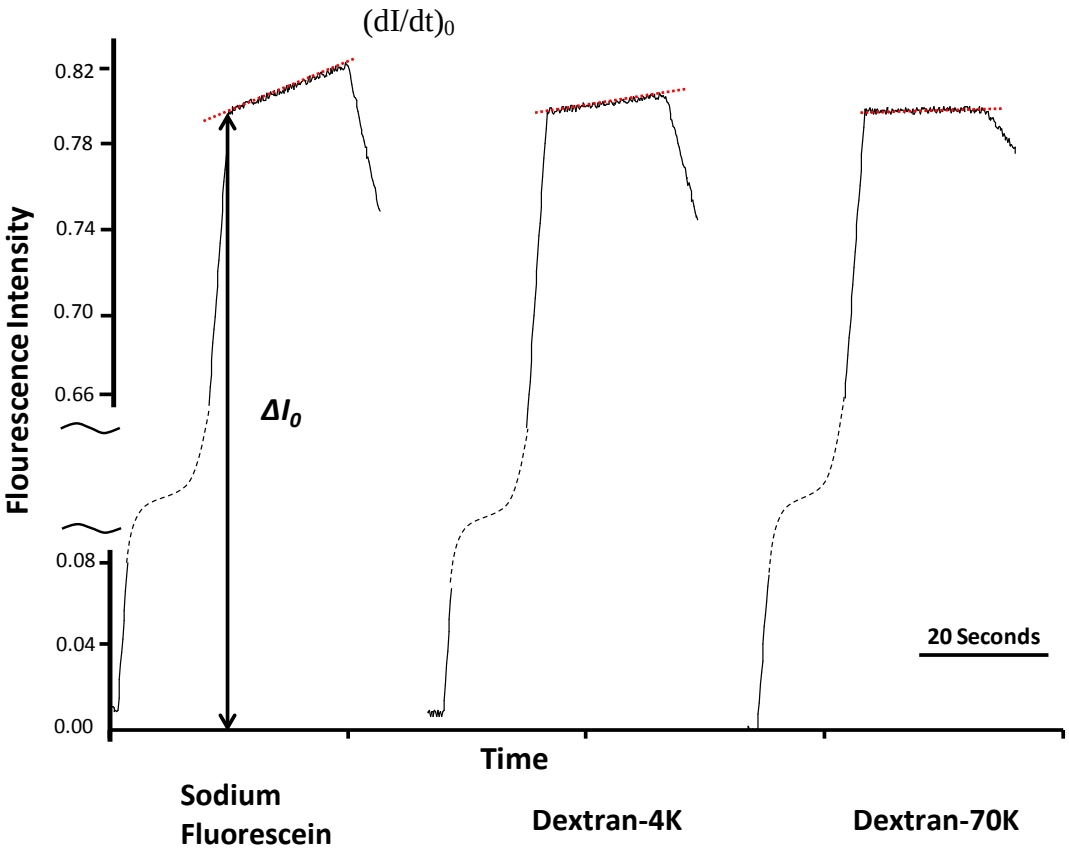

Figure 2.4 Typical curves of fluorescence intensity (normalized value) as a function of time for solute permeability measurements on three individual microvessels of ~ 30 μm diameter for three solutes. The left panel is for the permeability to sodium fluorescein, which is 2.62×10^{-6} cm/s. The middle panel is for FITC-dextran-4k permeability, which is 0.88×10^{-6} cm/s. The right panel is for the permeability to FITC-dextran-70k, which is 0.12×10^{-6} cm/s.

Calibration experiments

The primary assumption in the calculation of *P* with the use of fluorescent solutes is that the fluorescence intensity *I* is a linear function of the number of solute molecules (concentration) in the measuring field. To test the linear range of the intensity vs. the concentration, we used the same instrument settings in the *in vitro* calibration experiments as those used in *in vivo* permeability measurements. *In vitro* calibrations were performed using two chambers of different depths. One was a cell counting chamber (hemocytometer) of depth of 100 μm (Hausser Scientific, PA), and the other was the chamber constructed of glass cover slips (Adamson *et al.*, 1988; Fu *et al.*, 1998; Huxley *et al.*, 1987). The latter chamber has a depth of approximately 170 μm. A large 24 × 50-mm cover slip formed the base of the chamber. Two small 22-mm^2 cover slips were laid on top of this base, ~ 1 cm apart, and a third small cover slip was placed on top of those to form a chamber, 170 μm deep. Solutions of fluorescence probes were applied to fill the chamber by capillarity. The chamber was cleaned before the solution of different concentration was applied. The measuring window was ~ 250 μm × 300 μm. These *in vitro* calibration experiments showed that the relationship between the concentration and the fluorescence intensity was linear from 0.05 to 0.12 mg/ml for sodium fluorescein (**Figure 2.5**), from 0.2 to 2 mg/ml for FITC-dextrans with various molecular weights (not shown here) for both 100 μm and 170 μm chambers. We used 0.1 mg/ml sodium fluorescein or 1 mg/ml FITC-dextrans at 28% maximum power of illumination in our *in vivo* experiments.

Furthermore, we found in the *in vitro* photo bleaching experiment that for 0.1 mg/ml sodium fluorescein, or 1 mg/ml FITC-dextrans at 28% maximum power of illumination, the intensity *I* values fell less that 0.5% of their original values in ~ 1 min. One minute was typically 2 to 3 times of the exposure time required for an individual solute permeability measurement (**Figure 2.4**). The low degree of photo bleaching was due to the reduced excitation light intensity and more sensitive camera for the image collection.

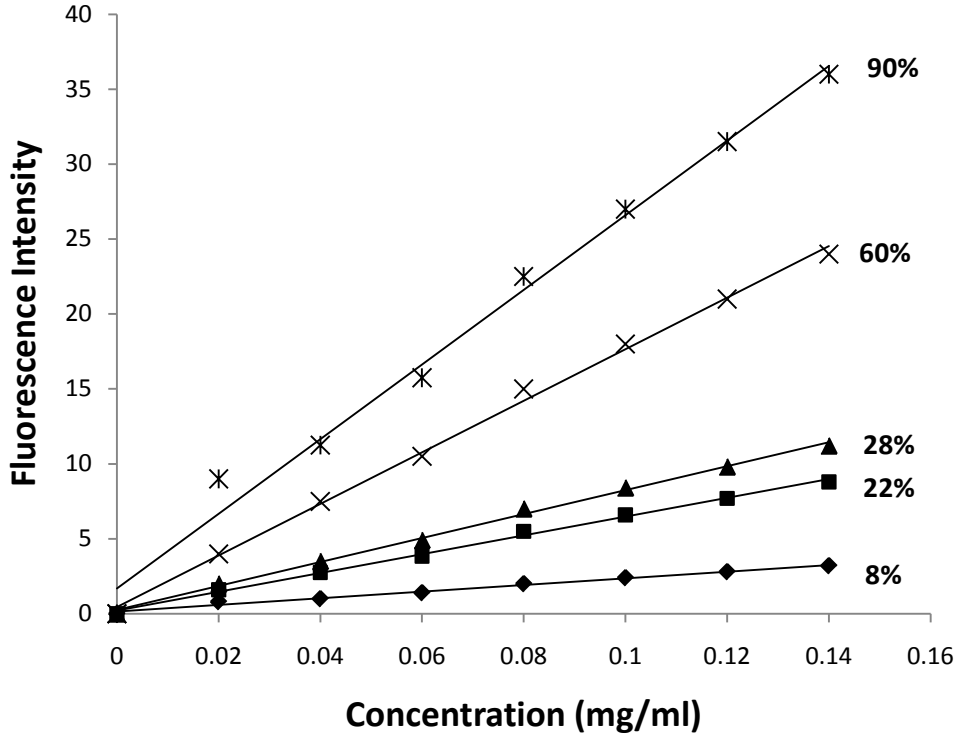

Figure 2.5 In vitro calibration experiments using a cell counting chamber (hemocytometer) with 100 μm depth. Fluorescence intensity (arbitrary unit) was measured for different concentrations of sodium fluorescein under various strengths of laser output. Percentage is relative to the maximum power of our light system.

Depth of light collection

Since the measurements of fluorescence intensity for pial microvessels were performed on thick tissue, collection of the light from out-of-focus region would contribute to the measured value of intensity. To measure the depth of light collection of our system, we did *in vitro* experiments similar to Huxley *et al*. (1987) and Yuan *et al*. (1993) but using an imaging system to determine the fluorescence intensity. Four chambers with different depths, 50 μm from Intracellular Imaging Inc. (Cincinnati, OH), 100 μm (hemocytometer), 170 μm chamber formed by cover slips (described in the previous section), and 340 μm chamber with two cover slips stacked, were used to measure fluorescence intensity of sodium fluorescein solutions, which were filled in the chambers by capillarity. The experiment instrument settings were the same as in *in vitro* linear calibration experiments as well as in *in vivo* permeability measurement (20× lens, NA = 0.75, 28% maximum illumination). With the concentration-depth product kept constant, the solutions of sodium fluorescein were diluted according to the different depth of the chambers (Yuan *et al*., 1993). The intensity was measured for a window area ~ 250 μm × 300 μm, and the focus was on the top surface of the solution. Results are shown in **Figure 2.6** Intensities for 50 μm and 100 μm deep chambers remained almost the same. However, for the chambers with depths larger than 100 μm, i.e. 170 μm and 340 μm chambers, the intensity decreased with increase of the depth of the chambers. The reason was that our experiment system can only collect the light from the solution in a smaller thickness region for the 170 μm and 340 μm chambers. Using a light collection index function defined in Yuan *et al*.

(1993), we did the curve fitting for the measured total intensity in the chambers of different depths (**Figure 2.6**). We found that within the depth of 95 μm (z_0 = 95μm in their index function), our imaging system can collect all the light. Beyond this depth, our system can collect the light either partially or none. This *in vitro* experiment indicated that the depth of light collection of our system was ~ 100 μm (Huxley *et al.*, 1987; Yuan *et al.*, 1993). Within this depth of the light collection, the fluorescence intensity is proportional to the total number of fluorescent molecules and is independent of the chamber depth. This narrow depth of light collection in our system allowed us to minimize the influence from the light coming from other parts of the brain tissue, especially from the meninges.

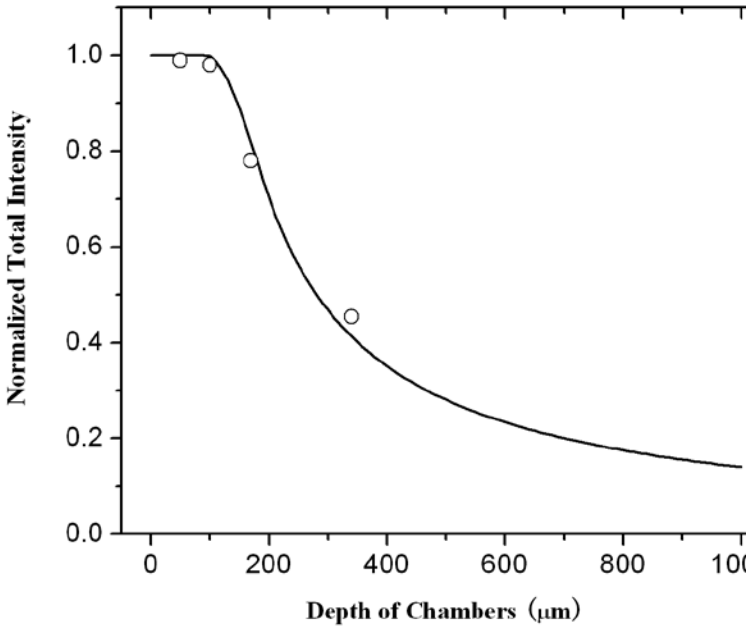

Figure 2.6 Depth of light collection. Samples of sodium fluorescein solution were prepared such that concentration-depth product was maintained constant. The total fluorescence intensity, which was normalized by the value for the 50 μm-depth chamber, was plotted for the chambers with the depth 50 μm, 100 μm, 170 μm and 340 μm. The continuous line is the curve fitting for the total intensity using a light collection index function in Yuan *et al.*, 1993.

Results and discussion

A summary of the apparent permeability P to various sized fluorescent tracers on individual post-capillary venules is shown in **Figure 2.7**. Two ROIs per vessel were measured for P, and the average was the permeability of that vessel. The average of 2.5 (± 0.8 SD, n = 55, ranging from 1 to 4 vessels per animal) vessels were measured for each animal. Total 22 animals were used in the study. The apparent permeability of sodium fluorescein, P^{NaF}, was 2.71 (±0.76, SD; n = 11) × 10^{-6} cm/s, ranging from 1.84 to 4.14 × 10^{-6} cm/s. The apparent permeability of FITC-dextran-4k, $P^{dextran\text{-}4k}$, was 0.92 (± 0.45, SD; n = 10) × 10^{-6} cm/s, ranging from 0.36 to 1.79 × 10^{-6} cm/s. The apparent permeability of FITC-dextran-10k, $P^{dextran\text{-}10k}$, was 0.31 (± 0.13, SD; n = 7) × 10^{-6} cm/s, ranging from 0.12 to 0.41 × 10^{-6} cm/s. The apparent permeability of FITC-dextran-20k, $P^{dextran\text{-}20k}$, was 0.24 (± 0.10, SD; n = 6) × 10^{-6} cm/s, ranging from 0.11 to 0.34 × 10^{-6} cm/s. The apparent permeability of FITC-dextran-40k, $P^{dextran\text{-}40k}$, was 0.19 (± 0.11, SD; n = 10) × 10^{-6} cm/s, ranging

from 0.07 to 0.38 × 10^{-6} cm/s. The apparent permeability of FITC-dextran-70k, $P^{\text{dextran-70k}}$, was 0.15 (±0.05, SD; n = 11) × 10^{-6} cm/s, ranging from 0.07 to 0.27 × 10^{-6} cm/s.

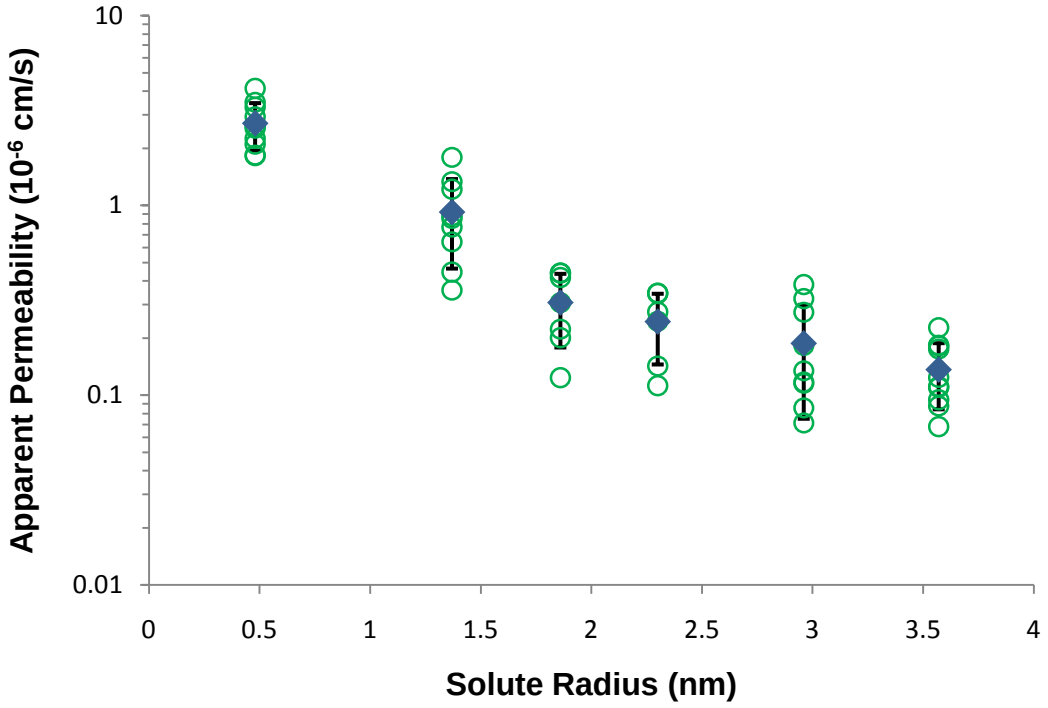

Figure 2.7 Apparent permeability P as a function of solute Stokes radius. Results for the individual microvessels (○) and mean values ± SD (■) are plotted.

Evaluation of methods: open vs. non-open skull measurements

Table 2.1 compares the permeability values measured with and without the skull. For open skull measurements, the frontoparietal bone (right or left),

~ 5 mm × 5 mm, was thinned with a micro-driller and removed (Easton *et al.*, 1997). The cerebral surface was exposed by cutting away the overlying meninges (**Figure 2.1c**). For non-open skull measurement, the frontoparietal bone was further thinned until it became soft and translucent (**Figure 2.1b**). To obtain the similar thickness of the thinned skull and keep the same other conditions for the rat brain, the time for skull grinding was kept as the same as possible between animals. The average time for grinding was 47 min (± 10 min SD, n = 22). In some experiments, the thinned part of the skull was peeled off and its thickness was measured by a confocal microscope (Leica TCS SP2, 40× objective lens with NA 1.25). The thinned part was quite uniform and the average thickness of 4 thinned skull samples was 87 μm (± 23 μm SD). We can see from the **Table 2.1** that the solute permeability measured in non-open skull preparation was slightly higher than that in open skull preparation, but not significant (probability levels $p > 0.3$). The possible reasons are: 1) The heat and/or inflammation due to the vibration from further thinning of the bone may induce a slight increase; 2) Even though the depth of the light collection of our system is narrow, the fluorescence from the vessels in meninges may enter into the measuring volume and slightly increase the $(dI/dt)_0$, the slope in **Figure 2.4**.

Table 2.1. Comparison of solute permeability P measured with and without the frontoparietal bone Values are means ± SD; n, number of vessels

Solutes	*P* with bone (x 10^{-6} cm/s)	*P* w/o bone (x 10^{-6} cm/s)	Significance Test p value
NaF	2.71 (±0.76), n=11	2.45 (±0.74), n=10	0.34
Dextran-10k	0.31 (±0.13), n=7	0.28 (±0.15), n=7	0.49
Dextran-20k	0.24 (±0.10), n=6	0.22 (±0.09), n=12	0.58
Dextran-40k	0.19 (±0.11), n=10	0.17 (±0.09), n=9	0.96
Dextran-70k	0.15 (±0.05), n=11	0.14 (±0.04), n=10	0.69

Easton *et al*. (1997) found that in the open skull measurement, after 20–60 min, the permeability *P* of the pial vessel to Lucifer Yellow increased and rose sharply in as soon as 44 min. In our non-open skull measurement, we compared *P* to sodium fluorescein and dextran 4k measured within 10 min and in 30–60 min after the skull was thinned. For 5 vessels, P^{NaF} was 2.50 (± 0.65 SD) × 10^{-6} cm/s measured in 10 min, and 2.59 (± 0.73 SD) × 10^{-6} cm/s in 30–60 min. No significant increase ($p > 0.8$). For another 5 vessels, $P^{dextran\ 4k}$ was 1.00 (± 0.26 SD) × 10^{-6} cm/s measured in 10 min, and 1.09 (± 0.33 SD) × 10^{-6} cm/s in 30–60 min, also no significant increase ($p > 0.6$). Therefore, non-open skull method provided a better preparation for longer term experiments.

Evaluation of methods: perfusion rate and RBCs

We chose the perfusion rate of 3 ml/min in injecting fluorescence solution through the carotid artery because 3 ml/min is the normal blood perfusion rate at the carotid artery for the rats we used in the experiments (Garcia-Villalon *et al*., 1992). Although we completely changed the blood to the fluorescence solution from the carotid artery at this perfusion rate, there was still residue blood in the pial microvessel. The red blood cells (RBC) of the blood would induce an underestimate of the fluorescence intensity in the lumen, ΔI_0 in **Figure 2.4**. We estimated that the red blood cell would account for 10% volume (Yuan *et al.*, 2009a) of the fluorescence solution in a pial microvessel at the perfusion rate of 3 ml/min from the carotid artery. The measured lumen fluorescence intensity would be only 90% of that of the effective solution. The effective solution means that the solute in the solution can travel across the vessel wall. The underestimated lumen intensity ΔI_0 would induce an 11% overestimation in the measured P. The corrected P for the influence of the red blood cells is shown in **Table 2.2**.

Table 2.2 Measured P and corrected P for the RBC, the free dye and the solvent drag

Solutes	No. of vessels	*P* (measured) (x 10^{-6} cm/s)	*P* (corrected for RBC) (x 10^{-6} cm/s)	*P* (corrected for RBC and free dye) (x 10^{-6} cm/s)	*P* (corrected for RBC, free dye and the solvent drag) (x 10^{-6} cm/s)
NaF	11	2.71 ± 0.76	2.43 ± 0.68	2.43 ± 0.68	2.43 ± 0.68
Dextran4k	10	0.92 ± 0.46	0.83 ± 0.41	0.82 ± 0.41	0.82 ± 0.40
Dextran10k	7	0.31 ± 0.13	0.28 ± 0.12	0.27 ± 0.11	0.26 ± 0.11
Dextran20k	6	0.24 ± 0.10	0.22 ± 0.09	0.21 ± 0.09	0.21 ± 0.08
Dextran40k	10	0.19 ± 0.11	0.17 ± 0.10	0.16 ± 0.10	0.16 ± 0.09
Dextran70k	11	0.15 ± 0.05	0.14 ± 0.05	0.13 ±0.04	0.13 ± 0.04

Values are means ± SD; RBC = red blood cells

Evaluation of methods: free dye associated with FITC-labeled dextrans

We chose FITC as the labeling fluorophore for dextrans with different molecular weights to obtain high quantum yield (ratio of the number of fluorescence photons emitted to the number of photons absorbed) with low light excitation. However, FITC (mol wt 389.4) diffuses through capillary walls much faster than FITC-dextrans (mol wt ranging from 4000 to 70,000). A small amount of the free FITC will cause a large overestimation of the permeability to FITC-dextran molecules. We therefore measured the amount of free dye in FITC-dextrans solutions. After being ultrafiltered by a clinical centrifuge (1750 rpm, 444 g) through a centricon filter (Millipore, 3000 mol. wt. cutoff) from the 1 mg/ml FITC-dextrans

solutions used in our experiments, the filtrate was checked for fluorescence intensity due to free FITC (I_f). The method for measuring I_f was the same as that described in the *in vitro* calibration, and the instrument settings were the same as those used for the *P* measurements. The ratio of free dye to original solutions was less than 0.3% for all 1 mg/ml FITC-dextrans solutions. If we use measured $P^{\text{sodium fluorescein}}$ (2.71×10^{-6} cm/s) for P^{FITC} of microvessels since the molecular weight of FITC (389.4) is very close to that of sodium fluorescein (376), provided that *P* is determined by solute size, we can estimate the free dye influence on $P^{\text{dextran-4k}}$, $P^{\text{dextran-10k}}$, $P^{\text{dextran-20k}}$, $P^{\text{dextran-40k}}$ and $P^{\text{dextran-70k}}$. By using the same method as in Appendix of Fu *et al.* (1998), $P^{\text{correct}} = [(1)/(1 - F)]P^{\text{measure}} - [(F) / (1 - F)]P^{\text{freedye}}$ (P^{measure} is the measured *P* for FITC-dextrans, P^{freedye} is P^{FITC}, $F = 0.3\%$ is the intensity ratio of free dye filtrate to original FITC-dextrans solutions, and P^{correct} is the corrected *P* for dextrans), we estimated that free FITC dye would lead to an overestimation for $P^{\text{dextran-4k}}$ by 0.7%, $P^{\text{dextran-10k}}$ by 2.7%, $P^{\text{dextran-20k}}$ by 3.4%, $P^{\text{dextran-40k}}$ by 4.5%, and $P^{\text{dextran-70k}}$ by 5.7%. The corrected *P* values for the free dye are shown in **Table 2.2**.

Effects of polydispersed dextrans

We purchased the FITC-dextrans from Sigma and used Zetasizer Nano ZS (Malvern Instruments Ltd, UK) to measure the molecular weight distributions of 3 largest dextrans in our study: dextrans-20k, -40k and -70k (**Figure 2.8**). Since the dextrans are polydispersed, the components that are lighter than the average-weight would induce an overestimation in the overall permeability for the polydispersed polymer of the average-weight, while the components that are heavier would induce

an underestimation in the overall permeability. **Figure 2.8** shows that the lightest component of dextran-70k (11%) has similar molecular weight of the average-weight dextran-40k, and the lightest component of dextran-40k (6.1%) has similar molecular weight of the average-weight dextran-20k. We used the same formula for the free dye effect (see previous section) and the measured $P^{\text{dextran-40k}}$ (corrected for the free dye) to calculate the overestimation of $P^{\text{dextran-70k}}$ due to the size overlap. It is 3.1%. We used the measured $P^{\text{dextran-20k}}$ to calculate the overestimation of $P^{\text{dextran-40k}}$. It is only 2.1%. If we consider the underestimation of larger components for the dextran permeability, the overall overestimation will be less than these values.

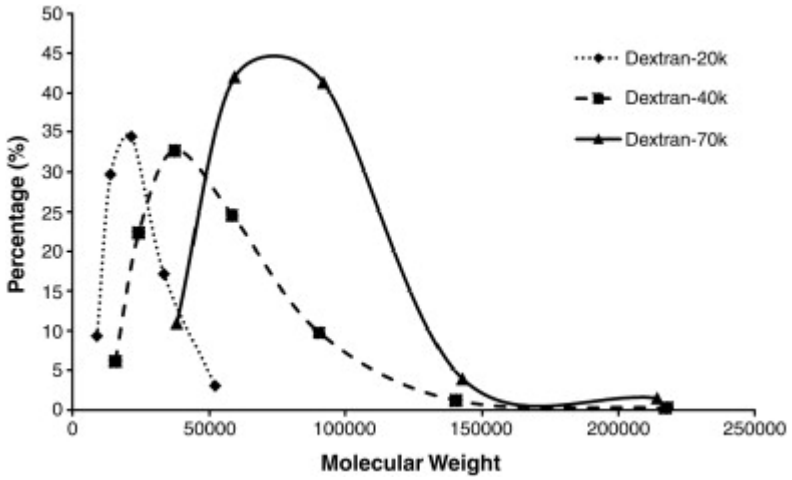

Figure 2.8 Molecular weight distributions of polydispersed dextrans.

Solvent drag contribution to the permeabilities for intermediate-sized and large molecules

Since solute flux can be coupled to water flow (solvent drag), the permeability coefficient *P* measured in our experiments (apparent permeability) tends to

overestimate the true diffusive permeability (P_d) of intermediate-sized and large molecules. Using the hydraulic conductivity L_p value of the frog pial microvessel, 2.0×10^{-9} cm/s/cm H_2O, which was measured in Fraser *et al*. (1990), we calculated the diffusive permeability P_d for FITC-dextrans (the data are summarized in **Table 2.2**) by employing the following formula in (Curry and Frokjaer-Jensen, 1984; Fu *et al.*, 1998; Fu *et al.*, 2003),

$$P = P_d \frac{\mathrm{P_e}}{\exp(\mathrm{P_e}) - 1} + L_p(1-\sigma)\Delta p_{\mathrm{eff}} \quad (1)$$

$$\mathrm{P_e} = \frac{L_p(1-\sigma)\Delta p_{\mathrm{eff}}}{P_d} \quad (2)$$

$$\Delta p_{\mathrm{eff}} = \Delta p - \sigma^{\mathrm{albumin}}\ \Delta\pi^{\mathrm{albumin}}\ - \sigma^{\mathrm{FITC-solute}}\ \Delta\pi^{\mathrm{FITC-solute}} \quad (3)$$

Here L_p is the hydraulic conductivity of the microvessel, σ is the reflection coefficient of the microvessel to the solute, and Δp_{eff} is the effective filtration pressure across the microvessel wall. Δp and $\Delta\pi$ are the hydrostatic and oncotic pressure drops across the microvessel wall, respectively. Superscript FITC-solute can be either FITC-dextran-4k, FITC-dextran-10k, FITC-dextran-20k, FITC-dextran-40k, or FITC-dextran-70k.

Since no data were reported for the reflection coefficients of rat pial microvessel to FITC-dextrans, we estimated the reflection coefficients to dextrans based on those found in rat mesenteric microvessels to albumin (mot. wt. 67,000) and α-lactalbumin (mot. wt. 14,176). $\sigma^{\mathrm{albumin}}$ and $\sigma^{\alpha\text{-lactalbumin}}$ of the rat mesenteric microvessel are 0.94 (Kendall and Michel, 1995) and 0.4 (Michel and Curry, 1999), respectively. Therefore, $\sigma^{\mathrm{dextran\text{-}70k}}$ was assumed as 0.94, as the size of dextran-70k

should be very close to the size of albumin, and $\sigma^{\text{dextran-40k}}$, $\sigma^{\text{dextran-20k}}$, $\sigma^{\text{dextran-10k}}$ and $\sigma^{\text{dextran-4k}}$ were assumed as 0.6, 0.5, 0.3, and 0.2, respectively. In the calculation, Δp in the rat pial microvessel was ~ 10 cm H_2O (Mayhan and Heistad, 1986). $\Delta\pi^{\text{albumin}}$ was 3.6 cm H_2O for 10 mg/ml BSA. Using these parameters, the diffusive permeability of dextran-4k $P_d^{\text{dextran-4k}}$ was calculated as 0.82×10^{-6} cm/s, which was 99% of its corrected apparent permeability (corrected for the RBC and the free dye); the diffusive permeability of dextran-10k, $P_d^{\text{dextran-10k}}$, was 0.26×10^{-6} cm/s, which was 97% of its corrected apparent permeability; the diffusive permeability of dextran-20k, $P_d^{\text{dextran-20k}}$, was calculated as 0.21×10^{-6} cm/s, which was 97% of its corrected apparent permeability; the diffusive permeability of dextran-40k, $P_d^{\text{dextran-40k}}$, was calculated as 0.16×10^{-6} cm/s, which was 97% of its corrected apparent permeability; and the diffusive permeability of dextran-70k, $P_d^{\text{dextran-70k}}$, was calculated as 0.13×10^{-6} cm/s, which was 99% of its corrected apparent permeability. If the reflection coefficient of the pial microvessel is estimated as 0.99 instead of 0.94, the difference in corrected $P_d^{\text{dextran-70k}}$ is 0.47%.

Comparison of P of the pial microvessel and P of the mesenteric microvessel

In **Figure 2.9**, we plot the diffusive permeability of the rat pial and mesenteric microvessels to various sized solutes. The measured permeability data for rat mesenteric microvessels are from Fu and Shen (2004) for a small molecule, sodium fluorescein, an intermediate-sized molecule, α-lactalbumin and a large molecule, albumin. **Figure 2.9** shows that the solute permeability of rat pial microvessels is about an order of magnitude lower than that of rat mesenteric microvessels, from 1/11

for a small solute, sodium fluorescein, to 1/6 for a large solute, albumin or dextran 70k. We also plotted the permeability data for a small molecule, Lucifer Yellow (mol. wt. 457), measured by (Easton and Fraser, 1994) and (Easton *et al*., 1997) using an open-skull method. We can see from **Figure 2.9**, there is a good agreement between Easton and Fraser's data and our results from a non-invasive measurement.

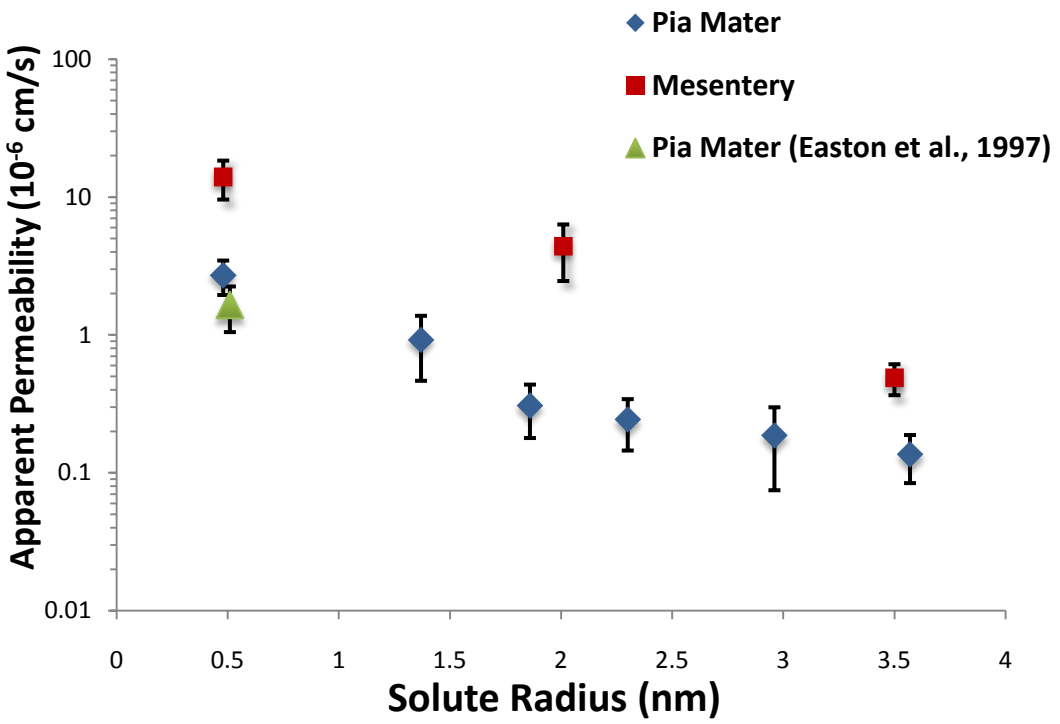

Figure 2.9 Comparison of solute permeability P for rat pial microvessels (♦Current study; ▲ Easton *et al.*, 1997) with that for rat mesenteric microvessels (■) (Fu and Shen, 2004). Values are means ± SD.

In summary, we developed a non-invasive method for measuring solute permeability in rat pial microvessels. This non-invasive method overcomes the disadvantage of previous *in vivo* methods due to exposing the brain tissue to the atmosphere, which induces the increase in microvessel permeability in longer time experiments. We will use this method in the future to quantify the cerebral microvessel permeability changes due to varied physiological and pathological conditions and to develop better strategies for drug delivery across the blood–brain barrier.

CHAPTER 3 CHARGE EFFECTS OF THE BBB ON SOLUTE TRANSPORT *IN VIVO*

Introduction

The blood-brain barrier (BBB) is a regulatory interface between the cerebral circulation and the brain tissue, and it is essential for protecting the central nervous system (CNS) from blood-borne neuroactive solutes (Smith, 2000). This barrier is composed of an endothelial layer with embedment of pericytes at irregular intervals with the complete wrapping of the basement membrane, which is ensheathed by astrocyte foot processes (Nicolazzo *et al.*, 2006). A simplified sketch for the cross-sectional view of the BBB is shown in **Figure 3.1A**. At the luminal surface of the endothelium, there is a fluffy glycocalyx layer (Ueno *et al.*, 2004a), and this mucopolysaccharide structure is highly hydrated in electrolytic solution and contains large numbers of solid-bound fixed negative charges due to its constituents with abundance in glycoproteins, acidic oligosaccharides, terminal sialic acids, proteoglycan, and glycosaminoglycans aggregates (Tarbell and Pahakis, 2006). The endothelium and pericytes are surrounded by a uniform and very narrow matrix-like basement membrane, which consists of collagen type IV, heparin sulfate proteoglycans, laminins, fibronectin, and other extracellular matrix proteins, and thus contains a great number of negative charges (del Zoppo and Hallenbeck, 2000; Hamann *et al.*, 1995; Leblond and Inoue, 1989; Miosge, 2001). Finally, this basement membrane is wrapped by the end-feet of astrocytes, one type of glial cells in the brain

(Farkas and Luiten, 2001). The unique structure and compositions of the BBB determine its low permeability to water and solutes.

Increased permeability of the BBB has been observed in association with the disruption of the basement membrane in pathological states (Rascher *et al.*, 2002; Rosenberg *et al.*, 1993). Because of the distinct location of the basement membrane in the trans-BBB pathway as well as its polyanionic nature, it is necessary to examine if the basement membrane plays an important role in the maintenance of the normal permeability and selective properties of the BBB, in addition to the endothelial surface glycocalyx and tight junctions between endothelial cells. **Figure 3.1B** demonstrates an enlarged view of the endothelial surface glycocalyx, inter-endothelial cleft, tight junction strands, basement membrane and the astrocyte foot processes of the BBB. The charge density of the endothelial surface glycocalyx is denoted as C_{mf} and that of the basement membrane, C_{mb}. Up to date, no detailed quantitative data and models that investigate the role of the BBB structure and compositions, especially the contribution of the charge carried by the endothelial surface glycocalyx and basement membrane to the permeability of the BBB to the charged molecules and particles. One objective of our study is to predict the charge densities C_{mf} and C_{mb} of the rat pial cerebral microvessel by combining *in vivo* solute permeability measurements and a mathematical model for the transport across the BBB (Fu *et al.*, 2008).

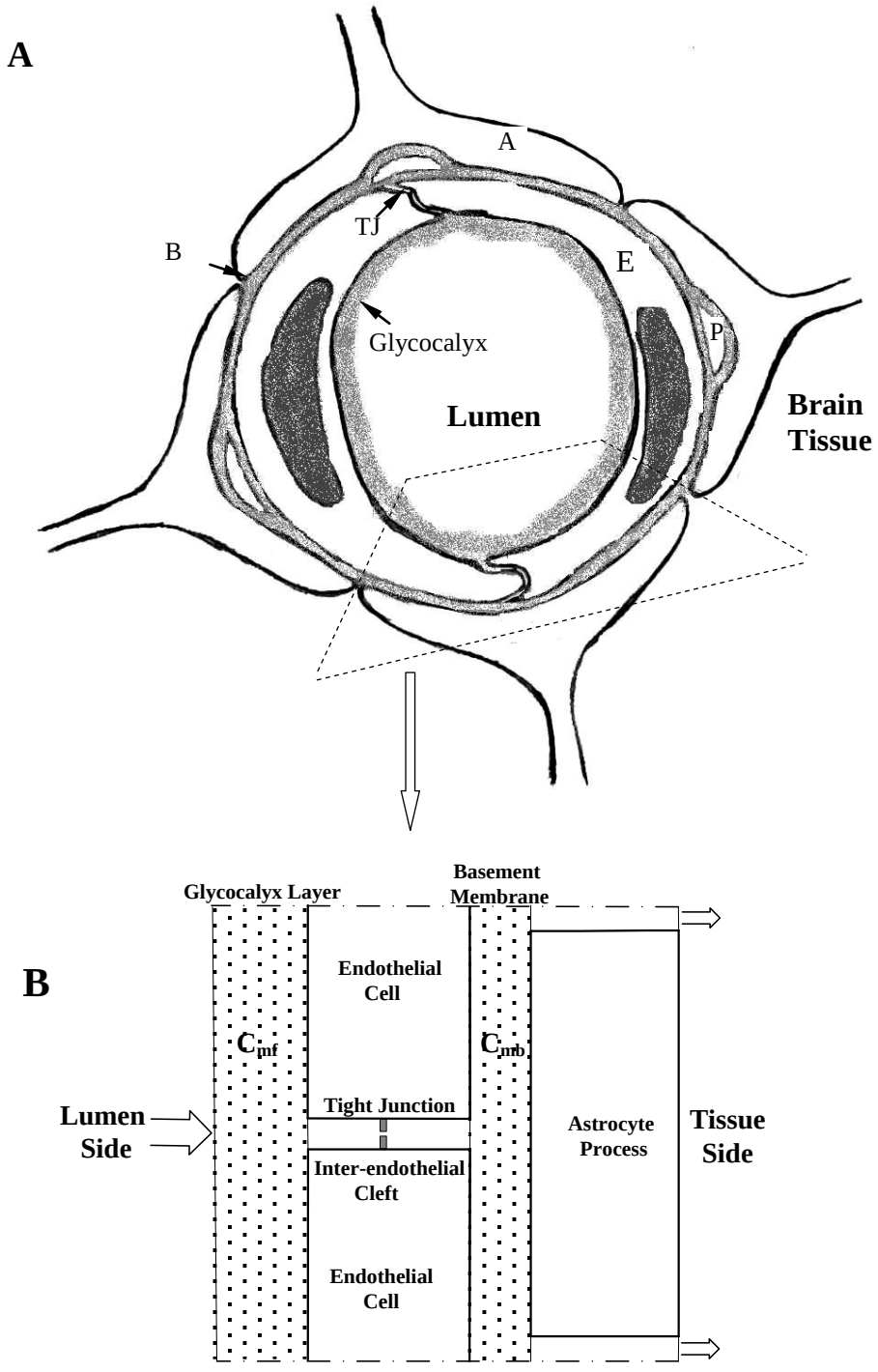

Figure 3.1 (A) The cross-sectional view of the sketch for the blood-brain barrier (BBB) (not in scale), which is formed by the endothelium (EC), surrounding

basement membrane (BM) and astrocyte foot process (A) and pericytes (p). At the luminal surface of the endothelium, there is a glycocalyx layer. In between endothelial cells, there is an interendothelial cleft with the tight junction strand (TJ). At the abluminal side of the endothelium, a basement membrane separates the endothelium and the ensheathing astrocyte foot processes (Allt and Lawrenson, 1997a; Cassella *et al.*, 1997; Farkas and Luiten, 2001; Paulson and Newman, 1987; Schulze and Firth, 1992b). **(B)** Plane view of the BBB. T*he endothelial surface glycocalyx and basement membrane carry negative charge* due to their matrix compositions (del Zoppo and Hallenbeck, 2000; Hamann *et al.*, 1995; Leblond and Inoue, 1989; Miosge, 2001; Ueno *et al.*, 2004a). We denote charge density C_{mf} for the surface glycocalyx and C_{mb} for the basement membrane, respectively.

By measuring permeability to similar-sized solutes, α-lactalbumin and ribonuclease (Stokes radius ~2 nm), of which, the former carries a negative charge of -11 and the latter carries a positive charge of +3, Adamson *et al*. (Adamson *et al.*, 1988) found that the endothelial surface glycocalyx of frog mesenteric microvessels has negative charge with estimated charge density of 11.4 mEq/L. Huxley *et al.* (Huxley *et al.*, 1993) showed that permeability to α-lactalbumin was lower during exposure to plasma than that during exposure to bovine serum albumin (BSA), but there was no change in hydraulic conductivity. Curry *et al*. (Curry *et al.*, 1989) further observed that the permeability of frog mesenteric microvessels to negatively charged molecule, α-lactalbumin, decreased with addition of a plasma polyanionic glycoprotein, orosomucoid, at the concentration as low as 0.1 mg/ml while hydraulic

conductivity did not change. On the basis of these observations on frog mesenteric microvessels, (Fu *et al.*, 2003) developed a mathematical model to explain the charge effect of the endothelial surface glycocalyx on microvessel permeability to water and charged molecules. Their model predicted that the charge density of surface glycocalyx of frog mesenteric capillaries was ~30 mEq/L under normal conditions. Addition of the plasma would increase this charge density by 2.4-fold, while 0.1 mg/ml orosomucoid would increase the glycocalyx charge density by 2.2-fold in frog mesenteric microvessels.

Orosomucoid, or α_1-acid glycoprotein, is known to be an acute phase protein with the molecular weight of ~40 kDa and the dimension of ~3 × 3 × 6 nm (Predescu *et al.*, 1998), and its plasma concentration is 0.1-1.1 mg/ml (Schnitzer and Pinney, 1992). It has been reported that the orosomucoid level increases several folds during infection or trauma (Kremer *et al.*, 1988; Matsumoto *et al.*, 2007). In addition, it has been demonstrated that orosomucoid molecules bound to the microvascular endothelial cells *in vitro* (Schnitzer and Pinney, 1992). Haraldsson and Rippe (Haraldsson and Rippe, 1987) showed that circulating orosomucoid reduced the trans-vascular leakage of albumin in the isolated perfused rat hindquarter when added to a Ringer-albumin perfusate. This study, along with the study by Curry *et al*. (Curry *et al.*, 1989) and observation by (Matsumoto *et al.*, 2007), indentified a specific plasma protein, which contributes to the maintenance of stable solute permeability of microvessels by modulating the charge of microvessel walls.

However, the effect of orosomucoid on the permeability properties of the mammalian peripheral as well as cerebral microvessels, have not been examined so far. Therefore, another objective of our study is to test the hypothesis that addition of orosomucoid to a Ringer-albumin perfusate enhances the transport of cationic solutes across the BBB but decreases that of anionic solutes by altering the charge density of the endothelial surface glycocalyx and that of the basement membrane of the BBB. To do this, we measured the apparent permeability of rat pial microvessels, in the absence and presence of orosomucoid, to FITC-α-lactalbumin and FITC-ribonuclease, which have almost same size (Stokes radius ~2 nm), but opposite charge (net charge of -11 and +3, respectively), as well as FITC-BSA (Stokes radius ~3.5 nm, net charge of -19). In order to determine the charge density of the endothelial surface glycocalyx, C_{mf}, of the rat microvessels (mesenteric and pial) and its alteration by orosomucoid, we also did paired measurements of apparent permeability of rat mesenteric post-capillary venules to these three solutes in the absence and presence of orosomucoid. Combining the *in vivo* measured permeability data and a theoretical model, which was developed recently from our group (Fu *et al.*, 2008), we could predict the charge densities C_{mf} and C_{mb} of the glycocalyx layer and the basement membrane in the BBB under normal conditions and under orosomucoid treatment.

Materials and methods

General preparation

All *in vivo* experiments were performed on adult female Sprague-Dawley rats (250-300 g) supplied by Hilltop Laboratory Animals (Scottdale, PA). All procedures and the animal use have been approved by the Institutional Animal Care and Use Committee at the City College of New York. The rats (age 3-4 months) were anesthetized with pentobarbital sodium given subcutaneously. The initial dosage was 65 mg/kg, and additional 3 mg/dose was given when needed. The rats were kept warm on a heating pad. The animals were prepared for two groups. One group was prepared for the measurement of the permeability of pial microvessels, and the other was for the measurement of the permeability of mesenteric microvessels. The methods for two types of the preparation are given below.

Preparation for the measurement of pial microvessel permeability

The detailed description of the method has been described in **Chapter 2**. A brief outline is given with emphasis of special features in the current experiments. A section of the left frontoparietal bone, approximately ~5 mm × ~5 mm, was carefully ground with a micro-grinder, until the area in the middle (~2 mm x ~2 mm) became soft and translucent. The blood vessels could be seen under a 16× dissection microscope. During the process, artificial cerebrospinal fluid (ACSF) with the room temperature was applied to the surface of the skull to remove the heat due to grinding. The pial microvessels in this thinned section were observed under an inverted microscope. The fluorescent solution was introduced into the cerebral circulation by a

syringe pump at a constant rate of 3 ml/min. The images of the pial post-capillary venules (20-40μm in diameter) and nearby brain tissue were simultaneously collected by a CCD camera connected to a computer.

Preparation for the measurement of mesenteric microvessel permeability

The detailed description of the method was published elsewhere (Yuan *et al.*, 2009b). Briefly, after anaesthetization, the rat was transferred on a heating pad, and the mesentery was then gently taken out from the abdominal cavity and arranged on the surface of a polished quartz pillar (~2 cm in diameter; New Port Glass, Costa Mesa, CA). This arrangement was to maintain the circulation to the gut and mesentery of the animal and also allowed the trans-illumination of the mesenteric microvasculature. The upper surface of the mesentery was continuously superfused with Ringer solution at 37°C at the rate of ~4 ml/min, which kept the layer of fluid over the tissue at approximately constant depth. The permeability measurement was made on straight non-branched post-capillary venules (25-40μm in diameter). All microvessels had brisk blood flow immediately before cannulation and had no marginating white cells. A double-barreled θ pipette (Fu *et al.*, 2005) was used to cannulate the microvessel. The detailed illustration of using θ pipette cannulation in the permeability measurement has been given in (Fu and Shen, 2004). Briefly, the microvessel was cannulated using a θ pipette, two channels of which contained either the washout solution containing no fluorescent solute or the test solution containing the fluorescent solute. This allowed alternate perfusion of the cannulated microvessel with a washout solution or the dye solution. Each channel of the θ pipette was

connected to a water manometer, which enabled perfusion at known pressures. In the study, the pressure in the microvessel was estimated to be 10-20cm H_2O as determined by balancing the interface between fluorescent and non-fluorescent solutions within the non-flowing channel of the θ pipette. The images of the microvessel and surrounding tissue were recorded during the perfusion for later offline fluorescence intensity analysis.

Solutions and fluorescent test solute preparation

Mammalian Ringer solution

Mammalian Ringer solution was used for all perfusates (Fu and Shen, 2004). The solution composition was (in mM) NaCl 132, KCl 4.6, $MgSO_4$ 1.2, $CaCl_2$ 2.0, $NaHCO_3$ 5.0, glucose 5.5, and HEPES 20. All these chemicals were from Sigma. The pH was buffered to 7.4–7.45 by adjusting the ratio of HEPES acid to base. The solutions were made fresh on the day of use to avoid binding to the serum albumin (Adamson *et al.*, 1994; Fu *et al.*, 1998).

Artificial Cerebrospinal Fluid (ACSF)

The ACSF solution composition was (in mM) NaCl 110.5, KCl 4.7, $CaCl_2$ 2.5, KH_2PO4 1.1, $MgSO_4$•7H2O 1.25, $NaHCO_3$ 25 and HEPE 15 (Easton *et al.*, 1997), and the solution was buffered to pH 7.4 ± 0.5. All chemicals were obtained from Sigma.

Fluorescence labeling BSA, α-lactalbumin and ribonuclease

FITC-labeled BSA (A9771, Sigma) was directly purchased from Sigma, while α-lactalbumin (L6010, Sigma) and ribonuclease A (R5500, Sigma) were labeled with FITC (F7250, Sigma, mol. wt. 389.4) as follows (Adamson *et al.*, 1988; Fu *et al.*, 1998). Protein (90 mg) was dissolved in 15 ml of borate buffer (0.05 M, pH approximately 9.3, 20°C) containing 0.4 M NaCl. The solution was placed in 18-mm-diameter dialysis tubing (Spectrum Medical Industries, 3500 mol. wt. cutoff) and was then dialyzed for 12 hours with constant stirring at 15°C against 50 ml of the borate buffer containing FITC (0.5 mM). The labeled protein then was dialyzed against 2 liters of glucose-free mammalian Ringer solution twice, each round for 12 hours. The dialysis procedure was then performed twice with 2 liters of normal Ringer solution until there was no free dye. The influence of the free dye on measured permeability to a labeled protein was discussed by (Fu *et al.*, 1998). The FITC-labeled α-lactalbumin and ribonuclease were stored frozen and used within 2 week of preparation, while FITC-BSA (purchased from Sigma) was made on the day of use. In addition, on the day of experiment, unlabeled 10 mg/ml BSA was added to aliquots of the labeled protein in the Ringer solution. The final FITC-α-lactalbumin, FITC-ribonuclease and FITC-BSA dye concentrations used in the experiment were 2 mg/ml in the Ringer-BSA solution. For this preparation, the fluorescence intensity of the free FITC dye was less than 1% of the solution, which was checked using the image system at the same instrument settings used in our *in vivo* experiments. All dye solutions described above were kept chilled until just before use and were discarded at the end of the day.

Microscope preparation

A detailed description of the microscope preparation used to measure *P* to fluorescently labeled solutes has been described in **Chapter 2**. Briefly, a Nikon TE2000-E inverted fluorescence microscope was used to observe either pial or mesenteric microvessels. In the measurement of *P* of rat pial microvessels, with the illumination of a monochromator (the xenon lamp as light source, FSM150Xe; Bentham, U.K.), the pial microvessels were observed with a 20× lens (NA = 0.75, Nikon), while in the measurement of *P* of rat mesenteric microvessels, the single perfused mesenteric microvessel was observed with a 10× lens (NA 0.3, Nikon). The excitation/emission wavelength was set 490 nm/520 nm for all FITC-labeled solutes in the study. The images were captured using a highly sensitive 12-bit Sensicam QE CCD camera (Cooke, MI) and then transferred to an imaging acquisition and analysis workstation.

Permeability measurement

When the dye was perfused into the microvessel either through the carotid artery for measuring the *P* of pial microvessels or through the cannulating micropipette for measuring the *P* of mesenteric microvessels, the images were recorded simultaneously. The *P* was determined off-line from the prerecorded images. The measuring windows for pial microvessels were at least 100-200 μm long and 40-100 μm wide (Yuan *et al.*, 2009b), while the measuring windows for mesenteric microvessels were generally 300-400 μm long and 100-200 μm wide (Fu

and Shen, 2004). In this way, the solute permeability coefficient *P* can be determined from the relationship $P = (1/\Delta I_0)(dI/dt)_0$ (r/2), where ΔI_0 is the step increase in fluorescence intensity in the measuring window as the test solute fills the microvessel lumen, $(dI/dt)_0$ is the initial rate of increase in fluorescence intensity after the solute fills the lumen and begins to accumulate in the tissue, and *r* is the vessel radius (Adamson *et al.*, 1988; Fu *et al.*, 1998; Fu and Shen, 2004). **Figure 3.2** shows typical curves of fluorescence intensity vs. time for three test solutes under control and orosomucoid treatment. The step increase ΔI_0 and the slope of the increasing curve $(dI/dt)_0$ are indicated in **Figure 3.2A**. We measured the diameter of the vessel and the total intensity of fluorescence in the lumen of the vessel segment from the recorded images and found no changes during the period in our experiments (up to 1 min). This indicates that there was no vasoreactivity, which may induce the change in the vessel radius.

For the control *P* measurement on the single cannulated mesenteric microvessel, the perfusate was 10 mg/ml BSA-Ringer on both washout and dye sides of the θ pipette. For the test measurement, the perfusate on both sides was changed to 10 mg/ml BSA-Ringer additionally containing 0.1 mg/ml orosomucoid (G3643, α_1-acid glycoprotein, Sigma). For the control *P* measurement of pial microvessels, the perfusate through the carotid artery was 10 mg/ml BSA-Ringer for both dye and washout solutions and it was changed to 0.1 mg/ml orosomucoid in Ringer-BSA for the test measurement. To test the effect of orosomucoid on solute permeability, the vessel was perfused with the orosomucoid perfusate without dye for 1 min (Curry *et*

al., 1989) before *P* was determined by averaging 2-3 measurements for that vessel in mesenteric microvessels, while 2 measurements on different segments were averaged for *P* of an individual vessel in pial microvessels.

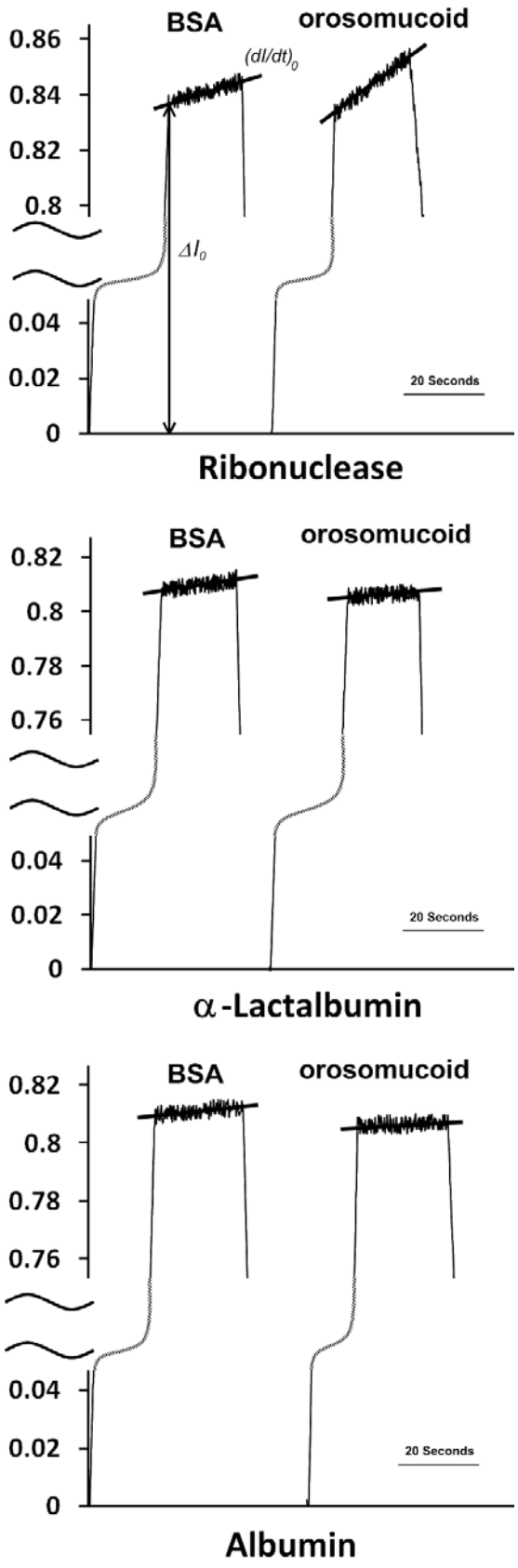

Figure 3.2 Typical curves of fluorescence intensity (normalized value) as a function of time for solute permeability (P) measurements on six individual pial microvessels of ~30μm diameter for three solutes perfused with either the Ringer-BSA (the left panels) or orosomucoid in the Ringer-BSA (the right panels): (A) P of ribonuclease, which were 3.51×10^{-7} cm/s (BSA) and 9.41×10^{-7} cm/s (orosomucoid), respectively; (B) P of α-lactalbumin, which were 1.62×10^{-7} cm/s (BSA) and 0.67×10^{-7} cm/s (orosomucoid), respectively; and (C) P of BSA, which were 1.54×10^{-7} cm/s (BSA) and 0.45×10^{-7} cm/s (orosomucoid), respectively.

Analysis and statistics

Two to three *P* measurements during perfusion of test solutes in a vessel were averaged to establish a single value for *P* of that vessel under either control with Ringer-BSA perfusate or treatment with orosomucoid for mesenteric microvessels, while 2 measurements on different segments were averaged for *P* of an individual vessel for pial microvessels. All data were presented as means ± SE. Data were analyzed for statistical significance using ANOVA. Significance was assumed for probability levels $p < 5\%$.

Results

Apparent permeability (P) of pial microvessels to charged solutes during Ringer-BSA and orosomucoid-Ringer-BSA perfusion

The apparent permeability coefficients (*P)* to three charged solutes, FITC-α-lactalbumin, FITC-ribonuclease, and FITC-BSA, were measured on different pial post-capillary venules under control with Ringer-BSA perfusate and treatment with orosomucoid-Ringer-BSA perfusate. Two ROIs per vessel were measured and the averaged value was given as the *P* of that vessel. Total 60 vessels on pia mater were measured in 29 rats. For the control group with the Ringer-BSA perfusate, the mean value for *P* to negatively charged α-lactalbumin ($P^{\alpha\text{-}lactalbumin\ ,BSA}$) was 1.54 ± 0.35 (SD) × 10^{-7} cm/s (n = 11, ranging from 0.85 to 2.01 × 10^{-7} cm/s) and that to positively charged ribonuclease ($P^{ribonuclease,\ BSA}$) was 6.23 ± 2.04 (SD) × 10^{-7} cm/s (n = 13, ranging from 3.01 to 8.87 × 10^{-7} cm/s), although they have similar size (Stokes radius

~2 nm). The mean value of P to a larger negatively charged solute BSA (Stokes radius ~3.5 nm) ($P^{albumin,\ BSA}$) was 1.05 ± 0.30 (SD) × 10^{-7} cm/s (n = 10, ranging from 0.60 to 1.54 × 10^{-7} cm/s). For the treatment group with orosomucoid perfusate, the mean value for P to α-lactalbumin ($P^{\alpha\text{-}lactalbumin\ ,orosomucoid}$) was 0.87 ± 0.20 (SD) × 10^{-7} cm/s (n = 9, ranging from 0.54 to 1.23 × 10^{-7} cm/s) and the mean value of P to ribonuclease ($P^{ribonuclease,\ orosomucoid}$) was 9.42 ± 1.77 (SD) × 10^{-7} cm/s (n = 11, ranging from 5.81 to 11.65 × 10^{-7} cm/s). The mean value of P to BSA ($P^{albumin,\ orosomucoid}$) was 0.61 ± 0.13 (SD) × 10^{-7} cm/s (n = 6, ranging from 0.45 to 0.87 × 10^{-7} cm/s). The measured data were summarized in **Table 3.1**. On average, in the absence of orosomucoid, P to positively charged ribonuclease was four times as large as that to negatively charged α-lactalbumin, $P^{ribonuclease,\ BSA}/P^{\alpha\text{-}lactalbumin,\ BSA}$ = 4.0. In the presence of orosomucoid, however, this ratio was significantly greater than that when the orosomucoid was absent, $P^{ribonuclease,\ orosomucoid}/P^{\alpha\text{-}lactalbumin,\ orosomucoid}$ = 10.8. The ratios of the apparent permeability of pial microvessels in the presence to that in the absence of orosomucoid are: $P^{albumin,\ orosomucoid}/P^{albumin,\ BSA}$ = 0.58, $P^{\alpha\text{-}lactalbumin,\ orosomucoid}/P^{\alpha\text{-}lactalbumin,\ BSA}$ = 0.56, and $P^{ribonuclease,\ orosomucoid}/P^{ribonuclease,\ BSA}$ = 1.51. The decrease in P to negatively charged solutes and the increase in P to a positively charged solute in the presence of orosomucoid indicate that orosomucoid adds negative charge to the BBB.

Table 3.1 Measured P and corrected P of pial microvessels for the RBC, the free dye, and the solvent drag

Group	Solutes	No. of vessels	*P* (measured) ($\times 10^{-7}$ cm/s)	*P* (corrected for RBC) ($\times 10^{-7}$ cm/s)	*P* (corrected for RBC and free dye) ($\times 10^{-7}$ cm/s)	*P* (corrected for RBC, free dye, and solvent drag) ($\times 10^{-7}$ cm/s)
Control	α-lactalbumin	11	1.54 ± 0.35	1.39 ± 0.32	1.31 ± 0.25	1.29 ± 0.24
	Ribonuclease	13	6.23 ± 2.04	5.61 ± 1.84	5.55± 1.82	5.52 ± 1.81
	Albumin	10	1.05 ± 0.30	0.95 ± 0.28	0.88 ± 0.27	0.88 ± 0.07
Orosomucoid	α-lactalbumin	9	0.87 ± 0.20	0.78 ± 0.19	0.71 ± 0.19	0.68 ± 0.18
	Ribonuclease	11	9.42 ± 1.77	8.48 ± 1.58	8.43 ± 1.56	8.40 ± 1.55
	Albumin	6	0.61 ± 0.13	0.55 ± 0.11	0.48 ± 0.10	0.47 ± 0.10

Values are means ± SD; RBC = red blood cell.

Apparent permeability (P) of mesenteric microvessels to charged solutes during Ringer-BSA and orosomucoid-Ringer-BSA perfusion

Because there is charge in the endothelial surface glycocalyx and in the basement membrane of the BBB, to predict how much charge orosomucoid adds to these different structural components of the BBB, we also measured the *P* of mesenteric microvessels to these charged solutes in the presence and absence of orosomucoid. Although there is a basement membrane surrounding the mesenteric endothelium, it contributes much smaller resistance than that in the BBB because there are no wrapping astrocyte foot processes (Fu *et al*., 2008). Therefore, we can neglect the basement membrane in calculating permeability of mesenteric

microvessels and predict the charge density C_{mf} in the surface glycocalyx first by combining the measured *P* data with the model predictions (Fu *et al.*, 2003). An individual mesenteric post-capillary venule (25-40 μm in diameter) was cannulated with a θ-pipette. For the control measurement, two channels of the pipette were filled with either fluorescence solution or washout solution that contains Ringer-BSA. A series of 2-3 *P* measurements were repeated, and the averaged value was given as *P* for the control in that vessel. After the control measurements, the same vessel was recannulated with the second θ-pipette, with its two channels filled with same solutions but additionally containing 0.1 mg/ml orosomucoid. Before perfusion of the fluorescence solution for the *P* measurement, the vessel was perfused with washout solution containing orosomucoid for 1 minute (Curry *et al.*, 1989). Then, two or three consecutive measurements were repeated to obtain the average *P* for the orosomucoid treatment. Paired measurements were performed on seven vessels for each solute with total 21 vessels in 21 rats for 3 solutes, with one vessel per animal.

The mean values of *P* to negatively charged α-lactalbumin under control ($P^{\alpha\text{-}lactalbumin\ ,BSA}$) and orosomucoid treatment ($P^{\alpha\text{-}lactalbumin\ ,orosomucoid}$) were 23.3 ± 9.89 (SD) × 10^{-7} cm/s (n = 7, ranging from 9.66 to 34.9 × 10^{-7} cm/s) and 11.2 ± 4.43 (SD) × 10^{-7} cm/s (n = 7, ranging from 6.76 to 22.8 × 10^{-7} cm/s), respectively. The mean value of $P^{\alpha\text{-}lactalbumin,orosomucoid}$ to $P^{\alpha\text{-}lactalbumin,BSA}$ for the paired measurement was 0.52 ± 0.24 (SD) (ranging from 0.24 to 0.9). For positively charged ribonuclease, the mean values of *P* under control ($P^{ribonuclease\ ,BSA}$) and orosomucoid treatment ($P^{ribonuclease\ ,orosomucoid}$) were 44.8 ± 19.8 (SD) × 10^{-7} cm/s (n = 7, ranging from 3.42 to 66.0 × 10^{-7} cm/s) and

58.2 ± 22.5 (SD) × 10^{-7} cm/s (n = 7, ranging from 13.0 to 96.5 × 10^{-7} cm/s), respectively, and the mean value of $P^{ribonuclease\ ,orosomucoid}$ to $P^{ribonuclease\ ,BSA}$ for the paired measurement was 1.64 ± 0.81 (SD) (ranging from 0.78 to 3.80). The mean value of *P* to albumin under control ($P^{albumin\ ,BSA}$) and orosomucoid treatment ($P^{albumin\ ,orosomucoid}$) were 7.47 ± 2.03 (SD) × 10^{-7} cm/s (n = 7, ranging from 4.57 to 11.1 × 10^{-7} cm/s) and 3.95 ± 1.40 (SD) × 10^{-7} cm/s (n = 7, ranging from 1.25 to 5.16 × 10^{-7} cm/s), respectively, and the mean value of $P^{albumin\ ,orosomucoid}$ to $P^{albumin\ ,BSA}$ for the paired measurement was 0.54 ± 0.24 (SD) (ranging from 0.27 to 0.83). **Table 3.2** summarized the measured data. For rat mesenteric microvessels, $P^{ribonuclease\ ,BSA}/P^{\alpha\text{-}lactalbumin\ ,BSA}$ = 1.92 in the absence of orosomucoid, while in presence of orosomucoid, $P^{ribonuclease\ ,BSA}/\ P^{\alpha\text{-}lactalbumin\ ,BSA}$ = 5.2. These ratios are smaller than those in the BBB, suggesting that there is significant negative charge in the basement membrane of the BBB, in addition to the endothelial surface glycocalyx.

Table 3.2 Measured P and corrected P of mesenteric microvessels for the free dye and the solvent drag

Group	**Solutes**	**No. of vessels**	***P*** **(measured)** **(× 10^{-7} cm/s)**	***P*** **(corrected for free dye)** **(× 10^{-7} cm/s)**	***P*** **(corrected for free dye and solvent drag)** **(× 10^{-7} cm/s)**
Control	α-lactalbumin	7	23.3 ± 9.89	22.9 ± 9.82	21.4 ± 9.82
	Ribonuclease	7	44.8 ± 19.8	44.5 ± 19.6	43.0 ± 19.6
	Albumin	7	7.47 ± 2.03	7.07 ± 1.98	6.92 ± 1.98
Orosomucoid	α-lactalbumin	7	11.2 ± 4.43	10.8 ± 4.40	9.21 ± 4.40
	Ribonuclease	7	58.2 ± 22.5	58.0 ± 22.3	56.5 ± 22.0
	Albumin	7	3.95 ± 1.40	3.54 ± 1.40	3.39 ± 1.35

Values are means ± SD.

Discussion

Evaluation of methods: perfusion rate, RBCs, and free dye associated with FITC-labeled solutes

In the pial microvessel solute permeability measurement, a normal blood perfusion rate of 3 ml/min in the common carotid artery was chosen in injecting fluorescence solution (Yuan *et al.*, 2009b). Although the blood was completely replaced by fluorescence solution from the carotid artery at this perfusion rate, there was still residue blood in the pial microvessel, in which red blood cells (RBCs) would induce an underestimate of the fluorescence intensity in the lumen (ΔI_0). This underestimated lumen intensity ΔI_0 would induce ~10% overestimation in the measured P as we predicted in our previous study (Yuan *et al.*, 2009b). The corrected P for the influence of the RBCs was shown in **Table 3.1**.

We chose FITC as the labeling fluorophore for α-lactalbumin, ribonuclease, and albumin to obtain high quantum yield (ratio of the number of fluorescence photons emitted to the number of photons absorbed) with low light excitation. Since FITC (mol. wt. 389.4) diffuses through microvessel walls much faster than α-lactalbumin (mol. wt. 14,176), ribonuclease (mol. wt. 13,700), and albumin (BSA, mol. wt. 69,000), a small amount of the free FITC would cause a large overestimation of the permeability to intermediate and large sized molecules. We therefore measured the amount of free dye in our labeled α-lactalbumin and ribonuclease solutions as well as commercial FITC-albumin obtained from Sigma. After being ultrafiltered by a

clinical centrifuge (1750 rpm, 444 g) through a centricon filter (Millipore, 3000 mol. wt. cutoff) from the 2 mg/ml FITC-α-lactalbumin, FITC-ribonuclease, or FITC-BSA solutions used in our experiments, the filtrate was checked for fluorescence intensity due to free FITC (I_{ff}). The method for measuring I_{ff} was the same as that described in the *in vitro* calibration and the instrument settings were the same as those used for the *P* measurements. The ratio of free dye to original solutions was approximately 0.3% for all 2 mg/ml FITC-α-lactalbumin, FITC-ribonuclease and FITC-albumin solutions. If we use measured $P^{sodium\ fluorescein}$, 2.71×10^{-6} cm/s for pial microvessels (Yuan *et al.*, 2009b), 1.4×10^{-5} cm/s for mesenteric microvessels (Fu and Shen, 2004), for P^{FITC} of microvessels since the molecular weight of FITC (389.4) is very close to that of sodium fluorescein (376), provided that *P* is determined by solute size, we can estimate the free dye influence on $P^{\alpha\text{-}lactalbumin}$, $P^{ribonuclease}$, and $P^{albumin}$. By using the same method as in the appendix of Fu *et al*. (Fu *et al.*, 1998), we estimated that 0.3% free FITC dye would lead to an overestimation in $P^{\alpha\text{-}lactalbumin}$ of pial microvessel by 5.7% under control and by 9.0% under orosomucoid treatment, while in that of mesenteric microvessels, by 1.7% and 3.5%, respectively. The overestimation in $P^{ribonuclease}$ of pial microvessels was 1% under control and 0.6% under orosomucoid treatment, while in that of mesenteric microvessels was 0.6% and 0.4%, respectively. Finally, the overestimation in $P^{albumin}$ of pial microvessels was 7.4% under control and 13.0% under orosomucoid treatment, while in that of mesenteric microvessels was 5.3% and 10.3%, respectively (**Tables 3.1** and **3.2**).

Solvent drag contribution to $P^{\alpha\text{-lactalbumin}}$, $P^{ribonuclease}$, and $P^{albumin}$

Since solute flux can be coupled to water flow (solvent drag), the apparent permeability P measured in the study would overestimate the true diffusive permeability P_d of intermediate-sized FITC-α-lactalbumin and FITC-ribonuclease as well as large molecule, FITC-albumin. Using the hydraulic conductivity L_p = 2.0 × 10^{-9} cm/s/cm H_2O for the frog pial microvessel, which was measured in Fraser *et al* (Fraser *et al.*, 1990) and L_p = 1.2 × 10^{-7} cm/s/cm H_2O for rat mesenteric microvessels, which was measured in Curry *et al*. (2003), we calculated the diffusive permeability P_d for FITC-α-lactalbumin, FITC-ribonuclease, and FITC-albumin by the following formula in (Curry and Frokjaer-Jensen, 1984; Fu *et al.*, 1998; Fu and Shen, 2003),

$$P_d = \frac{L_p(1-\sigma)\Delta p_{\text{eff}}}{lnP - ln\left[P - L_p(1-\sigma)\Delta p_{\text{eff}}\right]} \quad (1)$$

Here, P is the measured apparent permeability, L_p is the hydraulic conductivity of the microvessel, σ is the reflection coefficient of the microvessel to the solute, and Δp_{eff} is the effective filtration pressure across the microvessel wall.

$$\Delta p_{\text{eff}} = \Delta p - \sigma^{\text{albumin}}\,\Delta\pi^{\text{albumin}} - \sigma^{\text{FITC-solute}}\,\Delta\pi^{\text{FITC-solute}} \quad (2)$$

Superscript FITC-solute can be either FITC-α-lactalbumin, or FITC-ribonuclease, or FITC-albumin. Since there were no data reported for the reflection coefficients to all three test solutes of the rat pial microvessel, we estimated its reflection coefficients based on the data from rat mesenteric microvessels, which is 0.94 for albumin (Kendall and Michel, 1995) and 0.4 for α-lactalbumin (Michel and Curry, 1999),

respectively. Thus, $\sigma^{\alpha\text{-lactalbumin}}$ and $\sigma^{\text{ribonuclease}}$ were estimated to be 0.5 and σ^{albumin} to be 0.99 for pial microvessels (Yuan *et al.*, 2009b). In addition, Δp was ~10 cm H_2O in the pial microvessel (Yuan *et al.*, 2009b). $\Delta\pi^{\text{albumin}}$ was 3.6 cm H_2O for 10 mg/ml BSA. Using these values, the diffusive permeability of pial microvessels to FITC-α-lactalbumin ($P_d^{\alpha\text{-lactalbumin}}$) were calculated as 1.29 ± 0.22 (SD, n = 11) under control and 0.68 ± 0.17 (SD, n = 9) × 10^{-7} cm/s under orosomucoid treatment, which were 98.5% and 95.8% of their apparent permeability, respectively; the diffusive permeability to FITC-ribonuclease ($P_d^{ribonuclease}$) were calculated as 5.52 ± 1.77 (SD, n = 13) under control and 8.40 ± 1.58 (SD, n = 11) × 10^{-7} cm/s under orosomucoid treatment, which were 99.5% and 99.6% of their respective apparent permeability; the diffusive permeability to FITC-albumin ($P_d^{albumin}$) were calculated as 0.88 ± 0.21 (SD, n = 10) under control and 0.48 ± 0.11 (SD, n = 6)× 10^{-7} cm/s under orosomucoid treatment, which were 99.94% and 99.89% of their apparent permeability, respectively. For mesenteric microvessels, $\sigma^{\alpha\text{-lactalbumin}}$ and $\sigma^{\text{ribonuclease}}$ were estimated to be 0.4 and σ^{albumin} to be 0.94, while Δp_{eff} was calculated as ~5 cm H_2O (Fu and Shen, 2004). Using these values, $P_d^{\alpha\text{-lactalbumin}}$ of mesenteric microvessels were calculated as 21.4 ± 9.82 (SD, n = 7) under control and 9.21 ± 4.41 × 10^{-7} (SD, n = 7) cm/s under orosomucoid treatment, which were 93% and 85% of their apparent permeability, respectively; $P_d^{ribonuclease}$ were calculated as 43.0 ± 19.6 (SD, n = 7) under control and 56.5 ± 22.0 × 10^{-7} (SD, n = 7) cm/s under orosomucoid treatment, which were 97% of their respective apparent permeability; $P_d^{albumin}$ were calculated as 6.92 ± 1.98 (SD, n = 7) under control and 3.39 ± 1.34 (SD, n = 7) × 10^{-7} cm/s

under orosomucoid treatment, which were 98% and 96% of their apparent permeability, respectively.

Kimura *et al*. (Kimura *et al.*, 1993) measured L_p of arterioles in isolated rat brain cortex. Their median value for L_p was 5.9×10^{-9} cm/s/cm H_2O, which is almost 3 times of *in vivo* L_p value of 2.0×10^{-9} cm/s/cm H_2O for frog pial microvessels measured in (Fraser *et al.*, 1990). In general, frog microvessels have higher permeability than rat microvessels (Adamson *et al.*, 1988; Adamson *et al.*, 2004b). We used L_p of 2.0×10^{-9} cm/s/cm H_2O as our approximation for L_p of rat pial microvessel to calculate the convective contribution to the measured permeability. This frog L_p value would slightly overestimate the convective contribution to the permeability of rat pial microvessels.

Yuan *et al*. (Yuan *et al.*, 2009b) have reported the diffusive permeability of rat pial microvessels to neutral FITC-labeled dextrans under Ringer-BSA perfusion. The diffusive permeability to neutral FITC-dextran-10k and dextran-20k were 2.6×10^{-7} cm/s and 2.1×10^{-7} cm/s, respectively. From these measured data, it is reasonable to estimate the diffusive permeability to a neutral dextran having the same molecular weight as ribonuclease or α-lactalbumin (~14k), as 2.4×10^{-7} cm/s. This value is 1.9-fold of that to negatively charged α-lactalbumin and 43% of that to positively charged ribonuclease. In their study, they also measured the permeability to neutral FITC-dextran-70k with similar molecular weight of albumin (67k). The diffusive permeability to FITC-dextran-70k is 1.3×10^{-7} cm/s, which is 1.5-fold of that to negatively charged albumin.

Figure 3.3 demonstrates the comparison of the diffusive permeability of pial and mesenteric microvessels to the same solutes in the absence and presence of orosomucoid. The orosomucoid significantly changes the permeability to these charged molecules in both mesenteric and pial microvessels ($p < 0.03$). We can also see that under both control and orosomucoid treatment, the permeability of mesenteric microvessels to these three solutes is about one order of magnitude higher of that of pial microvessels, ranging from 7.8 to 17.4-fold under control and from 6.7 to 13.5-fold under orosomucoid treatment.

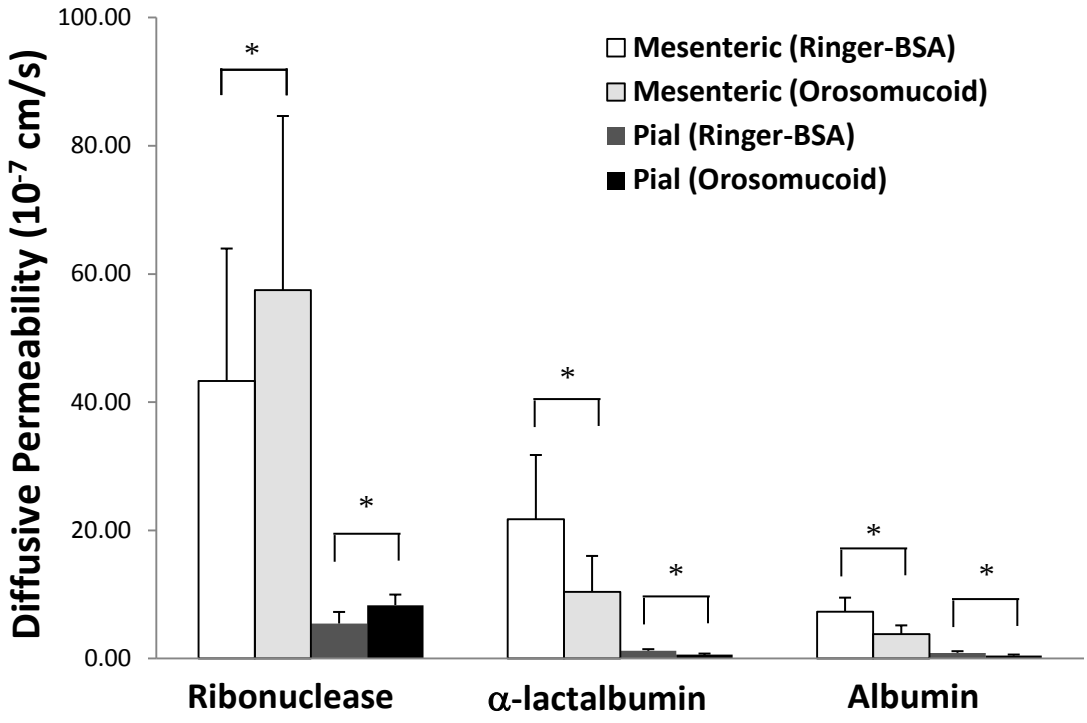

Figure 3.3 Comparisons of the diffusive permeability of pial and mesenteric microvessels to ribonuclease, α-lactalbumin, and BSA under normal Ringer-BSA

perfusion and orosomucoid treatment. The columns were plotted as mean ± SD. * $p < 0.05$

Modulation of solute permeability of mesenteric microvessels to charged solutes by orosomucoid: charge density of endothelial surface glycocalyx C_{mf}

Previous studies have demonstrated that the highly anionic glycoprotein, orosomucoid, plays an important role in determining the solute permeability of peripheral microvessels to charged hydrophilic solutes in both amphibians and mammals (Curry *et al.*, 1989; Haraldsson and Rippe, 1987; Haraldsson *et al.*, 1992). Curry *et al*. (Curry *et al.*, 1989) quantified the solute permeability of the frog mesenteric vessels to negatively charged α-lactalbumin and positively charged ribonuclease in the absence and presence of orosomucoid. In the present study, we quantified the diffusive permeability (P_d) of rat mesenteric microvessels to negatively charged α-lactalbumin and albumin, and to positively charged ribonuclease under the same conditions as in Curry *et al*. (Curry *et al.*, 1989). The ratio of $P_d^{\alpha\text{-}lactalbumin,orosomucoid}$ to $P_d^{\alpha\text{-}lactalbumin,BSA}$ for the paired measurement is 0.43, the ratio of $P_d^{ribonuclease,BSA}$ to $P_d^{\alpha\text{-}lactalbumin,BSA}$ is 2.0 and that of $P_d^{ribonuclease,orosomucoid}$ to $P_d^{\alpha\text{-}lactalbumin,orosomucoid}$ is 6.1. These values are comparable to those reported for frog mesenteric microvessels (Curry *et al.*, 1989). The higher permeability of positively charged ribonuclease than that of negatively charged α-lactalbumin indicates that the rat mesenteric microvessel carries negative charge under control conditions with the Ringer-BSA perfusate. In the presence of orosomucoid, $P^{ribonuclease}$ increases and $P^{\alpha\text{-}}$

^{lactalbumin} decreases from those in the absence of orosomucoid, suggesting that orosomucoid adds negative charge to the rat mesenteric microvessel wall.

On the basis of above observations, employing an electrodiffusion model for effects of endothelial surface glycocalyx on microvessel permeability (Fu *et al.*, 2003) and using the ultra-structural parameters measured by Adamson *et al*. (Adamson *et al.*, 2004b) and Squire *et al*. (Squire *et al.*, 2001) for the rat mesenteric microvessel wall, we predicted the effect of charge density of the surface glycocalyx C_{mf} on the permeability of the rat mesenteric microvessel to charged molecules. **Figure 3.4** demonstrates our model predictions for the ratio of $P_d^{\ ribonuclease}$ to $P_d^{\ \alpha\text{-}lactalbumin}$ as a function of $C_{mf.}$ To account for the measured $P_d^{\ ribonuclease,BSA}$ to $P_d^{\ \alpha\text{-}lactalbumin,BSA}$ of 2.0 (square in **Figure 3.4**), C_{mf} would be 30 mEq/L, while to account for the increased ratio of 6.1 in the presence of orosomucoid (triangle in **Figure 3.4**), C_{mf} would be 80 mEq/L, a 2.7-fold increase from the control. Our results suggest that the addition of orosomucoid alters the permeability of rat peripheral microvessels to charged molecules by increasing the fixed negative charge in the endothelial surface glycocalyx of the vessel wall.

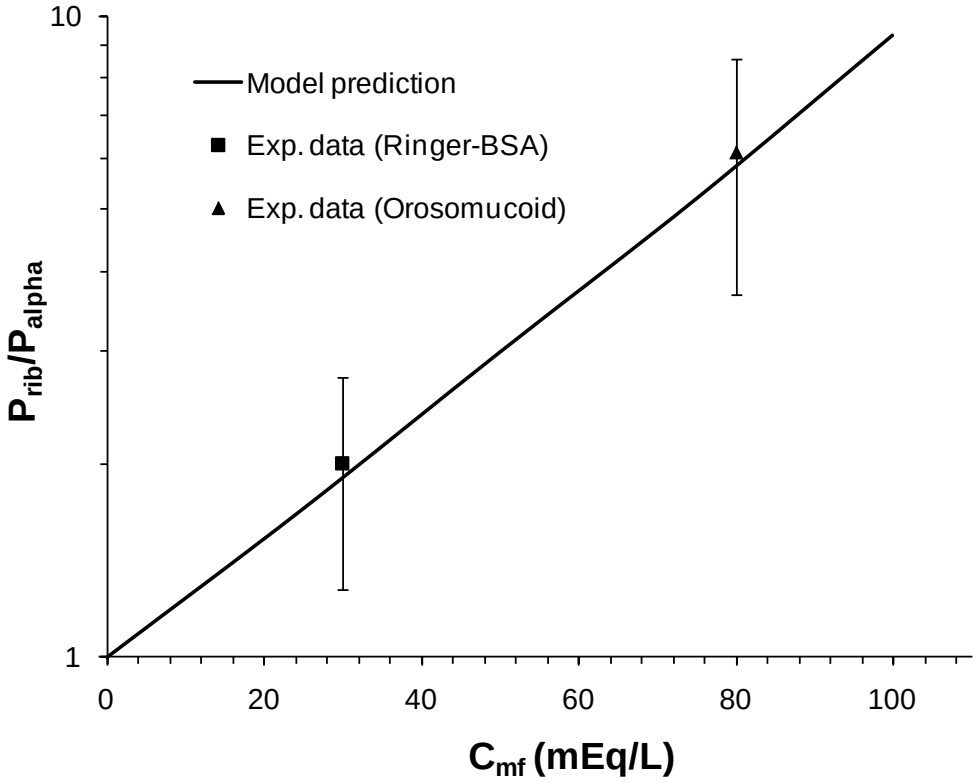

Figure 3.4 Ratio of permeability of positively charged ribonuclease to that of negatively charged α-lactalbumin (P_{rib}/P_{alpha}) as a function of charge density in the surface glycocalyx layer C_{mf} for rat mesenteric microvessels. The solid line is the model prediction while the square and triangle symbols (values plotted as mean ± SD) represent experimental data for P_{rib}/P_{alpha} under control (Ringer-BSA) and that under 0.1 mg/ml orosomucoid in Ringer-BSA, respectively.

Modulation of solute permeability of the BBB to charged solutes by orosomucoid: charge density of endothelial surface glycocalyx C_{mf} and that of basement membrane C_{mb}

To find out the effect of orosomucoid on the permeability of the BBB to charged solutes, we quantified the diffusive permeability (P_d) of rat pial microvessels to negatively charged α-lactalbumin and albumin, and to positively charged ribonuclease in the presence and absence of orosomucoid. The ratio of $P_d^{\ ribonuclease,BSA}$ to $P_d^{\ \alpha\text{-}lactalbumin,BSA}$ is 4.3, and that of $P_d^{\ ribonuclease,orosomucoid}$ to $P_d^{\ \alpha\text{-}lactalbumin,orosomucoid}$ is 12.4. In addition, to investigate whether this modulation of the permeability to these two test solutes is resulting from modification of other properties of the transport pathway rather than altering charge density of the SGL and the BM by orosomucoid, we also measured the permeability of pial microvessel to two neutral FITC-labeled dextrans, FITC-dextran-10k (FD10 s, Sigma; mol. wt. 10,000, Stokes radius ~1.9 nm) and FITC-dextran-40k (FD40 s, Sigma; mol. wt. 40,000, Stokes radius ~3.0 nm), under the treatment of orosomucoid, and the results were summarized in **Figure 3.5**. The mean value of the permeability to FITC-dextran-10k in presence of orosomucoid was 3.19 ± 1.47 (SD, n = 7) × 10^{-7} cm/s, and it is no significantly different from that in absence of orosomucoid (p = 0.97), which was 3.08 ± 1.30 (SD, n = 7) × 10^{-7} cm/s (Yuan *et al.*, 2009b). Additionally, the mean value of the permeability to FITC-dextran-40k in presence of orosomucoid was 1.87 ± 0.98 (SD, n = 9) × 10^{-7} cm/s, and it is also no significantly different from that in absence of orosomucoid (p = 0.84), which was 1.80 ± 0.91 (SD, n = 7) × 10^{-7} cm/s

(Yuan *et al.*, 2009b). From the results above, it appeared that orosomucoid did not alter the permeability to neutral solutes as orosomucoid did for the permeability to charge solutes, which may indicate that orosomucoid most likely to change solely the charge density along the transport pathway.

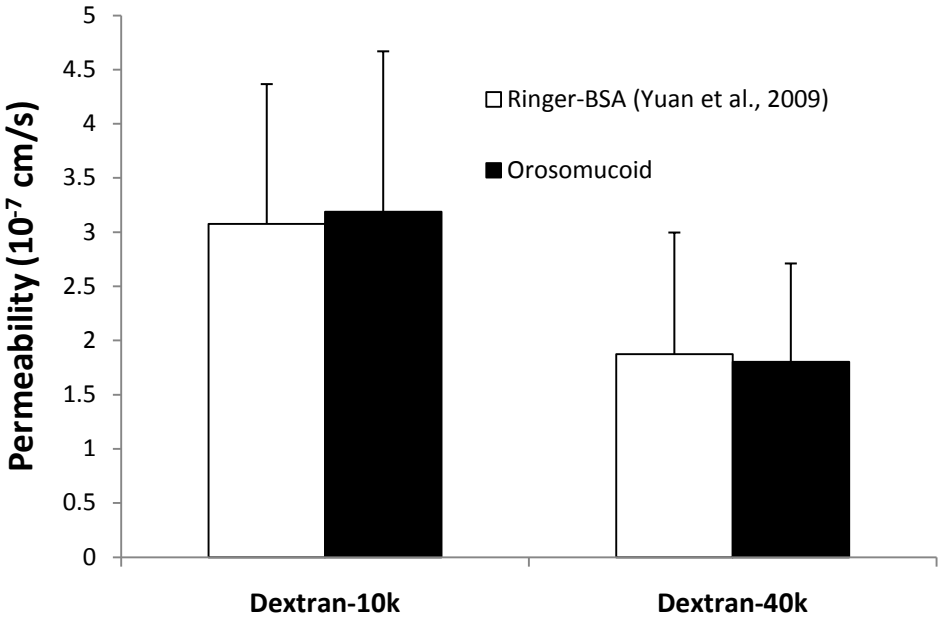

Figure 3.5 Comparison of solute permeability of pial microvessels by addition of 0.1 mg/ml orosomucoid with the BSA group (Yuan *et al.*, 2009b) for two neutral FITC-label dextrans, Dextran-10k with molecular weight of 10,000 and Dextran-40k with molecular weight of 40,000. Values were mean ± SD.

Based on the above measured permeability data of rat pial microvessels, we predicted the charge density C_{mf} in the endothelial surface glycocalyx and the charge density C_{mb} in the basement membrane of the BBB by using our newly developed transport model across the BBB (Fu *et al.*, 2008) and the anatomical parameters of the

rat cerebral microvessel reported in (Allt and Lawrenson, 1997a; Cassella *et al.*, 1997; Farkas and Luiten, 2001; Paulson and Newman, 1987; Schulze and Firth, 1992b). **Figure 3.6** demonstrates our model predictions for the ratio of $P_d^{\ ribonuclease}$ to $P_d^{\ \alpha\text{-}lactalbumin}$ as a function of C_{mb} under a fixed C_{mf} or when $C_{mf} = C_{mb}$. **Figure 3.6A** is the prediction for the control without orosomucoid and **Figure 3.6B** for that with orosomucoid. The dashed in **Figure 3.6A** is the prediction for a fixed C_{mf} = 30 mEq/L, which is the charge density predicted for the rat mesenteric microvessel under control condition, while the solid line in **Figure 3.6A** is the prediction when $C_{mf} = C_{mb}$. To account for the measured $P_d^{\ ribonuclease,BSA}$ to $P_d^{\ \alpha\text{-}lactalbumin,BSA}$ of 4.3 (square in **Figure 3.6A**), C_{mb} would be 30 mEq/L for both C_{mf} = 30 mEq/L and $C_{mf} = C_{mb}$ cases. **Figure 3.6B** is the prediction for the ratio of $P_d^{\ ribonuclease}$ to $P_d^{\ \alpha\text{-}lactalbumin}$ as a function of C_{mb} in the presence of orosomucoid. The dashed line in **Figure 3.6B** is the prediction for a fixed C_{mf} = 80 mEq/L, which is the charge density predicted for the rat mesenteric microvessel in the presence of orosomucoid, while the solid line in **Figure 3.6B** is the prediction when $C_{mf} = C_{mb}$. To account for the ratio of 12.4 in the presence of orosomucoid (triangle in **Figure 3.6B**), C_{mb} would be 55 mEq/L, a 1.8-fold increase from the control. The less increase in C_{mb} than that in C_{mf} might be due to less orosomucoid binding to the matrix in the basement membrane of the BBB, because the tight junction in between endothelial cells provides a large resistance to the transport of orosomucoid from the lumen to the basement membrane of the BBB.

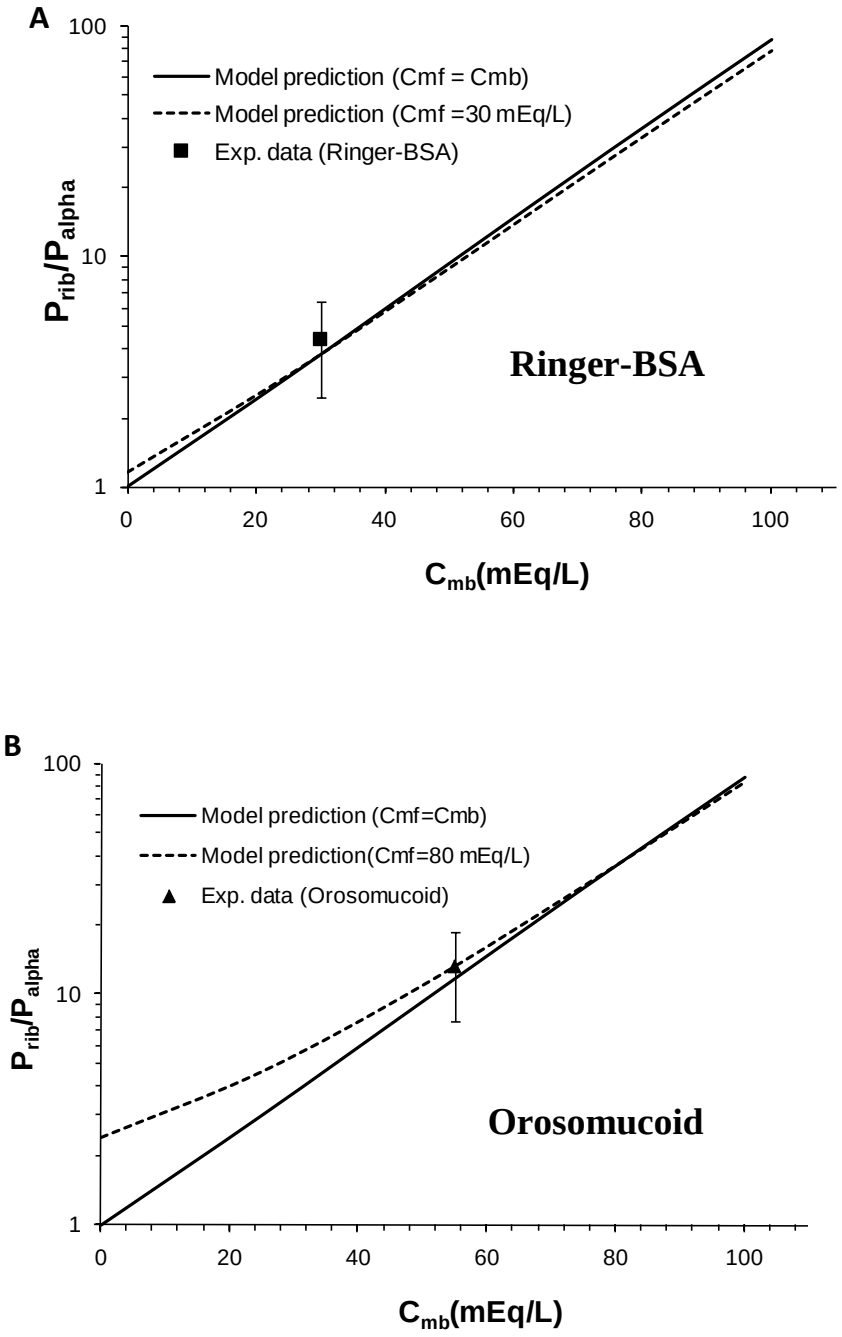

Figure 3.6 Ratio of permeability of positively charged ribonuclease to that of negatively charged α-lactalbumin (P_{rib}/P_{alpha}) as a function of charge density C_{mb} in the basement membrane for rat pial microvessels under the perfusate of **(A)** Ringer-

BSA and **(B)** 0.1 mg/ml orosomucoid in Ringer-BSA. The square and triangle symbols are experimental data for P_{rib}/P_{alpha} under control (Ringer-BSA) and that under 0.1mg/ml orosomucoid in Ringer-BSA, respectively. The lines are model predictions. The solid lines are the predictions when the charge density in the surface glycocalyx layer C_{mf} is the same as that in the basement membrane $C_{mb.}$ The dashed lines are the predictions for fixed C_{mf} : C_{mf} = 30 mEq/L in **(A)** and C_{mf} = 80 mEq/L in **(B)**.

In summary, we have measured the permeability of the rat pial cerebral microvessel to charged solutes in the absence and presence of orosomucoid. Combining the measured permeability data with a newly developed theoretical model for the solute transport across the BBB, we predicted the charge density in the endothelial surface glycocalyx and that in the basement membrane of the BBB in the absence and presence of orosomucoid. Our results suggest that there is charge in the matrix components of the BBB and orosomucoid modulates the permeability of the BBB to charged solutes by adding the negative charge to both the surface glycocalyx and the basement membrane of the BBB. These findings will help better understand the structural and electrochemical mechanisms of selectivity of the BBB and therefore provide a new method for controlling transport rates of charged molecules in drug delivery across the BBB.

CHAPTER 4 SURFACE CHARGE OF IMMORTALIZED MOUSE CEREBRAL ENDOTHELIAL CELL MONOLAYER ON TRANSPORT OF CHARGED SOLUTES

Introduction

To protect brain from blood-born neural toxins, the blood-brain barrier (BBB) between the central nervous system and the cerebral circulation maintains very low permeability due to its unique structure. In addition to endothelial cells with tight junctions, the BBB has complete wrapping of a very thin basement membrane and astrocytic end-feet (Hawkins and Davis, 2005). Various *in vivo* and *in vitro* models have been used for the study of the solute transport across the BBB. Except their comparatively high permeability and the loss of some expression of BBB efflux protein systems (Nicolazzo *et al.*, 2006), *in vitro* models have several advantages over *in vivo* models, including low cost, high-throughput screening, and easiness to assess compounds and to investigate the transport mechanism at molecular levels. Over decades, many *in vitro* models have been derived from primary brain capillary endothelial cell cultures, which have the closest resemblance to BBB phenotype *in vivo* (Nicolazzo *et al.*, 2006), and exhibit excellent characteristics of the BBB at early passages. However, primary cell cultures have their inherent disadvantages. For instance, they are usually extremely time consuming and require high skilled researchers. In addition, primary cell cultures lose their differential phenotype over repeated passages (Nicolazzo *et al.*, 2006; Omidi *et al.*, 2003). Moreover, primary cell

cultures have potential contaminations from other types of brain cells such as pericytes and astrocytes, which induce leaky barriers in the *in vitro* monolayer models (Brown *et al.*, 2007). Recently, the *in vitro* monolayer deriving from immortalized mouse brain endothelial cell line, bEnd3, becomes popular because of its advantages over primary cell culture, including the ability to maintain BBB characteristics over many passages, as well as easy growth and low cost. Previous studies have evaluated bEnd3 cells as an *in vitro* BBB model in terms of expression of tight junction proteins, the permeability to sucrose, the trans-endothelial electrical resistance (TEER) as well as transporter of glucose (Brown *et al.*, 2007; Omidi *et al.*, 2003) . They concluded that bEnd3 monolayer is an attractive *in vitro* BBB model, which can express mRNA for a number of important tight junction proteins, ZO-1, ZO-2, claudin-1, and claudin-3 and exhibit similar barrier functions as primary culture cells. In the present study, we investigated whether or not the bEnd3 monolayer is a good *in vitro* model for studying solute and nanoparticle transport across the BBB, especially the transport of charged molecules.

The surface glycocalyx layer (SGL) of the BBB is located on the luminal surface of the endothelium (Ueno *et al.*, 2004a) and contains a great number of solid-bound fixed negative charge (Tarbell and Pahakis, 2006). In addition to the tight junctions in between endothelial cells, the SGL plays an important role in maintaining the barrier function of endothelium due to its matrix-like structure as well as the charge (Adamson and Clough, 1992; Bruegger *et al.*, 2005; Cabrales *et al.*, 2007; Fu *et al.*, 2003; Squire *et al.*, 2001; Ueno *et al.*, 2004c). Yuan *et al.* (Yuan *et al.*, 2009b)

found that the permeability of intact rat pial microvessels to positively charged ribonuclease was four times as large as that to negatively charged α-lactalbumin, though they have almost the same size. Combining these measured permeability data with a mathematical model, they predicted that the charge density is ~30 mEq/L in the structural components of the BBB, i.e., the SGL and the basement membrane. Therefore, the first objective of the present study is to test whether bEnd3 monolayer expresses the functional SGL as in the intact BBB by quantifying the thickness ($\boldsymbol{L_f}$) and charge density ($\boldsymbol{C_{mf}}$) of the cultured bEnd3 monolayer (**Figure 4.1**)**.** To do this, we measured the solute permeability of bEnd3 monolayer to fluorescently-labeled neutral solutes (sodium fluorescein and various sized dextrans) and charged solutes (α-lactablumin and ribonuclease). By combining a transport model across the bEnd3 monolayer with the measured permeability data, we can predict $\boldsymbol{L_f}$ and $\boldsymbol{C_{mf}}$ of the SGL at the bEnd3 monolayer.

Orosomucoid, a plasma glycoprotein, which is synthesized in the liver and may be also secreted by endothelial cells (Sorensson *et al.*, 1999), increases several folds during infection or trauma (Matsumoto *et al.*, 2007; Sann *et al.*, 1984). Orosomucoid is also bound to the surface of cultured bovine pulmonary microvascular endothelial cells (Schnitzer and Pinney, 1992). It has been found that orosomucoid modulates the transport of charged solutes across the wall of peripheral and cerebral microvessels *in vivo* by decreasing the transport of negatively charged molecules but increasing that of positively charged ones (Curry et al., 1989; Haraldsson and Rippe, 1987); Yuan *et al.*, 2009b), suggesting that orosomucoid plays an essential role in maintaining the permeability property of endothelium by

adding negative charge to the SGL (Curry *et al.*, 1989; Haraldsson and Rippe, 1987; Sorensson *et al.*, 1999). The second objective of the present study is thus to investigate whether orosomucoid modulates the bEnd3 monolayer permeability in a similar way as it does for the intact endothelium of the BBB.

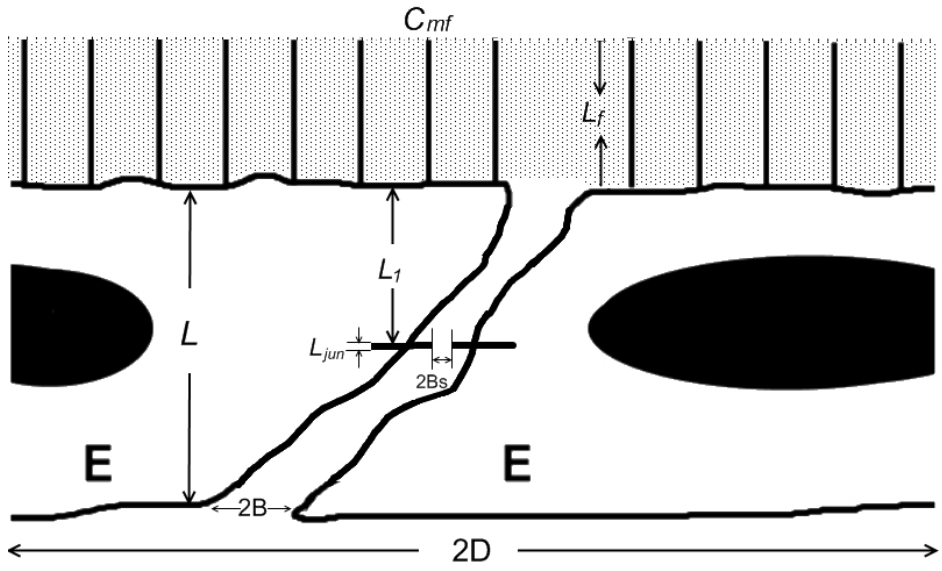

Figure 4.1 The schematic diagram of the b.End3 monolayer. There is a cleft (width 2B) with a tight junction (TJ, opening width $2B_s$) in between adjacent endothelial cells (E) . At the luminal side of the endothelium, there is a surface glycocalyx layer with a thickness L_f and a charge density C_{mf}.

The third objective is to test whether or not bEnd3 cell monolayer is a good *in vitro* model for studying the transport of nanoparticle drug carriers across the BBB. In the past decade, the charge-loaded polymeric nanoparticles have attracted increasing interests as the carriers for therapeutic agents across the BBB due to their prolonged bioavailability, high loading efficiency, and tunable surface chemistry (Moghimi *et*

al., 2001). Gil *et al*. (Gil *et al.*, 2009) developed novel quaternary ammonium β-cyclodextrin (QAβCD) nanoparticles as drug delivery carriers across the BBB. The QAβCD nanoparticles exhibit cationic property, which has been considered as an effective approach to enhance the transport across the BBB (Kreuter, 2004). The hydrodynamic radii of QAβCD nanoparticles are from 77 to 88 nm in pH 7.4 and 37 °C (Gil *et al.*, 2009), which are significantly larger than the size of paracellular pathways of the BBB. Surprisingly, Gil *et al.* (Gil *et al.*, 2009) found that the permeability of the bovine brain microvessel endothelial cell (BBMEC) monolayer to QAβCD nanoparticles was either comparable or even larger than that to neutral dextran-4k, whose molecular weight is similar to that of one basic unit of QAβCD nanoparticles (~5,000). One explanation was that when the large QAβCD nanoparticle crosses the BBMEC monolayer, it degrades to its much smaller basic units. Another more likely explanation was that the transport of the nanoparticles is by transcytosis, a trans-cellular process, instead of through a paracellular pathway. To examine whether or not bEnd3 monolayer is able to mimic the transport of nanoparticles across the endothelium of the intact BBB, we measured the bEnd3 monolayer permeability to these QAβCD nanoparticles, and compared with that of intact rat pial microvessels.

Materials and Methods

Cell culture

Immortalized mouse cerebral endothelial cells, bEnd3 cells (American Type Culture Collection, Manassas, VA) were grown in DMEM with 4.5 g/L glucose, 10% FBS, 3.7 g/L sodium bicarbonate, and 4 mM glutamine. Cells were maintained in a humidified cell culture incubator at 37°C and with 5% CO_2/95% room air. Cells used in all experiments were in passage 28-35. Cells were seeded at a density of 6.0×10^4 cells/cm^2 on Transwell permeable inserts (12mm in diameter, 0.4 μm pores size; Corning Incorporated, Corning, NY). Inserts were incubated at 37°C with 200 μl of 30 μg/ml fibronectin for one hour before plating cells. The cells seeded onto Transwell insert reached confluence within approximately two days, shown in **Figure 4.2**, in which the tight junction accessory proteins ZO-1 were stained with anti-ZO-1 antibody in green and the nuclei of endothelial cells were stained with propidium iodide in red. The permeability experiments were performed on the monolayer 4-5 days after cell seeding, allowing sufficient time for the cells to develop the junctions between cells.

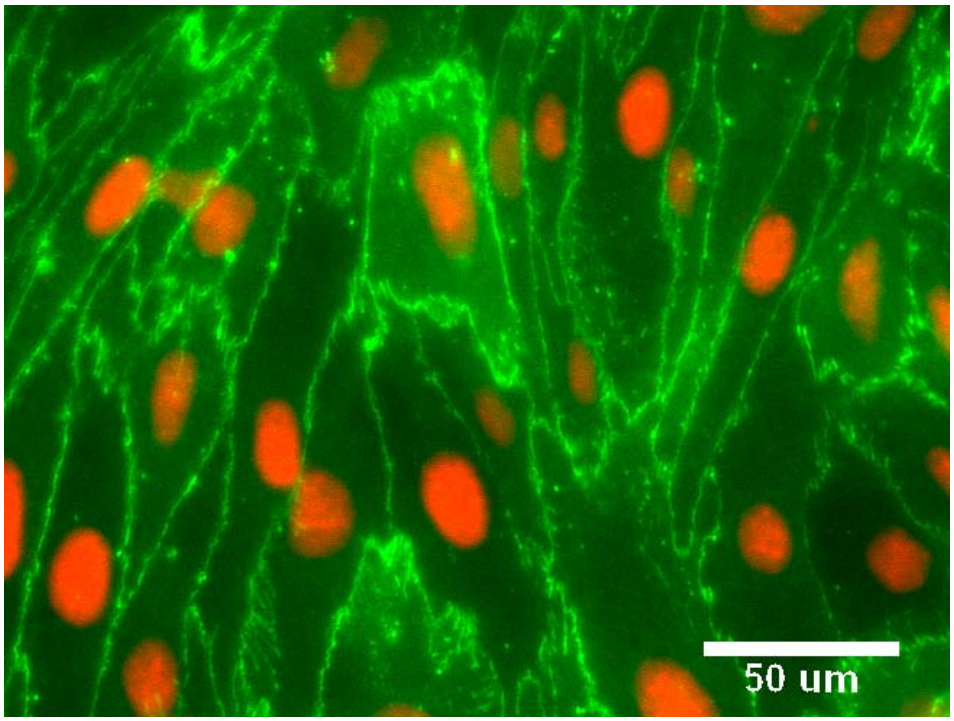

Figure 4.2 Tight junction accessory proteins ZO-1, stained with anti-ZO-1 antibodies in green, and the nucleus of endothelial cells, stained with propidium iodide in red, in bEnd3 cells grown on Transwell™ insert were observed using a fluorescence microscope.

In vitro solute permeability measurement

On the day of experiment, Transwell insert filter was washed with PBS, and then the media of the donor chamber was filled with 0.5 ml fluorescently-labeled test solutes in Ringer solution containing 10 mg/ml BSA while the acceptor chamber was filled with 1.5 ml Ringer solution containing 10 mg/ml BSA (**Figure 4.3**). The samples of 50 µL were drawn every 10 minutes for 90 minutes from the acceptor

chamber and were then replaced with the same amount of Ringer-BSA solution. The fluorescence tracer concentration in the samples was determined by Bio-Tek Synergy HT plate reader (Winooski, VT), and the excitation and emission wavelengths were set to 485 nm and 535 nm, respectively, for all fluorescence tracers in the present study. The solute permeability (P) of the monolayer was calculated from the relationship,

$$P = \frac{(\frac{\Delta C_A}{\Delta t}) \times V_A}{C_D \times S}$$

Where $\frac{\Delta C_A}{\Delta t}$ is the increase in fluorescence concentration in the accepter chamber during the time interval Δt, C_D is fluorescence concentration in the donor chamber (assumed to be constant during the experiment), V_A is the volume of the acceptor chamber, and S is the surface area of the filter.

The measured solute permeability was made on the bEnd3 monolayer that was formed on Transwell insert with 0.4 μm pores. Transwell insert itself could also provide resistance on transport of solutes. Therefore, the total resistance of this *in vitro* model system comprises of two parts: the resistance from the monolayer and the resistance from the empty insert. Thus, the permeability of the monolayer alone could be calculated from the relationship,

$$\frac{1}{P_t} = \frac{1}{P_c} + \frac{1}{P_i}$$

Solving above equation, we have the permeability of the monolayer, $P_c = \frac{P_t}{1-\frac{P_t}{P_i}}$.

Here P_t is the measured permeability of the total system and P_i is the permeability of the insert.

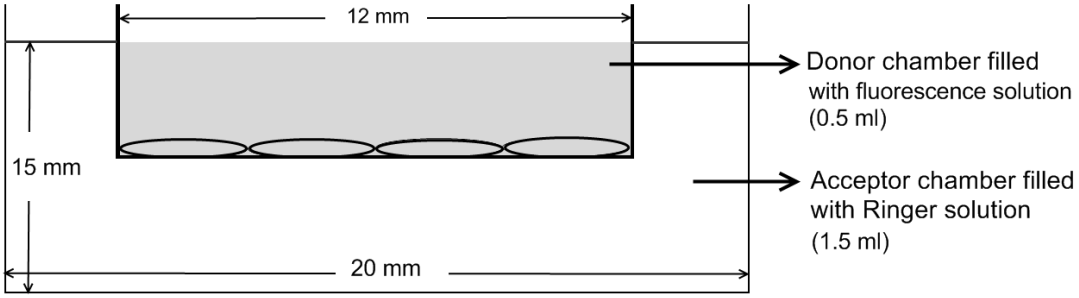

Figure 4.3 Transwell filter set-up for measuring cell monolayer permeability to solutes. The acceptor chamber was filled with 10 mg/ml BSA in Ringer solution or with additional orsomucoid, while the donor chamber was filled with the same solution additionally added with fluorescence tracers. The sample solution was extracted from the acceptor chamber every 10 minutes for fluorescence assessment.

Solutions and fluorescent test solute preparation

Mammalian Ringer solution

Mammalian Ringer solution with 10mg/ml bovine serum albumin (BSA, A4378, Sigma) was used during the permeability measurement (Fu and Shen, 2004). Composites of the Ringer solution were described in Chapter 2 and 3.

Neutral test solutes: sodium fluorescein and FITC-dextrans

Sodium fluorescein (F6377, Sigma; mol. wt. 376, Stokes–Einstein radius ~ 0.45 nm) and all FITC-dextrans, FITC-dextran-4k (FD4, Sigma; mol. wt. 4000, Stokes radius ~ 1.4 nm), FITC-dextran-20k (FD20 s, Sigma; mol. wt. 20,000, Stokes radius ~ 2.4 nm), and FITC-dextran-70k (FD70 s, Sigma; mol. wt. 70,000, Stokes radius ~ 3.6 nm), were dissolved in Ringer solution containing 10 mg/ml BSA at the concentration of 10 μM.

Charged test solutes: FITC labeled BSA, ribonuclease and α-lactalbumin

The FITC-labeling of ribonuclease and α-lactalbumin was described in details in Chapter 3, and FITC-labeled BSA (A9771, Sigma) was directly purchased from Sigma.

Analysis and statistics

All data were presented as means ± SD. Data were analyzed for statistical significance using ANOVA. Significance was assumed for probability levels $p < 5\%$.

Results and Discussion

It has been demonstrated that bEnd3 monolayer is able to mimic permeability properties of primary culture models of early passages (Brown *et al*., 2007; Omidi *et al*., 2003). However, they also suggested that the permeability of bEnd3 monolayer to sucrose increased significantly after passage 35, compared with that of prior

passages. In the present study, we measured solute permeability of bEnd3 monolayer of the cells at passages from 28 to 35, 2-3 days after the formation of confluence. The extra time after confluence is crucial for the formation of the tight junctions between endothelial cells (Brown *et al*., 2007).

Solute permeability of bEnd3 monolayer to neutral solutes

Table 4.1 summarized the measured permeability (*P*) of the monolayer to sodium fluorescein and various sized neutral dextrans in Ringer-BSA solution. The solute permeability was also corrected by subtracting the resistance contributed by empty Transwell insert using the equation shown in the previous section. After correction, the permeability to sodium fluorescein (P^{NaF}) was 7.24 ± 0.84 × 10^{-6} cm/s, ranging from 5.40 to 8.35 × 10^{-6} cm/s, while P^{Dex4k} was 2.91 ± 0.43× 10^{-6} cm/s, ranging from 2.48 to 4.01 × 10^{-6} cm/s, P^{Dex20k} was 0.80 ± 0.16 × 10^{-6} cm/s, ranging from 0.59 to 1.04 × 10^{-6} cm/s, and P^{Dex70k} was 0.44 ± 0.16 × 10^{-6} cm/s, ranging from 0.26 to 0.96 × 10^{-6} cm/s. These values are comparable to those measured in previous studies of bEnd3 monolayer and other *in vitro* BBB models using primary cells for similar size solutes (Brown *et al*., 2003; Brown *et al*., 2007; Grabb and Gilbert, 1995; Omidi *et al*., 2003).

Table 4.1 Measured and corrected permeability (P) of b.End3 monolayer to neutral solutes

Solutes	MW	Stokes radius (nm)	*P* (x 10^{-6} cm/s), measured (± SD, n = 6)	*P* (x 10^{-6} cm/s), corrected (± SD, n = 6)
NaF	376	0.45	5.70 (± 0.66)	7.24 (± 0.84)
Dex4k	4000	1.4	2.38 (± 0.35)	2.91 (±0.43)
Dex20k	20000	2.4	0.77 (± 0.15)	0.80 (±0.16)
Dex70k	70000	3.6	0.42 (± 0.15)	0.44 (±0.16)

Solute permeability of bEnd3 monolayer to charged solutes in the presence and absence of orosomucoid

We measured permeability of bEnd3 monolayer to FITC-labeled α-lactalbumin (MW 14,176; Stokes radius 2.01 nm; net charge -11) and ribonuclease (MW 13,683; Stokes radius 2.0 nm; net charge +3) in Ringer-BSA solution (control), and in that with additional 1 mg/ml orosomucoid (G3643, α_1-acid glycoprotein, Sigma). **Table 4.2** summarizes the measured and the corrected permeability to α-lactalbumin and ribonuclease for both control and orosomucoid groups. After correction for the resistance from the Transwell insert, the permeability of the bEnd3 monolayer to ribonuclease in Ringer-BSA ($P^{ribonuclease,\ BSA}$) was 2.21 ± 0.63 × 10^{-6} cm/s, ranging from 1.63 to 3.43 × 10^{-6} cm/s, while the permeability to ribonuclease in the presence of orosomucoid ($P^{ribonuclease,\ ORO}$) was 3.95 ± 0.72 × 10^{-6} cm/s, ranging from 2.48 to 4.91 × 10^{-6} cm/s; Similarly, $P^{\alpha\text{-}lactalbumin,\ BSA}$ was 1.09 ± 0.64 × 10^{-6} cm/s, ranging from 0.33 to 2.50 × 10^{-6} cm/s, while $P^{\alpha\text{-}lactalbumin,\ ORO}$ was 0.76 ± 0.27 × 10^{-6}

cm/s, ranging from 0.42 to 1.14 × 10^{-6} cm/s. Correspondingly, the ratio of permeability of the monolayer to positively charged ribonuclease to that to negatively charge α-lactalbumin was 2.03 in the absence of orosomucoid, while this ratio increased to 5.20 in the presence of orosomucoid.

Table 4.2 Measured and corrected P of b.End3 monolayer to charged solutes.

Solutes	MW	Stokes radius (nm)	Solution in Transwell	*P* (10^{-6} cm/s), measured (± SE)	*P* (10^{-6} cm/s), corrected (± SE)
Ribonuclease	13,683	2.0	**BSA**	1.97 (± 0.56), n = 6	2.21 (± 0.63), n =6
			Orosomucoid	3.24 (± 0.59), n = 9	3.95 (± 0.72), n = 9
α-lactalbumin	14,176	2.01	**BSA**	1.03 (± 0.60), n = 9	1.09 (± 0.64), n = 9
			Orosomucoid	0.73 (± 0.26), n = 9	0.76 (± 0.27), n = 9
BSA	69,000	3.5	**BSA**	0.39 (± 0.03), n = 8	0.40 (± 0.03), n = 8
			Orosomucoid	0.28 (± 0.04), n = 9	0.28 (± 0.04), n = 9

Comparison of permeability of bEnd3 monolayer and that of pial microvessels to neutral solutes

Figure 4.4 compares the permeability of bEnd3 monolayer to various sized neutral solutes, NaF, dextran-4k, dextran-20k, and dextran-70k (diamonds), with that of intact rat pial microvessels to the same solutes (squares) (Yuan *et al*., 2009a). The ratios of permeability of bEnd 3 (P_{bEnd3}) to that of pial microvessels (P_{pia}) are 3.0, 3.6, 3.8 and 3.4-fold correspondingly, to NaF, dextran-4k, dextran-20k, and dextran-70k. This range of P_{bEnd3} to P_{pia} is much smaller than that of $P_{mesentery}$ (measured in intact rat mesenteric microvessels) to P_{pia}, which is from 6 to 11-fold for the similar

sized solutes (Fu and Shen, 2004; Yuan *et al.*, 2009a). Our results indicate that the bEnd3 monolayer carries the low solute permeability character of the BBB and thus can be a good *in vitro* model for studying transport across the BBB.

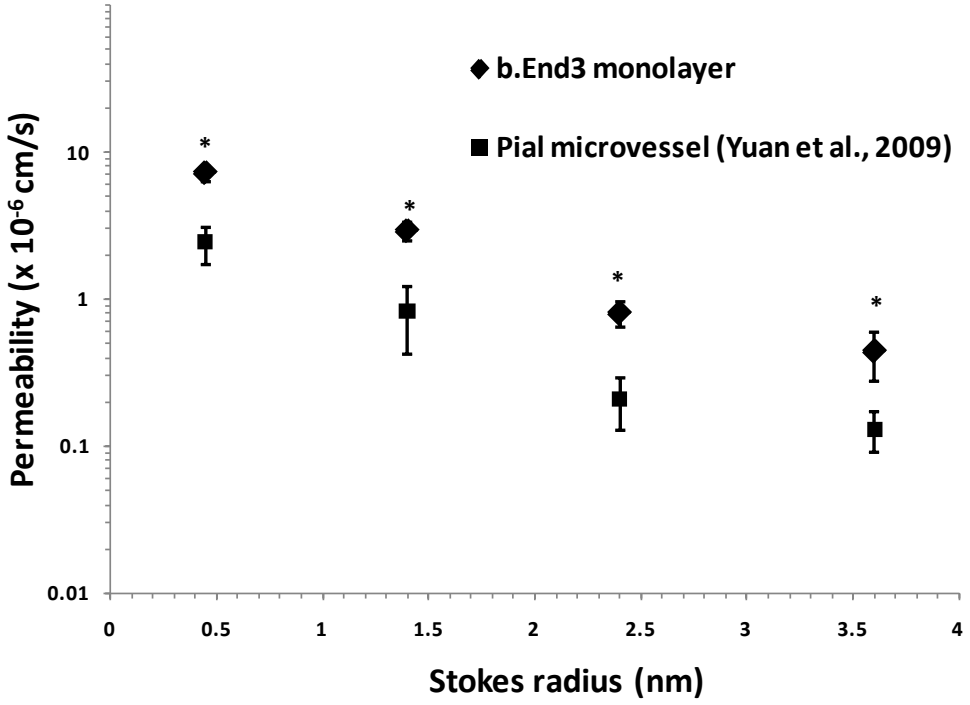

Figure 4.4 Comparison of the permeability of b.End3 monolayer (♦) to that of intact rat pial microvessel (■) to sodium fluorescein, dextran-4k, dextran-20k, and dextran-70k. Values were plotted as Mean ± SD. * $p < 0.001$.

Determination of surface glycocalyx layer (SGL) thickness L_f of bEnd3 monolayer

In order to predict the thickness of the SGL (L_f) of bEnd3 monolayer, we have measured the solute permeability of the monolayer to four neutral solutes with characteristic sizes: sodium fluorescein (Stokes radius = 0.45 nm), dextran-4k (Stokes

radius = 1.4 nm), dextran-20k (Stokes radius = 2.3 nm), and dextran-70k (radius = 3.5 nm). We also used a modified theoretical model from Fu *et al.* (Fu *et al.* 2003) to predict the L_f using the anatomical parameters of bEnd3 monolayer, either measured in the current study or from the literature. **Table 4.3** summarizes the values for these parameters. The model geometry is shown in **Fig. 4.1**. The lines in **Fig. 4.5** show the model predictions of the permeability to these four solutes as a function of L_f, while the filled circles represent the experimental results. From **Fig. 4.5** , we can see that for the best fit to the measured *P* to NaF, the thickness of the SGL, L_f, should be 215 nm, ranging from 195 to 260 nm when considering the deviation in the measured data; for Dextran-4k, L_f should be 140 nm, ranging from 110 to 160 nm; for Dextran-20k, L_f should be 200 nm, ranging from 150 to 260 nm; for Dextran-70k, L_f should be 100 nm, ranging from 85 to 180 nm. Overall, to account for the measured permeability data for all four solutes, L_f would be 163 ± 57 nm, which is comparable to those found in the peripheral and cerebral microvessels (Adamson and Clough, 1992; Allt and Lawrenson, 1997a).

Table 4.3 Anatomical parameters of bEnd3 monolayer in the model

Thickness of endothelial cells(Schulze and Firth, 1992a)	L	700nm
Distance between the junction strand and the front of the cleft(Fu and Chen, 2003; Schulze and Firth, 1992a)	L_1	350nm
Width of inter-endothelial cleft(Adamson *et al.*, 2004a)	2B	18nm
Width of the small slit of the junction strand(Allt and Lawrenson, 1997b; Cassella 1997)	$2B_s$	8nm
Thickness of tight junction strand(Adamson *et al.*, 2004a)	L_{jun}	11nm
Width of endothelial cells (measured in the present study)	2D	20μm
Total cleft length per unit endothelial monolayer surface area (measured in the present study)	L_{jt}	603cm/cm^2

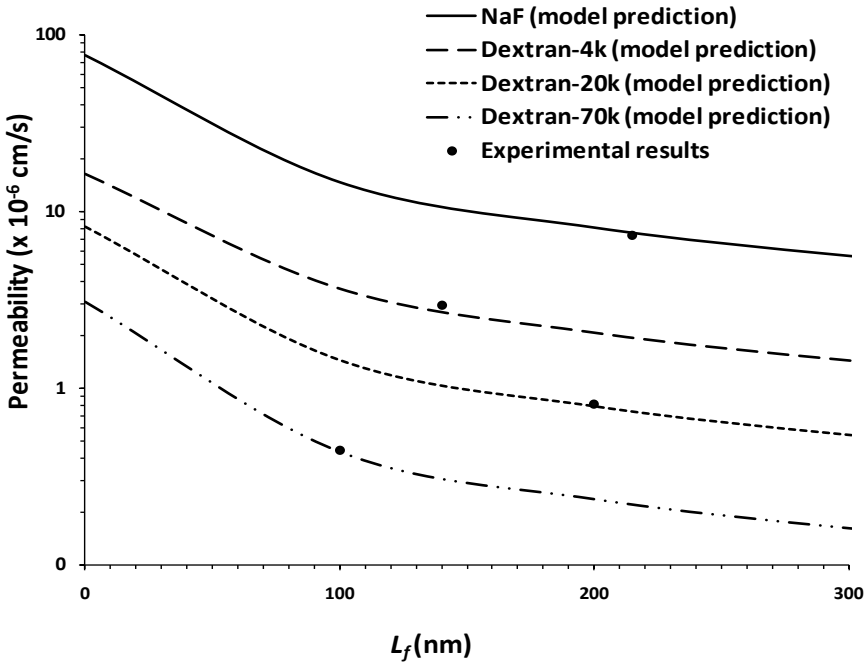

Figure 4.5 The permeability of b.End3 monolayer to four different sized solutes as a function of the thickness of SGL, L_f, of the monolayer. The lines represent model predictions, and experimental results (circles) were plotted as mean ± SD.

Comparison of permeability of bEnd3 monolayer and that of pial microvessels to charged solutes

Previously *in vivo* study has demonstrated that the charge carried by the SGL of the cerebral endothelium plays an important role in modulating the permeability of the BBB to charged solutes (Yuan *et al.*, 2009b). In the present study, we examined whether or not bEnd3 monolayer carries significant charge and has effect on the transport of charged solutes. If it does, how much is the charge density of the SGL of bEnd3 monolayer? Can the plasma glycoprotein, orosomucoid, modulate its permeability to charged solutes by adding the charge to the SGL, as it has been observed in the endothelium of the intact BBB (Yuan *et al.*, 2009b)? To answer these questions, we measured the permeability of bEnd3 monolayer to the solutes with similar size but opposite charges: negatively charged α-lactalbumin (-11) and positively charged ribonuclease (+3) in the presence and absence of orosomucoid. **Figure 4.6** shows our results. The ratio of $P^{ribonuclease}$ to $P^{\alpha\text{-}lactalbumin}$ was about 2.0 in the absence of orosomucoid, which was less than that, 4.4, found in intact pial microvessels (Yuan *et al*., 2009b). The difference is most likely due to the additional negative charge carried by the basement membrane sandwiched between the endothelium and the wrapping astrocytes of the intact BBB (del Zoppo and Hallenbeck, 2000; Hamann *et al*., 1995; Leblond and Inoue, 1989; Miosge, 2001). In the presence of orosomucoid, the ratio of $P^{ribonuclease}$ to $P^{\alpha\text{-}lactalbumin}$ was increased to 5.2, which is smaller than that measured in rat pial microvessels for the same reason as in the absence of orosomucoid.

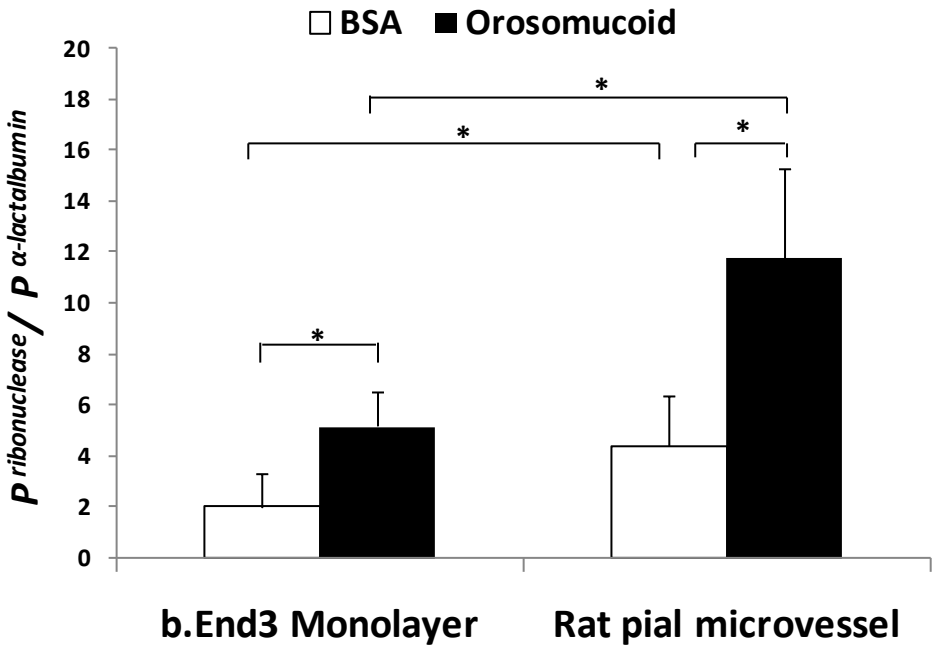

Figure 4.6 Comparison of the ratios of $P^{ribonuclease}/P^{\alpha\text{-}lactalbumin}$ of b.End3 monolayer to that of pial microvessels (Yuan *et al.*, 2009a) in 10 mg/ml BSA-Ringer solution (open columns) and in the solution added with 1 mg/ml orosomucoid (solid columns). The values were plotted as mean ± SD. * $p < 0.05$.

Determination of surface glycocalyx layer (SGL) charge density C_{mf} of bEnd3 monolayer

In order to estimate the charge density of the SGL, C_{mf}, of the bEnd3 monolayer, we combined the measured permeability of bEnd3 monolayer to negatively charged α-lactalbumin (-11) and positively charged ribonuclease (+3) in a control solution of 10 mg/ml BSA-Ringer, with predictions from an electro-diffusion

model modified from Fu *et al.* (Fu et al, 2003) using anatomical parameters of the bEnd3 monolayer (**Table 4.3**) and the SGL thickness $\boldsymbol{L_f}$ found from the previous section. The solid line in **Fig. 4.7** shows our model prediction for the ratio of the permeability of the bEnd3 monolayer to ribonuclease to that to α-lactalbumin as a function of the SGL charge density $\boldsymbol{C_{mf}}$. The squares represent the measured permeability in the presence and absence of orosomucoid. To account for the measured ratio of $P^{\,ribonuclease}$ to $P^{\,\alpha\text{-}lactalbumin}$ of 2.0 in the absence of orosomucoid, $\boldsymbol{C_{mf}}$ would be 24 mEq/L, which is comparable to that of the SGL, ~30 mEq/L, at the endothelium of the intact pial microvessel (Yuan *et al.*, 2009b).

Modulation of permeability of bEnd3monolayer to charged solutes by orosomucoid

Our recent study (Yuan *et al*. 2009b) demonstrated that the charge density of SGL of the intact pial microvessel increases from ~30 mEq/L in the absence of orosomucoid, to ~80 mEq/L in the presence of orosomucoid, by roughly 2.7-fold increase, in order to account for the increased ratio of $P^{\,ribonuclease}$ to $P^{\alpha\text{-}lactablumin}$ under the orosomucoid treatment. For this *in vitro* BBB model of bEnd3 monolayer, our model (the line in **Fig. 7**) predicted that the charge density of the SGL $\boldsymbol{C_{mf}}$ would increase from ~25 mEq/L in the absence of orosomucoid to ~50 mEq/L in the presence of orosomucoid, by approximately 2-fold increase, in order to account for the measured ratios, the open square for the control and the solid square for the orosomucoid treatment. Although this increase ratio is slightly less than that in the intact pial microvessel, the added charge by orosomucoid to the SGL of bEnd3 is significant and it substantially modulates the transport of charged solutes.

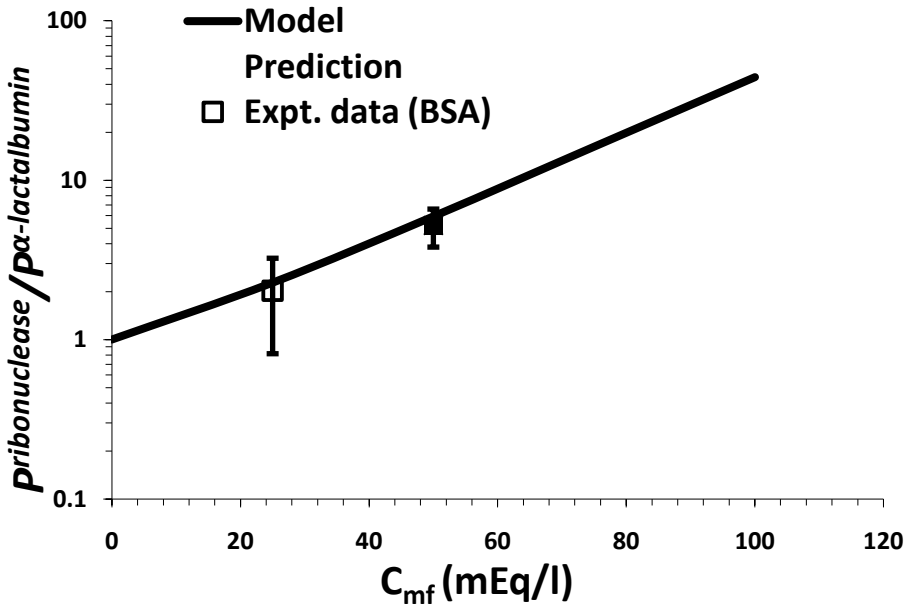

Figure 4.7 The ratio of $P^{ribonuclease}$ to $P^{\alpha\text{-}lactalbumin}$ as a function of charge density of SGL ($\mathbf{C_{mf}}$) of b.End3 monolayer. The solid line represents the model prediction. The open square represents the measured ratio in 10 mg/ml BSA-Ringer (BSA), while the solid square represents the measured ratio in 1mg/ml orosomucoid in BSA-Ringer (ORO). Experimental data were plotted as mean ± SD.

Comparison of permeability of bEnd3 monolayer and that of rat pial microvessels to QAβCD nanoparticles

We measured the permeability of both bEnd3 monolayer and rat pial microvessels to QAβCD nanoparticles, designed as carriers for drug delivery to the central nervous system, to examine whether bEnd3 monolayer is a good *in vitro* model for transport study of drug carriers. The permeability of bEnd3 monolayer and

that of rat pial microvessels to QA*β*CD nanoparticles are summarized in **Fig. 4.8**. Each QA*β*CD sample is denoted as 1-W-N, where W and N represent the feeding molar ratios of choline and epichlorohydrin to *β*-CD, respectively (Gil *et al.*, 2009). Sample 1-15-0.5 has a zeta potential of -11.8 $(\zeta)^c$/mV, while sample 1-15-4 and sample 1-15-6 have zeta potential of 6 and 14 $(\zeta)^c$/mV, respectively (Gil *et al.*, 2009). The hydrodynamic radii of these QAβCD nanoparticles were 77 to 88 nm in pH 7.4 and 37 °C (Gil *et al*., 2009). The permeability of bEnd3 monolayer to sample 1-15-0.5, 1-15-4, and 1-15-6 was 2.17 (± 0.66, SD, n = 6) × 10^{-6} cm/s, 3.60 (± 1.40, SD, n = 6) × 10^{-6} cm/s, and 3.27 (± 1.58, SD, n = 6) × 10^{-6} cm/s, respectively, while that of rat pial microvessels was 2.34 (± 0.70, SE, n = 9) × 10^{-6} cm/s, 2.71 (± 0.58, SD, n = 13) × 10^{-6} cm/s, and 2.83 (± 0.64, SD, n = 11) × 10^{-6} cm/s, correspondingly. The permeability of bEnd3 monolayer to each QAβCD nanoparticle shows no significantly difference from that of rat pial microvessels ($p > 0.05$). The permeability of bEnd3 monolayer to neutral Dextran-4k was 2.91 × 10^{-6} cm/s, which is slightly larger than that of the negatively charged 1-15-0.5, but smaller than that of positively charged 1-15-4, and 1-15-6. In contrast, the permeability of pial microvessels to neutral Dextran-4k was 0.92 × 10^{-6} cm/s (Yuan *et al.*, 2009a), which is roughly 1/3 of its permeability to these nanoparticles.

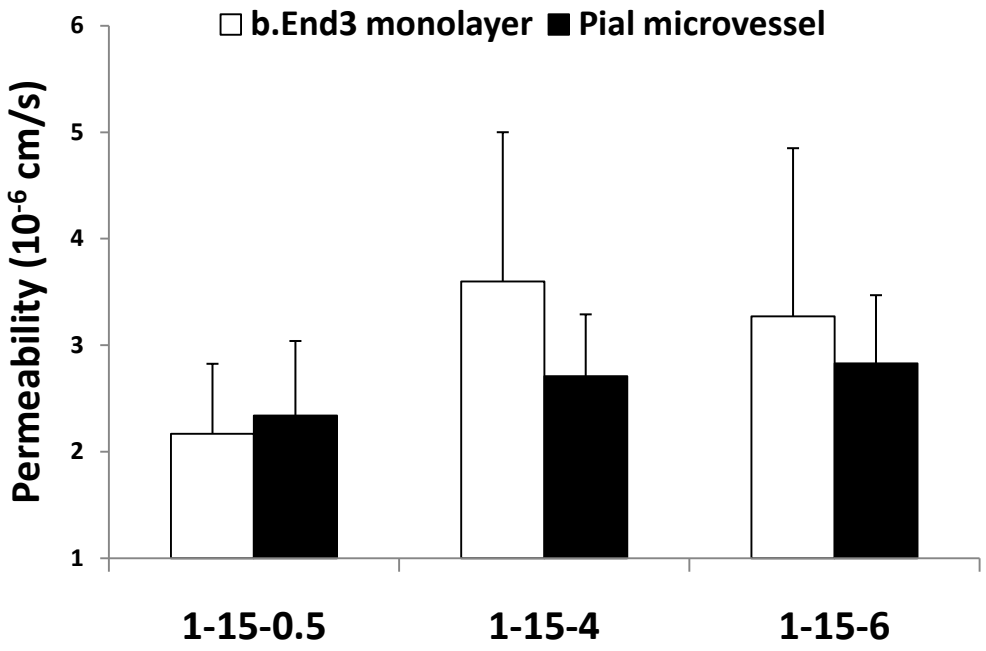

Figure 4.8 Comparison of the permeability of b.End3 monolayer and rat pial microvessel to three samples of QAβCD nanoparticles. The values were plotted as mean ± SD.

Because the endothelium of the BBB is wrapped by the basement membrane and astrocyte-foot processes, the resistance of the BBB would be larger for both paracellular and transcellular transport than that of the endothelium alone. That the permeability of the BBB to much smaller Dextran-4k is only 1/3 of that to the much larger nanoparticles suggests that instead of going through a paracellular pathway like Dextran-4k, these nanoparticles would go through a transcellular pathway across the BBB. In addition, there is no significant difference between the permeability of

bEnd3 monolayer and that of pial microvessels to the QAβCD nanoparticles. This implies that the trans-endothelial resistance is dominant in the nanoparticle transport across the BBB.

In summary, the cultured cell monolayer of the immortalized mouse brain cell line, bEnd3, is able to maintain many characteristics of the BBB: low (paracellular) permeability to various sized solutes, suggesting well-formed tight junctions; comparable thickness and the charge density of the SGL to that of the intact BBB endothelium; the charge of SGL can be modulated by orosomucoid in a similar way as in the intact BBB; demonstrating transcellular transport of large nanoparticles as observed in the intact BBB. Overall, the bEnd3 monolayer is a good *in vitro* model for studying the solute and particle transport across the BBB.

CHAPTER 5 SUMMARY AND FUTURE WORK

The blood-brain barrier is the most important factor limiting drug delivery into the central nervous system because of its unique structures, which on the other hand protect the brain from blood-borne neurotoxics. The first step to develop new drugs for the CNS disease may start from searching the chemicals or drug carriers that are capable of penetrating the barrier. In this study, we have developed an *in vivo* rat model to measure apparent permeability to various sized and various charged solutes as well as nanoparticles, which is essential for assessing the ability of those molecules to cross the BBB. This model involves minimum damage to the animal as well as microvessels, without opening the skull and without direct manipulation on microvessels, and is thus suitable for long term measurement (1-2 hours). Nevertheless, this model still needs improvement to avoid the potential damage of the BBB. For example, we introduced fluorescence solution into the cerebral circulation with mammalian Ringer solution and 1% BSA, which is used as blood substitute without oxygen. This may cause hypoxia in the brain, which is suggested to increase the permeability of the BBB (Kaur and Ling, 2008), although our results did not show significant increase in the permeability in one hour after perfusion with 1% BSA-Ringer. The oxygenazation of solution will prevent potential hypoxia at the local measurement region.

Later, we have applied this model, along with a newly developed theoretical model, to quantify the charge effects of the BBB and the effects of orosomucoid on

charged solute transport, which will help us to better understand the mechanism by which the BBB regulates the transport of charged solutes. Our results showed that not only the charge in the surface glycocalyx layer of the BBB but also the charge in the basement membrane of the BBB play an important role in determining the permeability of charged solutes. Moreover, our study shows that orosomucoid, the circulating plasma glycoprotein, is essential for maintaining the permeaselective property of the BBB by adding a negative charge to the SGL of the endothelium, which will decrease the BBB permeability to the negatively charged plasma proteins such as albumin.

Another interesting related study would be to examine effects of vascular endothelial growth factor (VEGF) and adenosine 3′, 5′-cyclic monophosphate (cAMP) on solute transport across the BBB, which could lead us to find new targets in curing CNS disorders as well as new ways in delivering therapeutic drugs into the brain. Vascular endothelial growth factors (VEGFs) are a family of cytokines that act as potent mediators of endothelial cell proliferation, migration, and angiogenesis (Connolly *et al.*, 1989; Dvorak *et al.*, 1995). In VEGF-dependent steps in early angiogenesis include vasodilatation (increased blood flow) and vascular leakage (increased vascular permeability) (Merrill and Oldfield, 2005), and increased expression of VEGF has been suggested as a factor disrupting blood-brain barrier integrity (Mayhan, 1999). Additionally, a large numbers of studies have demonstrated the presence of VEGF in many CNS disorders, such as brain tumor, hypoxia-induced vasogenic edema, stroke, etc. (Ding *et al.*, 2004; Kaur *et al.*, 2006; Uesaka *et al.*,

2007), which has led to speculation that VEGF is an important contributor to these CNS disorders and a potential therapeutic target. In addition, previous studies have found that increased intracellular levels of adenosine 3′, 5′-cyclic monophosphate (cAMP) can block the inflammatory response in many experimental models. cAMP is one of the few substances that improve endothelial barrier function. Elevation of endothelial cAMP effectively reduced the permeability of endothelial cells both *in vitro* and *in vivo*, and under both physiological and pathological conditions such as in ischemia-reperfusion injury, and after exposure to inflammatory agents, e.g., histamine, one of the few central nervous system neurotransmitters found to cause consistent blood-brain barrier opening (Abbott, 2000), thrombin, ATP, H_2O_2, etc. (Fu *et al.*, 2006). Our objective is to understand how the BBB responses to these factors like VEGF and cAMP and how the permeability of the BBB is modulated by these factors. Understanding this will help us in designing better strategies for drug delivery into the brain.

Furthermore, in the present study, we have found that the cultured cell monolayer of the immortalized mouse brain endothelial cell line, b.End3 is a very good *in vitro* model for studying the transport across the BBB. We will continue this *in vitro* study by culturing b.End3 cells on Matrigel which carries negative charge and may mimic the basement membrane of the BBB. Finally, we will co-culture the b.End3 in Matrigel along with the astrocytes to form a complete *in vitro* model for the BBB.

BIBLIOGRAPHY

Abbott, N. J., 2000. Inflammatory mediators and modulation of blood-brain barrier permeability. Cell Mol Neurobiol. 20**,** 131-47.

Adamson, R. H., Clough, G., 1992. Plasma proteins modify the endothelial cell glycocalyx of frog mesenteric microvessels. J Physiol. 445**,** 473-86.

Adamson, R. H., Huxley, V. H., Curry, F. E., 1988. Single capillary permeability to proteins having similar size but different charge. Am J Physiol. 254**,** H304-12.

Adamson, R. H., Lenz, J. E., Zhang, X., Adamson, G. N., Weinbaum, S., Curry, F. E., 2004a. Oncotic pressures opposing filtration across non-fenestrated rat microvessels. Journal of Physiology-London. 557**,** 889-907.

Adamson, R. H., Lenz, J. F., Curry, F. E., 1994. Quantitative laser scanning confocal microscopy on single capillaries: permeability measurement. Microcirculation. 1**,** 251-65.

Adamson, R. H., Lenz, J. F., Zhang, X., Adamson, G. N., Weinbaum, S., Curry, F. E., 2004b. Oncotic pressures opposing filtration across non-fenestrated rat microvessels. J Physiol. 557**,** 889-907.

Allt, G., Lawrenson, J. G., 1997a. Is the pial microvessel a good model for blood-brain barrier studies? Brain Res Brain Res Rev. 24**,** 67-76.

Allt, G., Lawrenson, J. G., 1997b. Is the pial microvessel a good model for blood-brain barrier studies? Brain Research Reviews. 24**,** 67-76.

Ballabh, P., Braun, A., Nedergaard, M., 2004. The blood-brain barrier: an overview: structure, regulation, and clinical implications. Neurobiol Dis. 16**,** 1-13.

Brightman, M. W., Kaya, M., 2000. Permeable endothelium and the interstitial space of brain. Cellular and Molecular Neurobiology. 20**,** 111-130.

Brown, R. C., Mark, K. S., Egleton, R. D., Huber, J. D., Burroughs, A. R., Davis, T. P., 2003. Protection against hypoxia-induced increase in blood-brain barrier permeability: role of tight junction proteins and NFkappaB. J Cell Sci. 116**,** 693-700.

Brown, R. C., Morris, A. P., O'Neil, R. G., 2007. Tight junction protein expression and barrier properties of immortalized mouse brain microvessel endothelial cells. Brain Res. 1130**,** 17-30.

Bruegger, D., Jacob, M., Rehm, M., Loetsch, M., Welsch, U., Conzen, P., Becker, B. F., 2005. Atrial natriuretic peptide induces shedding of endothelial glycocalyx in coronary vascular bed of guinea pig hearts. Am J Physiol Heart Circ Physiol. 289**,** H1993-9.

Butt, A. M., Jones, H. C., Abbott, N. J., 1990. Electrical resistance across the blood-brain barrier in anaesthetized rats: a developmental study. J Physiol. 429**,** 47-62.

Cabrales, P., Vazquez, B. Y., Tsai, A. G., Intaglietta, M., 2007. Microvascular and capillary perfusion following glycocalyx degradation. J Appl Physiol. 102**,** 2251-9.

Calabria, A. R., Shusta, E. V., 2006. Blood-brain barrier genomics and proteomics: elucidating phenotype, identifying disease targets and enabling brain drug delivery. Drug Discov Today. 11**,** 792-9.

Cassella , J. P., Lawrenson ,J. G. , Firth,J. A., 1997. Development of endothelial paracellular clefts and their tight junctions in the pial microvessels of the rat. Journal of Neurocytology 2. 26**,** 547-575.

Cassella, J. P., Lawrenson, J. G., Firth, J. A., 1997. Development of endothelial paracellular clefts and their tight junctions in the pial microvessels of the rat. J Neurocytol. 26**,** 567-75.

Connolly, D. T., Heuvelman, D. M., Nelson, R., Olander, J. V., Eppley, B. L., Delfino, J. J., Siegel, N. R., Leimgruber, R. M., Feder, J., 1989. Tumor vascular permeability factor stimulates endothelial cell growth and angiogenesis. J Clin Invest. 84**,** 1470-8.

Cornford, E. M., Young, D., Paxton, J. W., Sofia, R. D., 1992. Blood-brain barrier penetration of felbamate. Epilepsia. 33**,** 944-54.

Curry, F. E., Frokjaer-Jensen, J., 1984. Water flow across the walls of single muscle capillaries in the frog, Rana pipiens. J Physiol. 350**,** 293-307.

Curry, F. E., Rutledge, J. C., Lenz, J. F., 1989. Modulation of microvessel wall charge by plasma glycoprotein orosomucoid. Am J Physiol. 257**,** H1354-9.

Dallasta, L. M., Pisarov, L. A., Esplen, J. E., Werley, J. V., Moses, A. V., Nelson, J. A., Achim, C. L., 1999. Blood-brain barrier tight junction disruption in human immunodeficiency virus-1 encephalitis. Am J Pathol. 155**,** 1915-27.

de Lange, E. C., de Boer, B. A., Breimer, D. D., 1999. Microdialysis for pharmacokinetic analysis of drug transport to the brain. Adv Drug Deliv Rev. 36**,** 211-227.

del Zoppo, G. J., Hallenbeck, J. M., 2000. Advances in the vascular pathophysiology of ischemic stroke. Thromb Res. 98**,** 73-81.

Ding, Y., Li, J., Luan, X., Ding, Y. H., Lai, Q., Rafols, J. A., Phillis, J. W., Clark, J. C., Diaz, F. G., 2004. Exercise pre-conditioning reduces brain damage in ischemic rats that may be associated with regional angiogenesis and cellular overexpression of neurotrophin. Neuroscience. 124**,** 583-91.

Dvorak, H. F., Brown, L. F., Detmar, M., Dvorak, A. M., 1995. Vascular permeability factor/vascular endothelial growth factor, microvascular hyperpermeability, and angiogenesis. Am J Pathol. 146**,** 1029-39.

Easton, A. S., Fraser, P. A., 1994. Variable restriction of albumin diffusion across inflamed cerebral microvessels of the anaesthetized rat. J Physiol. 475**,** 147-57.

Easton, A. S., Sarker, M. H., Fraser, P. A., 1997. Two components of blood-brain barrier disruption in the rat. J Physiol. 503 (Pt 3)**,** 613-23.

Ehrlich, P., 1885. Das sauerstufbudurfnis des organismus. Hireschwald, Berlin.

Elsinga, P. H., Hendrikse, N. H., Bart, J., Vaalburg, W., van Waarde, A., 2004. PET Studies on P-glycoprotein function in the blood-brain barrier: how it affects uptake and binding of drugs within the CNS. Curr Pharm Des. 10**,** 1493-503.

Farkas, E., Luiten, P. G., 2001. Cerebral microvascular pathology in aging and Alzheimer's disease. Prog Neurobiol. 64**,** 575-611.

Floris, S., Blezer, E. L., Schreibelt, G., Dopp, E., van der Pol, S. M., Schadee-Eestermans, I. L., Nicolay, K., Dijkstra, C. D., de Vries, H. E., 2004. Blood-brain barrier permeability and monocyte infiltration in experimental allergic encephalomyelitis: a quantitative MRI study. Brain. 127**,** 616-27.

Fraser, P. A., Dallas, A. D., Davies, S., 1990. Measurement of filtration coefficient in single cerebral microvessels of the frog. J Physiol. 423**,** 343-61.

Fu, B., Chen, B., 2003. A model for the modulation of microvessel permeability by junction strands. Journal of Biomechanical Engineering-Transactions of the Asme. 125**,** 620-627.

Fu, B. M., Adamson, R. H., Curry, F. E., 1998. Test of a two-pathway model for small-solute exchange across the capillary wall. Am J Physiol. 274**,** H2062-73.

Fu, B. M., Adamson, R. H., Curry, F. R., 2005. Determination of microvessel permeability and tissue diffusion coefficient of solutes by laser scanning confocal microscopy. J Biomech Eng. 127**,** 270-8.

Fu, B. M., Chen, B., Chen, W., 2003. An electrodiffusion model for effects of surface glycocalyx layer on microvessel permeability. Am J Physiol Heart Circ Physiol. 284**,** H1240-50.

Fu, B. M., Li, G., Yuan, W., 2008. Charge effects of the blood-brain barrier on the transport of charged molecules. FASEB J. 22**,** 734.1-.

Fu, B. M., Shen, S., 2003. Structural mechanisms of acute VEGF effect on microvessel permeability. Am J Physiol Heart Circ Physiol. 284**,** H2124-35.

Fu, B. M., Shen, S., 2004. Acute VEGF effect on solute permeability of mammalian microvessels in vivo. Microvasc Res. 68**,** 51-62.

Gaber, M. W., Yuan, H., Killmar, J. T., Naimark, M. D., Kiani, M. F., Merchant, T. E., 2004. An intravital microscopy study of radiation-induced changes in permeability and leukocyte-endothelial cell interactions in the microvessels of the rat pia mater and cremaster muscle. Brain Res Brain Res Protoc. 13**,** 1-10.

Gil, E. S., Li, J., Xiao, H., Lowe, T. L., 2009. Quaternary Ammonium beta-Cyclodextrin Nanoparticles for Enhancing Doxorubicin Permeability across the In Vitro Blood-Brain Barrier. Biomacromolecules.

Goldmann, E., 1913. Vitalfarbung am zentralnervensystem. Abhandl Kongil preuss Akad Wiss. 1**,** 1-60.

Grabb, P. A., Gilbert, M. R., 1995. Neoplastic and pharmacological influence on the permeability of an in vitro blood-brain barrier. J Neurosurg. 82**,** 1053-8.

Hamann, G. F., Okada, Y., Fitridge, R., del Zoppo, G. J., 1995. Microvascular basal lamina antigens disappear during cerebral ischemia and reperfusion. Stroke. 26**,** 2120-6.

Haraldsson, B., Rippe, B., 1987. Orosomucoid as one of the serum components contributing to normal capillary permselectivity in rat skeletal muscle. Acta Physiol Scand. 129**,** 127-35.

Haraldsson, B. S., Johnsson, E. K., Rippe, B., 1992. Glomerular permselectivity is dependent on adequate serum concentrations of orosomucoid. Kidney Int. 41**,** 310-6.

Hawkins, B. T., Davis, T. P., 2005. The blood-brain barrier/neurovascular unit in health and disease. Pharmacol Rev. 57**,** 173-85.

Henry, C. B., Duling, B. R., 1999. Permeation of the luminal capillary glycocalyx is determined by hyaluronan. Am J Physiol. 277**,** H508-14.

Huxley, V. H., Curry, F. E., Adamson, R. H., 1987. Quantitative fluorescence microscopy on single capillaries: alpha-lactalbumin transport. Am J Physiol. 252**,** H188-97.

Huxley, V. H., Curry, F. E., Powers, M. R., Thipakorn, B., 1993. Differential action of plasma and albumin on transcapillary exchange of anionic solute. Am J Physiol. 264**,** H1428-37.

Hynes, R. O., 1992. Integrins: versatility, modulation, and signaling in cell adhesion. Cell. 69**,** 11-25.

Kaur, C., Ling, E. A., 2008. Blood brain barrier in hypoxic-ischemic conditions. Curr Neurovasc Res. 5**,** 71-81.

Kaur, C., Sivakumar, V., Zhang, Y., Ling, E. A., 2006. Hypoxia-induced astrocytic reaction and increased vascular permeability in the rat cerebellum. Glia. 54**,** 826-39.

Kay, G. G., 2000. The effects of antihistamines on cognition and performance. J Allergy Clin Immunol. 105**,** S622-7.

Kendall, S., Michel, C. C., 1995. The measurement of permeability in single rat venules using the red cell microperfusion technique. Exp Physiol. 80**,** 359-72.

Kimura, M., Dietrich, H. H., Huxley, V. H., Reichner, D. R., Dacey, R. G., Jr., 1993. Measurement of hydraulic conductivity in isolated arterioles of rat brain cortex. Am J Physiol. 264**,** H1788-97.

Kremer, J. M., Wilting, J., Janssen, L. H., 1988. Drug binding to human alpha-1-acid glycoprotein in health and disease. Pharmacol Rev. 40**,** 1-47.

Kreuter, J., 2004. Influence of the surface properties on nanoparticle-mediated transport of drugs to the brain. J Nanosci Nanotechnol. 4**,** 484-8.

Lawrenson, J. G., Reid, A. R., Allt, G., 1997. Molecular characteristics of pial microvessels of the rat optic nerve. Can pial microvessels be used as a model for the blood-brain barrier? Cell Tissue Res. 288**,** 259-65.

Leblond, C. P., Inoue, S., 1989. Structure, composition, and assembly of basement membrane. Am J Anat. 185**,** 367-90.

Lewandowsky, M., 1900. Zur lehre von der cerebrospinalflussigkeit. Z Klin Med. 40**,** 480-494.

Matsumoto, K., Nishi, K., Kikuchi, M., Kadowaki, D., Tokutomi, Y., Tokutomi, N., Suenaga, A., Otagiri, M., 2007. Alpha1-acid glycoprotein suppresses rat acute

inflammatory paw edema through the inhibition of neutrophils activation and prostaglandin E2 generation. Biol Pharm Bull. 30**,** 1226-30.

Mayhan, W. G., 1999. VEGF increases permeability of the blood-brain barrier via a nitric oxide synthase/cGMP-dependent pathway. Am J Physiol. 276**,** C1148-53.

Merrill, M. J., Oldfield, E. H., 2005. A reassessment of vascular endothelial growth factor in central nervous system pathology. J Neurosurg. 103**,** 853-68.

Michel, C. C., Curry, F. E., 1999. Microvascular permeability. Physiol Rev. 79**,** 703-61.

Miosge, N., 2001. The ultrastructural composition of basement membranes in vivo. Histol Histopathol. 16**,** 1239-48.

Moghimi, S. M., Hunter, A. C., Murray, J. C., 2001. Long-circulating and target-specific nanoparticles: theory to practice. Pharmacol Rev. 53**,** 283-318.

Neuwelt, E. A., 2004. Mechanisms of disease: the blood-brain barrier. Neurosurgery. 54**,** 131-40; discussion 141-2.

Nicolazzo, J. A., Charman, S. A., Charman, W. N., 2006. Methods to assess drug permeability across the blood-brain barrier. J Pharm Pharmacol. 58**,** 281-93.

Oldendorf, W. H., Cornford, M. E., Brown, W. J., 1977. The large apparent work capability of the blood-brain barrier: a study of the mitochondrial content of capillary endothelial cells in brain and other tissues of the rat. Ann Neurol. 1**,** 409-17.

Omidi, Y., Campbell, L., Barar, J., Connell, D., Akhtar, S., Gumbleton, M., 2003. Evaluation of the immortalised mouse brain capillary endothelial cell line, b.End3, as an in vitro blood-brain barrier model for drug uptake and transport studies. Brain Res. 990**,** 95-112.

Pardridge, W. M., 1998. CNS drug design based on principles of blood-brain barrier transport. J Neurochem. 70**,** 1781-92.

Pardridge, W. M., 2006. Molecular trojan horses for blood-brain barrier drug delivery. Discov Med. 6**,** 139-43.

Paulson, O. B., Newman, E. A., 1987. Does the release of potassium from astrocyte endfeet regulate cerebral blood flow? Science. 237**,** 896-8.

Petty, M. A., Lo, E. H., 2002. Junctional complexes of the blood-brain barrier: permeability changes in neuroinflammation. Prog Neurobiol. 68**,** 311-23.

Predescu, D., Predescu, S., McQuistan, T., Palade, G. E., 1998. Transcytosis of alpha1-acidic glycoprotein in the continuous microvascular endothelium. Proc Natl Acad Sci U S A. 95**,** 6175-80.

Rascher, G., Fischmann, A., Kroger, S., Duffner, F., Grote, E. H., Wolburg, H., 2002. Extracellular matrix and the blood-brain barrier in glioblastoma multiforme: spatial segregation of tenascin and agrin. Acta Neuropathol. 104**,** 85-91.

Rosenberg, G. A., 1999. Ischemic brain edema. Prog Cardiovasc Dis. 42**,** 209-16.

Rosenberg, G. A., Estrada, E., Kelley, R. O., Kornfeld, M., 1993. Bacterial collagenase disrupts extracellular matrix and opens blood-brain barrier in rat. Neurosci Lett. 160**,** 117-9.

Sann, L., Bienvenu, F., Bienvenu, J., Bourgeois, J., Bethenod, M., 1984. Evolution of serum prealbumin, C-reactive protein, and orosomucoid in neonates with bacterial infection. J Pediatr. 105**,** 977-81.

Sawchuk, R. J., Elmquist, W. F., 2000. Microdialysis in the study of drug transporters in the CNS. Adv Drug Deliv Rev. 45**,** 295-307.

Schnitzer, J. E., Pinney, E., 1992. Quantitation of specific binding of orosomucoid to cultured microvascular endothelium: role in capillary permeability. Am J Physiol. 263**,** H48-55.

Schuetz, E. G., Schinkel, A. H., Relling, M. V., Schuetz, J. D., 1996. P-glycoprotein: a major determinant of rifampicin-inducible expression of cytochrome P4503A in mice and humans. Proc Natl Acad Sci U S A. 93**,** 4001-5.

Schulze, C., Firth, J. A., 1992a. Interendothelial Junctions during Blood-Brain-Barrier Development in the Rat - Morphological-Changes at the Level of Individual Tight Junctional Contacts. Developmental Brain Research. 69**,** 85-95.

Schulze, C., Firth, J. A., 1992b. Interendothelial junctions during blood-brain barrier development in the rat: morphological changes at the level of individual tight junctional contacts. Brain Res Dev Brain Res. 69**,** 85-95.

Smith, Q. R., 2000. Transport of glutamate and other amino acids at the blood-brain barrier. J Nutr. 130**,** 1016S-22S.

Sorensson, J., Matejka, G. L., Ohlson, M., Haraldsson, B., 1999. Human endothelial cells produce orosomucoid, an important component of the capillary barrier. Am J Physiol. 276**,** H530-4.

Squire, J. M., Chew, M., Nneji, G., Neal, C., Barry, J., Michel, C., 2001. Quasi-periodic substructure in the microvessel endothelial glycocalyx: a possible explanation for molecular filtering? J Struct Biol. 136**,** 239-55.

Tarbell, J. M., Pahakis, M. Y., 2006. Mechanotransduction and the glycocalyx. J Intern Med. 259**,** 339-50.

Ueno, M., Sakamoto, H., Liao, Y. J., Onodera, M., Huang, C. L., Miyanaka, H., Nakagawa, T., 2004a. Blood-brain barrier disruption in the hypothalamus of young adult spontaneously hypertensive rats. Histochemistry and Cell Biology. 122**,** 131-7.

Ueno, M., Sakamoto, H., Liao, Y. J., Onodera, M., Huang, C. L., Miyanaka, H., Nakagawa, T., 2004b. Blood-brain barrier disruption in the hypothalamus of young adult spontaneously hypertensive rats. Histochem Cell Biol. 122**,** 131-7.

Ueno, M., Sakamoto, H., Tomimoto, H., Akiguchi, I., Onodera, M., Huang, C. L., Kanenishi, K., 2004c. Blood-brain barrier is impaired in the hippocampus of young adult spontaneously hypertensive rats. Acta Neuropathol. 107**,** 532-8.

Uesaka, T., Shono, T., Suzuki, S. O., Nakamizo, A., Niiro, H., Mizoguchi, M., Iwaki, T., Sasaki, T., 2007. Expression of VEGF and its receptor genes in intracranial schwannomas. J Neurooncol. 83**,** 259-66.

van Uitert, R. L., Sage, J. I., Levy, D. E., Duffy, T. E., 1981. Comparison of radio-labeled butanol and iodoantipyrine as cerebral blood flow markers. Brain Res. 222**,** 365-72.

Wang, R., Ashwal, S., Tone, B., Tian, H. R., Badaut, J., Rasmussen, A., Obenaus, A., 2007. Albumin reduces blood-brain barrier permeability but does not alter infarct size in a rat model of neonatal stroke. Pediatr Res. 62**,** 261-6.

Yuan, F., Leunig, M., Berk, D. A., Jain, R. K., 1993. Microvascular permeability of albumin, vascular surface area, and vascular volume measured in human adenocarcinoma LS174T using dorsal chamber in SCID mice. Microvasc Res. 45**,** 269-89.

Yuan, W., Li, G., Zeng, M., Fu, B. M., 2009a. Modulation of the blood-brain barrier permeability by plasma glycoprotein orosomucoid. Microvasc Res.

Yuan, W., Lv, Y., Zeng, M., Fu, B. M., 2009b. Non-invasive measurement of solute permeability in cerebral microvessels of the rat. Microvasc Res. 77**,** 166-73.

Zhang, Y., Pardridge, W. M., 2001. Rapid transferrin efflux from brain to blood across the blood-brain barrier. J Neurochem. 76**,** 1597-600.

Zlokovic, B. V., Begley, D. J., Djuricic, B. M., Mitrovic, D. M., 1986. Measurement of solute transport across the blood-brain barrier in the perfused guinea pig brain: method and application to N-methyl-alpha-aminoisobutyric acid. J Neurochem. 46**,** 1444-51.